# MODELLING, SIMULATION, SYNTHESIS AND STRUCTURAL CHARACTERIZATION OF NI-FE BASED NANOALLOYS

A THESIS SUBMITTED TO
THE GRADUATE SCHOOL OF NATURAL AND APPLIED SCIENCES
OF
MIDDLE EAST TECHNICAL UNIVERSITY

BY

ECE ARSLAN IRMAK

IN PARTIAL FULFILLMENT OF THE REQUIREMENTS
FOR
THE DEGREE OF MASTER OF SCIENCE
IN
METALLURGICAL AND MATERIALS ENGINEERING

JUNE 2018

Approval of the thesis:

**MODELLING, SIMULATION, SYNTHESIS AND STRUCTURAL CHARACTERIZATION OF NI-FE BASED NANOALLOYS**

submitted by **ECE ARSLAN IRMAK** in partial fulfillment of the requirements for the degree of **Master of Science in Metallurgical and Materials Engineering Department, Middle East Technical University** by,

Prof. Dr. Halil Kalıpçılar _____
Dean, Graduate School of **Natural and Applied Sciences**

Prof. Dr. C. Hakan Gür _____
Head of Department, **Metallurgical and Materials Engineering**

Prof. Dr. Amdulla O. Mekhrabov _____
Supervisor, **Metallurgical and Materials Engineering, METU**

Prof. Dr. M. Vedat Akdeniz _____
Co-supervisor, **Metallurgical and Materials Eng., METU**

**Examining Committee Members:**

Prof. Dr. Macit Özenbaş
Metallurgical and Materials Engineering, METU _____

Prof. Dr. Amdulla O. Mekhrabov
Metallurgical and Materials Engineering, METU _____

Prof. Dr. M. Vedat Akdeniz
Metallurgical and Materials Engineering, METU _____

Prof. Dr. Rıza Gürbüz
Metallurgical and Materials Engineering, METU _____

Prof. Dr. Şükrü Talaş
Metallurgical and Materials Eng., Afyon Kocatepe University _____

**Date:** _____

**I hereby declare that all information in this document has been obtained and presented in accordance with academic rules and ethical conduct. I also declare that, as required by these rules and conduct, I have fully cited and referenced all material and results that are not original to this work.**

Name, Last Name: Ece Arslan Irmak

Signature :

# ABSTRACT

## MODELLING, SIMULATION, SYNTHESIS AND STRUCTURAL CHARACTERIZATION OF NI-FE BASED NANOALLOYS

IRMAK, ECE ARSLAN
M.S., Department of Metallurgical and Materials Engineering
Supervisor : Prof. Dr. Amdulla O. Mekhrabov
Co-Supervisor : Prof. Dr. M. Vedat Akdeniz

June 2018, 110 pages

There is a growing interest in the simulation and production of nanoalloys because the unique chemical and physical properties of nanoalloys can be tuned, and completely new structural motifs can be created by varying the type and composition of constituent elements, the atomic ordering, size, and shape of the nanoparticles. As an important magnetic material, Fe-Ni based nanoalloys have promising applications in the chemical industry, aerospace and stealth industry, magnetic biomedical applications and computer hardware industry. The purpose of this study is to analyze the structural properties of the magnetic nanoalloys at atomistic level and to establish a bridge between theoretical and experimental studies, in order to interpret many of experimental results and to predict the physical and chemical properties of the nanoalloys.

In the theoretical part, structural evolutions of Fe-Ni based nanoalloys have been studied by using molecular dynamics (MD) method in Large-scale Atomic/Molecular Massively Parallel Simulator (LAMMPS). In this regard, structural evolution of the bimetallic $FeNi_3$ crystalline and amorphous nanoalloys has been investigated by

means of MD simulation combined with Embedded Atom Model (EAM) with taking into account the effect of temperature (300-1700 K), particle size (2 nm-6 nm) and shape (spherical and cubic) on radial distribution functions, inter-atomic distances, coordination numbers, core-to-surface concentration profiles, surface energies and Voronoi analysis. From the molecular dynamics simulations, it has been clearly observed that the structural evolution, melting point and atomic arrangements of the nanoparticles exhibited strongly size and shape dependent behavior. As the particle size of the simulated nanoparticles increased, the particles became more heat-resistant and mostly preserved their stable crystalline structure, shape and mixing pattern at high temperatures. Also, it has been observed that the 6 nm nanoparticles owned the FCC lattice structure at room temperature which is consistent with the $L1_2$-type ordered structure of the synthesized via mechanical alloying $FeNi_3$ nanoparticles with soft magnetic properties.

In the experimental part of the study, $FeNi_3$ bimetallic nanoalloys were synthesized via mechanical alloying in a planetary high energy ball milling. The experimental studies were carried out in three parts. Firstly, mechanical alloying in high energy dry planetary ball milling with 250 and 400 rpm was applied to obtain $FeNi_3$ nanoparticles. Afterward, two-step mechanical alloying was performed in which dry milling was followed by surfactant-assisted ball milling to investigate the surfactant (oleic acid and oleylamine) and solvent (heptane) effect on the structure, size, and properties of the $FeNi_3$ nanoalloys. The structural and magnetic properties of the alloyed nanoparticles have been analyzed using XRD, SEM, EDS, and VSM techniques. In terms of the particle size, it was found that the amount of nano-sized particles raised with increasing milling time and milling speed, and consequently the magnetic properties of the particles varied. However, no significant effect of surfactants on the particle size was observed. The smallest, $L1_2$-type ordered $FeNi_3$ nanopowders with 5.82 nm crystallite size, -0.46% strain value, and 3.54263 Å lattice parameter, showing soft magnetic properties, were synthesized by mechanical alloying with 400rpm under dry atmosphere after 80 h milling time.

Keywords: Fe-Ni systems, Magnetic nanoalloys, Molecular dynamics, Embedded

atom model, Mechanical alloying

# ÖZ

## FE-Nİ BAZLI NANO-ALAŞIMLARIN, MODELLENMESİ SİMÜLASYONU, SENTEZLENMESİ VE YAPISAL ÖZELLİKLERİNİN BELİRLENMESİ

IRMAK, ECE ARSLAN
Yüksek Lisans, Metalurji ve Malzeme Mühendisliği Bölümü Bölümü
Tez Yöneticisi : Prof. Dr. Amdulla O. Mekhrabov
Ortak Tez Yöneticisi : Prof. Dr. M. Vedat Akdeniz

Haziran 2018 , 110 sayfa

Nanoalaşımların simülasyon ve üretimine giderek artan bir ilgi bulunmaktadır; çünkü nanoalaşımların benzersiz kimyasal ve fiziksel özellikleri, bileşenlerinin çeşidi ve kompozisyonu, nanoparçacıkların atomik düzeni, boyutu ve şekli değiştirilerek ayarlanabilir ve tamamen yeni yapısal motifler oluşturulabilir. Önemli bir manyetik malzeme olarak, Fe-Ni bazlı nanoalaşımların, kimyasal endüstride, havacılık ve savunma sanayide, manyetik biyomedikal uygulamalarda ve bilgisayar donanımı endüstrisinde ümit verici uygulama alanlarına sahiptir. Bu çalışmanın amacı; manyetik nanoalaşımların yapısal özelliklerini atomistik düzeyde incelemek, deneysel sonuçları öngörebilmek ve nanoalaşımların fiziksel ve kimyasal özelliklerini tahmin edebilmek için teorik ve deneysel çalışmalar arasında köprü kurmaktır.

Teorik bölümde, Fe-Ni bazlı nanoalaşımların yapısal dönüşümleri Büyük ölçekli Atomik / Moleküler Masif Paralel Simülatörde (LAMMPS) moleküler dinamik (MD) yöntemi kullanılarak incelenmiştir. Bu bağlamda, bimetalik $FeNi_3$ kristal ve amorf nanoalaşımların yapısal evrimi; sıcaklığın (300-1700 K), parçacık büyüklüğünün (2 nm-6nm) ve parçacık şeklinin (küresel ve kübik) radyal dağılım fonksiyonları, atom-

lar arası mesafeler, koordinasyon numaraları, çekirdek-yüzey konsantrasyon profilleri, yüzey enerjileri ve Voronoi analizi üzerinde etkisi dikkate alınarak, Gömülü Atom Modeli (EAM) ile kombine edilmiş MD simülasyonu ile incelenmiştir. Moleküler dinamik simülasyonlarda parçacıkların yapısal dönüşümü, erime sıcaklığı ve atomların konfigürasyonu güçlü bir şekilde boyuta ve şekle bağlı davranış sergilemiştir. Simüle edilmiş parçacıkların boyutu arttıkça, parçacıklar ısıya daha dayanıklı olmuş ve kararlı kristal yapılarını, şekillerini ve atomik paternlerini yüksek sıcaklıklarda korumuşlardır. Ayrıca, 6 nm nanoparçacıkların, oda sıcaklığında, FCC örgü yapısına sahip olduğu, bunun da, mekanik alaşımlama ile sentezlenen ve yumuşak manyetik özelliklere sahip $FeNi_3$ nanoparçacıklarının $L1_2$-tipi düzenli yapısına uygun olduğu gözlenmiştir.

Çalışmanın deneysel bölümünde, $FeNi_3$ bimetalik nanoalaşımlar, gezegen tipli yüksek enerjili bilyeli değirmende mekanik alaşımlama yoluyla sentezlenmiştir. Deneysel çalışmalar üç aşamada gerçekleştirilmiştir. İlk olarak, $FeNi_3$ nanopartikülleri elde etmek için 250 ve 400 rpm öğütme hızı ile yüksek enerjili kuru gezegen tipi değirmende mekanik alaşımlama uygulanmıştır. Sonrasında, iki aşamalı mekanik alaşımlama gerçekleştirilmiştir; bu yöntemde, kuru öğütme işlemine, yüzey aktif madde (oleik asit ve oleylamine) ve çözücünün (heptan) $FeNi_3$ nanoalaşımların yapısı, boyutu ve özellikleri üzerindeki etkisini araştırmak için sürfaktan destekli bilyeli öğütme ile devam edilmiştir. Alaşımlanmış nanopartiküllerin yapısal ve manyetik özellikleri XRD, SEM, EDS ve VSM teknikleri kullanılarak analiz edilmiştir. Parçacık büyüklüğü açısından, artan öğütme süresi ve öğütme hızı ile nano boyutlu parçacıkların miktarı artmış ve buna bağlı olarak manyetik özellikleri değişim göstermiştir. Ancak surfaktanların parçacık boyutu üzesinde belirgin bir etkisi gözlenmemiştir. Yumuşak manyetik özellik gösteren, 5.82 nm kristal boyutlu, -0.46% gerilme değerli ve 3.54263 Å kafes parametreli en küçük, $L1_2$-tipi düzenli yapıya sahip $FeNi_3$ nanotozlar; kuru atmosfer altında, 400 rpm öğütme hızında mekanik alaşımlama yöntemi ile 80 saat öğütme süresinden sonra sentezlenmiştir.

Anahtar Kelimeler: Fe-Ni sistemleri, Manyetik nanoalaşımlar, Moleküler dinamik, Gömülü atom modeli, Mekanik alaşımlama

*To my beloved Erdem.*

## ACKNOWLEDGMENTS

I would like to express my gratitude to my supervisor, Amdulla O. Mekhrabov and my co-advisor Vedat Akdeniz for invaluable guidance and support.

I also thank to technical and administrative staff of the Department of Metallurgical and Materials Engineering for their assistance and the facilities they have provided.

Computing resources used in this work were provided by the National Center for High Performance Computing of Turkey (UHeM) under grant number 4004752017, which authors gratefully acknowledge.

I would like to also show gratitude to Mine Konuk Onat for her understanding and advices. I sincerely acknowledge the former and present members of the NOVALAB group for their helps and friendship.

Finally, I feel myself indebted and grateful to my parents and my brother for their love and endless support throughout my life.

## TABLE OF CONTENTS

## LIST OF TABLES

TABLES

## LIST OF FIGURES

FIGURES

## LIST OF ABBREVIATIONS

| | |
|---|---|
| BCC | Body-Centered Cubic |
| CM | Center of Mass |
| CN | Coordination Numbers |
| DFT | Density Functional Theory |
| EAM | Embedded-Atom Method |
| EDS | Energy Dispersive Spectroscopy |
| FFC | Face-Centered Cubic |
| GGA | Generalized Gradient Approximation |
| IBC | Isolated Boundary Condition |
| ID | Interatomic Distances |
| LAMMPS | Large-Scale Atomic/Molecular Massively Parallel Simulator |
| LDA | Local Density Approximation |
| MA | Mechanical Alloying |
| MD | Molecular Dynamics |
| NVE | Microcanonical Ensemble |
| NVT | Canonical Ensemble |
| NPT | Isothermal-Isobaric Ensemble |
| PBCs | Periodic Boundary Conditions |
| PEF | Potential Energy Functions |
| PP | Pseudopotential Theory |
| PPW | Projector-Augmented Wave Method |
| RDF | Radial Distribution Functions |
| SEM | Scanning Electron Microscopy |
| VSM | Vibrating-Sample Magnetometer |

| | |
|---|---|
| XRD | X-Ray Diffraction |
| $\mu$VT | Grand Canonical Ensemble |

# CHAPTER 1

# INTRODUCTION

In 1959, Richard Feynman, who is the American theoretical physicist, gave the talk was entitled as “There’s Plenty of Room at the Bottom” [14]. Although Feynman did not use the "nanotechnology" term during his speech, this lecture became the central point in the field of nanotechnology and since then there has been an intense research interest in nanotechnology which is based on the materials in nanosize.

Nanostructured materials are any materials with at least one-nanometer dimension in 1-100 nm range, and they can include identical atoms or molecules of different species. Nanomaterials act as a boundary between an atom and macro systems and present an attractive potential for newly-emerging applications because of the high surface area to volume ratio and the quantum confinement effect [14].

After several valuable studies on pure nanostructured materials for the last few decades, the research interests have started to move towards nanostructured alloys since the special properties can be achieved by controlling the type of constituent elements, atomic and magnetic ordering, as well as size and shape of the nanoparticles for several promising research and application area, such as catalysis, energy storage, magnetism, optics, lightweight construction, cosmetics, etc. [3, 15].

In addition to the size-dependent structure of the nanoparticles, in bimetallic nanoalloys, the difference in structural and geometrical forms of the nanoalloys leads to increase the complexity of the system. In pure nanoparticles, for specified particle size, different geometric forms could be formed which are called as isomers. However, for bimetallic nanoalloys, the number of possible structural forms which are homotops and composomers are more dependent on the composition differently from

isomers. Homotops are the structures with a fixed number of atoms, same composition and same geometrical arrangement of atoms but differ only in the specific way of the atoms arrangement and mixing. On the other hand, composomers which refer to compositional isomers have the fixed number of atoms, same geometrical structure but differ in composition [3].

Bimetallic nanoalloys can be classified according to their mixing patterns, geometric structures, and chemical ordering. To investigate the physical and chemical properties of nanoalloys and to determine which applications are suitable for them, the mixing patterns have a crucial role. There are four main mixing patterns of bimetallic nanoalloys which are core-shell segregated, subcluster segregated, mixed and multi-shell nanoalloys [3, 16]. Archetypal mixing patterns for bimetallic nanoalloys are illustrated in Figure1.1.

- Mixed nanoalloys can be either ordered (Figure 1.1a) or random (Figure 1.1b). According to literature, the most common mixing type in bimetallic nanoalloys is the random mixing pattern.
- In core-shell segregated nanoalloys, a shell of one type of atom surrounds a core-shell of another type atom (Figure 1.1c), but some mixing may also occur between the core and the shell.
- Multi-shell nanoalloys may present layered or onion-like alternating shells. In multi-shell mixing pattern, two more layers are observed, and the cluster of one type of atoms is surrounded by the shell of the other type of atom which is also surrounded by the shell of the previous type of the atom (Figure1.1d).
- In subcluster segregated (phase-separated) of nanoalloys, there are separate subclusters of immiscible elements (Figure 1.1e&f). Theoretically, it is stated that this type of mixing pattern is possible, but the pattern has not been observed practically, yet.

Moreover, there are various crystalline and noncrystalline structures for nanoalloys. Crystal is a set of arranged nuclei in a periodic pattern for three directions. Some of the common crystal structures of the nanostructured alloys are octahedra, truncated

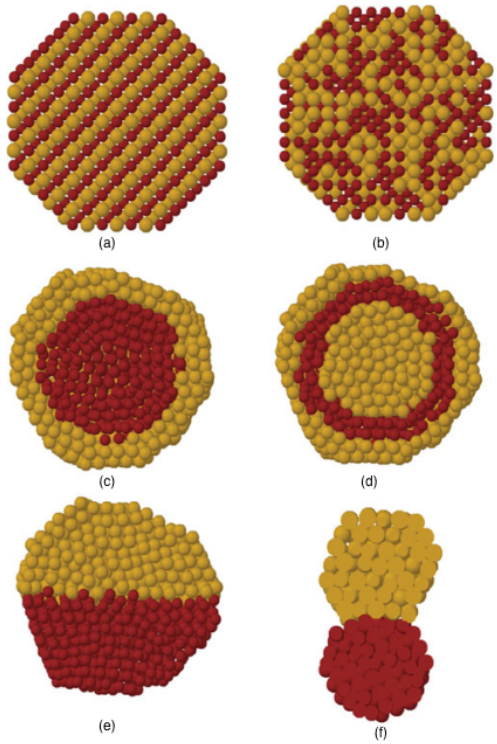


Figure 1.1: Mixing patterns of bimetallic nanoalloys (a) Ordered (b) Random (c) Core-shell (d) Three-shell (e-f) Subcluster segregated [2]

octahedra, and dodecahedra. On the other hand, non-crystalline structures do not have periodic arrangements, but generally have more compact shapes, such as icosahedral, polyicosahedral and twinned structures [3, 17]. Illustration of some geometric shapes of the nanoparticles are shown in Figure 1.2

Although there are several parameters that have an influence on the structural, segregation preferences and mixing pattern of nanoalloys, the main factors that affect segregation, mixing and ordering in nanoalloys are listed below [3, 18].

1. Atomic Sizes: Smaller atoms prefer to be in the core shell.

2. Surface Energy: The atoms which have the lowest surface energy tends to segregate at the surface in order to minimize the total energy of the system.

3. Cohesive Energy: Large difference in cohesive energies between two elements leads to segregation.

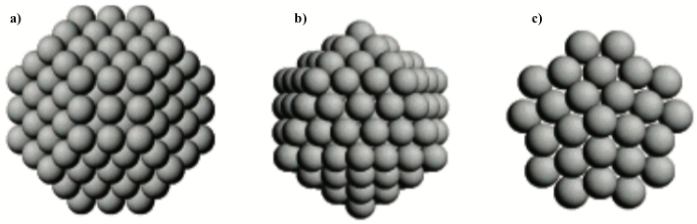


Figure 1.2: Schematic representation of some possible geometric shapes of nanoparticles a) FCC truncated octahedron b) icosahedron c) truncated decahedron [3]

4. Bond Strengths: There is a tendency towards mixing when the bonds of the unlike atoms are stronger than the bonds between like atoms. If the bonds of like atoms are stronger, segregation is formed.

5. Charge Transfer: Charge transfer between atoms affects the tendency towards mixing.

6. Binding Energy: Atoms which has a stronger binding with the surfactants tend to occupy the surface.

7. Electronic & Magnetic Effects: Electronic shell structure or electron spin interactions may lead to the stabilization of the cluster size or specific segregation arrangements.

8. Experimental Conditions & Synthesis Methods: The experimental conditions, in which the studies are conducted, have an influence on the mixing and ordering.

As the size decreases to the nano-dimensions, the fraction of the surface atoms in the material increases, so a large number of atoms are located in or close to grain boundaries and interfaces that alter the surface energy significantly. For example, if the grain size is decreased to 100 nm, 3 vol.% of the atoms or if the grain size is 5 nm, 50 vol.% of the atoms are located in the grain boundaries [19]. In general, the non-negligible influence and enhancement on the physical and mechanical properties are observed when the size of the particles is decreased to a range where the ratio of surface atoms to the total number of atoms is approximately equal to 0.5 [20, 21].

Furthermore, by reducing the system length scale to the nanoscale, the effects of quantum confinement and surface plasmon resonance alter the optical and electrical properties of the nanoalloys [22].

The quantum confinement effect, which is observed when the particle size is too small to be compared with the wavelength of the electron, plays a crucial role in the properties of the nanostructured materials. In bulk materials, the atomic energy levels spread out into energy bands and the bands vary according to the type of the material; for example, in metals, there is almost no energy band gap between valence and conduction band, so electrons are free to flow. However, as the size of a particle decreases to the nanoscale, the energy bands are replaced by discrete energy states, and this widens up the effective band gap, which leads to an alteration in the optical and electrical properties of the material. For instance, with the widened band gap and the confined electron motion, conductivity decreases and the conductive materials start to behave as a semiconductor or an insulator. Also, due to the broadened band gap, the absorbed, transmitted and scattered light, and consequently the optical properties of the nanoalloys change comparing to their bulk counterparts [14, 3].

The optical properties of the nanostructured alloys can also be controlled by the surface plasmon besides to tuning size, composition, and band gap. Surface plasmon resonance is an oscillation of valence electrons which occurred due to the interaction between the incident light and surface electrons. When the dimension of the nanoparticles is close to the wavelength, surface plasmon is excited by a light that results in absorption or scattering of the photons. As the particle size decreases, the plasmon resonance frequency increases which lead to a blue shift in the spectrum [16, 22, 14, 23].

With regard to the magnetic properties of the nanostructured alloys, the special magnetic properties are shown up when the size of the nanoparticles are smaller than the single domain limit of the material at which there is no domain wall. In bulk materials, remanence and coercivity are independent of the grain size. However, as the grain size decreases, magnetic domains start to show resistance. Therefore, coercive magnetic field increases with the strong coupling forces and the material becomes a harder magnetic material. This range of particle size is used for magnetic data storage.

On the other hand, after a critical point at which multidomain transforms to single-domain, crystalline anisotropy energy, which is the energy required to change the direction of magnetization, decreases and remanence and coercivity vanish. Therefore, the superparamagnetic material is obtained due to the single domain region. For the superparamagnetic materials which have a low coercivity and high permeability, thermal energy is sufficient to change the direction of magnetization of the entire crystal, even though the temperature is below the Curie temperature. [14, 20, 19]. The change in coercive force with respect to particle size and a corresponding change in magnetic hysteresis loop are shown in Figure1.3.

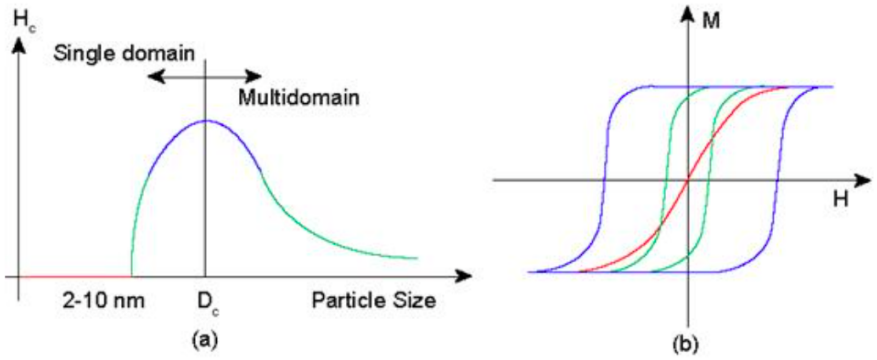


Figure 1.3: (a) Variation of coercivity with the particle size, (b) The corresponding variation in the magnetic hysteresis loop shape [4]

Due to the fine size effects that described above, magnetic nanoalloys have considerable attention with enhanced mechanical, electrical, optical and magnetic behavior for the special applications, such as radar absorbing material, catalyst, and biomaterial.

The radar absorbing materials (RAM) are the class of materials used in stealth technology to disguise a vehicle or structure from radar detection. A material's absorbency at a given frequency of radar wave depends upon its composition and particle size. RAM can have greater absorbency at some frequencies than other materials. To promote microwave absorption, a radar absorbing material should have good thermal stability, high saturation magnetization, high Curie temperature, low coercivity, high magnetic permeability [24]. Due to the disadvantages of the traditional materials that are used for this purpose, such as being thick and overweight, there is a growing interest in the usage of magnetic nanoalloys in radar absorbing materials because the

surface effects, the boundaries between grains of particles and the particle size can improve the absorbing properties of the material [25].

Moreover, in recent years, nanostructured alloys started to play a significant role in novel catalytic systems because it is possible to obtain different and enhanced characteristics and to increase the surface area of the catalysts [16, 26, 17]. Although the noble metals in nanosize, like platinum and palladium, are being used as a catalyst, in the future, there may be some supplying and economical problems for them [26]. Therefore, there is a growing interest in bimetallic catalytic nanoalloys which are formed with the combination of noble metals and other metals, such as copper and nickel [16]. Although it has been demonstrated that the surface activity of metallic nanoparticles can be improved by reducing its size and the combination of the two or more metals, the selectivity behavior is sensitive to the surface arrangements of the atoms [27]. Thus, investigating the structural behavior of the nanoalloys in advance plays a crucial role for the catalytic applications.

Due to having superior optical and magnetic properties, nanoalloys also have potential usage and research area in biomedical applications like nuclear magnetic resonance (NMR) imaging, drug and gene delivery, hyperthermia, MRI contrast enhancement and fluorescent biological labeling. Surface plasmon resonance has critical importance in biosensing and drug delivery. Therefore, it is known that noble metals, such as gold and silver, have been using for several years because of their unique surface plasmon properties. On the other hand, magnetic nanoalloys, such as iron-platinum, iron-nickel or iron-cobalt nano-systems have a promising research and application area in biomedical applications since they exhibit surface plasmon resonance effect and special properties such as superparamagnetism, high Curie temperature, low coercivity, high permeability and high saturation magnetization. However, there is not enough information regarding the usage area of the nanoalloys for biomedical applications because of the concern of the agglomeration, oxidation, and degradation; therefore, it is essential to obtain chemically stable nanoalloys for the biomaterials [16].

## 1.1 $FeNi_3$ Nanoalloys

The magnetic properties of bimetallic Fe-Ni based alloys depend on the composition of the constituents. For example, permalloys that contain more than 30% Ni act as a soft magnetic material. On the other hand, when the concentration of nickel is decreased to 30% Ni, the alloy starts to act as invar [20].

The phase diagram of Fe-Ni system is shown in the Figure 1.4, and the crystallographic data is listed in Table 1.1.

Iron-nickel based alloys offer a unique system to study austenitic steels, Invar effect, and the martensitic transformation. Fe-rich side of the phase diagram has the body-centered ferritic phase which has a wide range usage area in nuclear applications; on the other hand, austenitic phase dominates the face-centered cubic structured on the Ni-rich side. In addition, in the Fe-Ni bimetallic system, there is a eutectic phase decomposition from $\gamma$Fe,Ni phase at 345 °C [28, 29, 30].

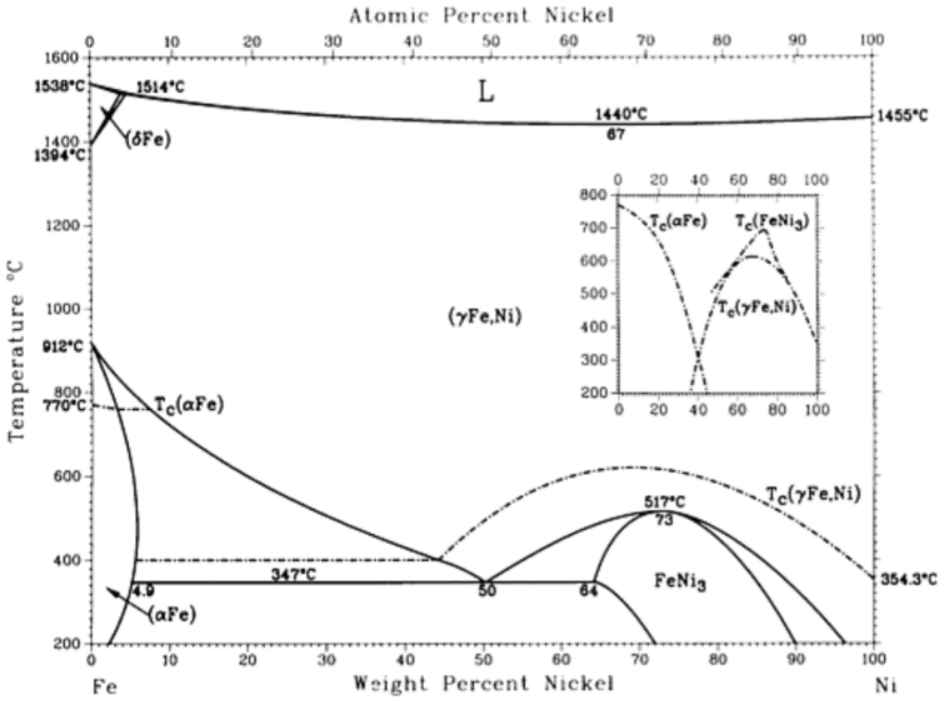


Figure 1.4: Phase diagram of the Fe-Ni system [1]

Table 1.1: Crystallographic data of Fe-Ni system [1]

| Phase | Composition (% Ni) | Pearson Symbol | Space Group |
|---|---|---|---|
| $\delta$ Fe | 0 - 3.7 | cI2 | $Im\bar{3}m$ |
| $\gamma$ Fe,Ni | 0 - 100 | cF4 | $Fm\bar{3}m$ |
| $\alpha$ Fe | 0 - 5.8 | cI2 | $Im\bar{3}m$ |
| $Fe_3Ni$ | 26 | cP4 | $Pm\bar{3}m$ |
| FeNi | 51 | tP2 | P4/mmm |
| $FeNi_3$ | 64 - 90 | cP4 | $Pm\bar{3}m$ |

Besides the stable body-centered cubic form on the Fe-rich side, there are three possible ordered Fe-Ni based intermetallic alloys which are $Fe_3Ni$, FeNi, and $FeNi_3$ below 1184 K [31]. Intermetallic alloys have special importance in many research and application area because of having superior performance in structural and magnetic properties. Although FeNi has been proposed as a stable intermetallic according to some theoretical and experimental studies [29, 30, 32], the existence of stable FeNi ordered phase is only possible under extremely slow cooling conditions that are almost inaccessible under laboratory condition, so the existence of stable FeNi ordered phase is still an open question. Also, there is still an open question about the stability of the $Fe_3Ni$, so these two structures are not shown in the phase diagram [28].

According to several studies, it has been proven that $FeNi_3$ which has a superstructure of $AuCu_3$ type FCC lattice and $Pm\bar{3}m$ space group is the stable ordered intermetallic with 3.525 Å lattice parameter [33]. $FeNi_3$ is formed by a first-order order-disorder transformation with a latent heat below 517 °C [28]. The ordered crystal structure of $FeNi_3$ system is shown in Figure1.5. $FeNi_3$ is also known as permalloy, and it has a wide range usage area in magnetic application due to having maximum permeability for wide concentration and temperature range.

As an important magnetic nanoalloy, the novel application area of $FeNi_3$ nanoalloys is expected to be widened in the chemical, aerospace industry and magnetic biomedical applications with improved mechanical and magnetic behavior due to fine size effects.

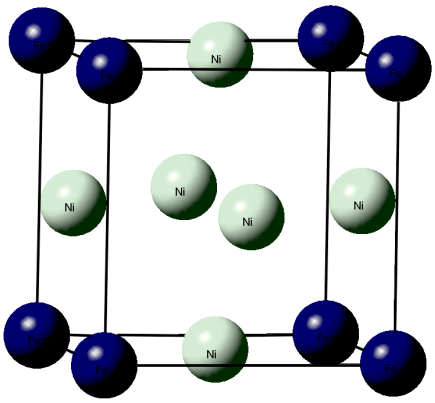


Figure 1.5: $AuCu_3$ type FCC lattice of ordered $FeNi_3$ alloy

## 1.2 Aim of the Study

The main aim of this study is to establish a bridge between theoretical and experimental studies, to interpret of many experimental results and to predict the properties of the nanoalloys.

Although structural properties of bulk alloys can be predicted from phase diagrams with temperature, pressure, and composition, the bulk phase diagrams do not allow making predictions about the formation behavior and physical properties of nanoalloys, as the properties of the nanoalloys are not identical with their bulk counterparts below the critical size. Therefore, computer modeling is an essential tool as the physical and chemical properties of nanosized alloys depend not only on the particle or crystallite size but also on composition and atomic ordering [3, 18].

For new generation nanoalloys, it is important to predict structure-property relations in advance. To supply this demand and make a contribution to the literature, in this thesis, crystalline and amorphous structure of $FeNi_3$ alloys in bulk and nano dimensions for different shape and size have been simulated by molecular dynamics method and synthesized by mechanical alloying.

In this regard, $FeNi_3$ structured nanoalloy has been considered because of its magnetic behavior, stable structure and the property of oxidation resistance. With its superior properties, $FeNi_3$ nanoalloys have promising application and research area

in the chemical industry (catalysis, battery), aerospace and stealth industry (radar absorbing material, jet engine alloys), magnetic biomedical applications (drug delivery, magnetic resonance imaging, biosensor) and computer hardware industry (data storage).

This study has been carried out in two main parts, which are theoretical and experimental parts.

In the theoretical part of the study, structural evolutions of $FeNi_3$ nanoparticles have been studied by using molecular dynamics (MD) method in Large-scale Atomic/-Molecular Massively Parallel Simulator (LAMMPS) with embedded atom model (EAM) which is capable of describing Fe-Ni bimetallic systems. Input files of the bulk and crystalline nano-systems were prepared in MEDEA software; however, the amorphous nanoparticles were obtained by subtracting from the amorphous bulk structure. Then, the heat-treated $FeNi_3$ crystalline and amorphous nanoparticles were illustrated by using VMD molecular graphics program. Also, Voronoi analysis was implemented with the OVITO software.

The formation and development of structures and their stability have been investigated at wide temperature range (300-1700 K) for the amorphous and crystalline $FeNi_3$ spherical nanoparticles with 2-6 nm diameters by calculating radial distribution functions (RDF), interatomic distances (ID), coordination numbers (CN), core-to-surface concentration profiles as well as surface energies and Voronoi analysis.

In the experimental part of the study, $FeNi_3$ bimetallic nanoalloys were synthesized by mechanical alloying in a planetary high energy ball mill. The experimental studies were carried out in three parts.

Firstly, dry mechanical alloying with high energy dry planetary ball milling was applied to obtain $FeNi_3$ nanoparticles. Secondly, the milling speed was increased to investigate the speed effect on the structural and magnetic properties of the powders. Then, two-step mechanical alloying was performed in which dry milling was followed by surfactant-assisted ball milling to observe the surfactant and solvent effect on the structure, size, and properties of the $FeNi_3$ nanoalloys. During two-step mechanical alloying, heptane was used as milling medium, and as surfactants, oleic acid

and oleylamine were used.

The characterization of the alloyed particles in terms of microstructure, morphology, particle size and magnetic properties with respect to milling time was done by X-ray diffraction (XRD), scanning electron microscopy (SEM), energy dispersive spectroscopy (EDS) and vibrating-sample magnetometer (VSM).

## 1.3 Organization

This thesis is organized as follows. In Section 2, the background of the computer simulations was briefly explained, such as quantum mechanical methods, Monte Carlo, and molecular dynamics methods. Afterward, the methodology and the results of the theoretical studies were given with detailed figures in the same section. In Section 3, production methods of the nanoalloys were reviewed and the mechanical alloying mechanism was described. Subsequently, the experimental studies were presented and the characterization results were discussed.

# CHAPTER 2

# SIMULATION OF IRON AND NICKEL BASED NANOALLOYS

## 2.1 Theoretical Background

There is a growing interest in the computer simulations to interpret of many experimental results and to predict structural, electronic, magnetic properties, geometric form and atomic order of the nanoalloys because the simulations give considerable understanding for various problems at atomistic levels and reduce the development time for new materials with novel properties [3, 18].

Although first-principles quantum mechanical methods provide the most accurate results, they need a large computational effort to solve the Schrödinger equation for only a few tens of atoms. Thus, first-principles quantum mechanical methods are mainly used for the static properties of small systems. On the other hand, empirical or semi-empirical inter-atomic potentials can be used for larger systems to study both the static and the dynamic properties of systems [34]. The simulation methods which are based on the empirical and semi-empirical potentials are called as atomistic-level simulations. There are four main tools of atomistic computer simulations which are Statics, Monte-Carlo, Molecular Dynamics and Lattice Dynamics [35].

In this study, Monte-Carlo and Molecular Dynamics simulation tools are described as the most common atomistic-level simulations. Also, density functional theory is briefly explained as a quantum mechanical method.

After the general information about the atomistic-level simulations, the four main elements of the simulations are described, which are potential energy functions, geometrical constraints, canonical ensemble and numerical algorithms. For all systems,

inter-atomic potentials play a crucial role to obtain an accurate results [36].

### 2.1.1 Quantum Mechanical Methods

Quantum mechanical theory is based on the time-independent, non-relativistic Schrödinger equation (equation2.1) in order to determine the total energy, and the energy changes of the atoms.

$$H\psi = \mathrm{E}\psi \tag{2.1}$$

Here, H is the Hamiltonian operator, $\psi$ is eigenstates and E is the ground state energy of the electrons which is the lowest energy state [7]. The properties of the atoms are understood with the determination of the eigenfunctions of the many-body Hamiltonian in which energy contribution of electrons and nuclei is considered.

$$H = T + V \tag{2.2}$$

Here, T is kinetic energy and V is the potential term. There are three types of interactions to provide the potential term which are nucleus-nucleus, nucleus-electron, and electron-electron interaction. In theory, kinetic energy term contains both the kinetic energies of electrons and nuclei; however, as nuclei are much heavier than the electrons, the kinetic energy of nuclei is neglected which is called the Born-Oppenheimer Approximation. Therefore, the eigenfunctions of the Hamiltonian depend only on electronic variables.

For the many-body Hamiltonian, the general Schrödinger expression is shown in the equation 2.3

$$\left[\frac{h^2}{2m}\sum_{i=1}^{N}\nabla_i^2 + \sum_{i=1}^{N}V\left(r_i\right) + \sum_{i=1}^{N}\sum_{j\neq i}U\left(r_i, r_j\right)\right]\psi = \mathrm{E}\psi \tag{2.3}$$

The first term in the bracket is the kinetic energy of each electron; the second term is the interaction energy between electron and nuclei, and the third term is electron-

electron interaction. For the many-body Hamiltonian, $\psi$ is selected as an electronic wave function [37].

#### 2.1.1.1 Density Functional Theory

One of the most common first-principles approaches to describe the quantum behavior of atoms, molecules, and alloys is the density functional theory (DFT) which offers accurate results[18].

The density functional theory is based on two fundamental theorems which were proven by Hohenberg and Kohn. The first one is that the ground state energy can be defined in terms of the electron density. The other theorem is that the correct electron density minimizes the energy which is called the ground state energy [38]. This means that, in DFT, the total energy is considered as a functional of the electron density. Therefore, if the true functional form is known, the electron density and the ground state energy can be obtained without solving many-body wave function which is the basis of quantum mechanical treatment[39, 37].

With the Kohn & Sham equations 2.4, DFT maps the complex many-body electronic problem into a single-particle problem and finds the correct electron density by solving set of equations with an exchange-correlation energy which is the difference between the exact total energy and the classical Hartree energy [18, 37].

$$\left(-\frac{h^2}{2m_e}\nabla^2 + V_{ext}\left(r\right) + \int \frac{\rho\left(r^{'}\right)}{|r-r^i|}dr^{'} + V_{xc}\left[\rho\left(r\right)\right]\right)\psi_i\left(r\right) = \epsilon_i\psi_i\left(r\right) \tag{2.4}$$

Here, the first term on the left is the kinetic energy of the non-interacting electrons, the second term is the single-body interaction potential, which describes the potential between the nucleus and core ion, the third term represents the electron-electron interaction which includes Coulomb repulsion, and the last one is the exchange-correlation term [18]. $\psi$ is the single particle orbital and $\epsilon$ is the corresponding eigenvalue [40].

The single-body interaction potential that is also known as the external energy can be defined by Pseudopotential (PP) Theory or Projector-Augmented-Wave Method

(PPW). The interaction potentials describe the behavior of the ground state electronic energy and they are necessary because it is practically impossible to calculate the many-body electronic wave function [18]. The accuracy of the computational modeling depends on the proper potential selection for the system [40].

The electronic density in the Kohn & Sham equations depends on the single-particle orbitals and the solution of the density is obtained by iteration; therefore, DFT requires high computational effort [18]. Basically, the algorithm of the DFT starts with setting initial electron density and the approximation of the exchange-correlation function. Afterward, the Kohn & Sham equations are solved simultaneously, and new electron density is obtained. If the electron density is same as the initially set density, the iteration finishes; otherwise, the iteration continues [40].

**Exchange-Correlation Energy**

Although it is almost impossible to determine the exact value of the exchange-correlation, the accuracy of the DFT depends on how close the exchange-correlation to the exact value [37].

There are several kinds of approximations for the exchange and correlation energy. One of the common approximations is the local density approximation (LDA) and the other is generalized gradient approximation (GGA).

In local density approximation, the electron density is considered as the uniform for all points in the system, and only local density is used to define the exchange-correlation energy [37].

In generalized gradient approximation, the local gradient in electron density is defined in addition to the local electron density to define exchange-correlation energy. It usually gives more accurate results, especially for non-homogeneous systems. Since there is not only one way to define the gradient in electron density, several GGA functionals have been developed, such as Perdew-Wang functional (PW91) and Perdew-Burke-Ernzerhof functional (PBE), for different systems [37].

### 2.1.2 Monte Carlo

Monte-Carlo method is based on the repeated random displacements to obtain physical results of a system. Monte Carlo simulations are not capable to give information regarding the time evolution of a system, but they provide a representative configuration with relevant thermodynamic properties. In this method, firstly, initial energy of the system is calculated according to the specified coordinates of particles by using inter-atomic potentials. Then, random displacement is applied and the energy according to the new configuration is determined. If the energy of the new configuration is smaller than the initial one, the new configuration is accepted and the initial energy is replaced with the accepted one; then the iteration continues. Otherwise, Boltzmann factor is calculated (equation 2.5) and Metropolis condition is checked in which is the acceptance function is used for the new position [41, 35].

$$A = e^{-\frac{\Delta \mathrm{E}}{kT}} \quad \Delta \mathrm{E} = \mathrm{E}_2 - \mathrm{E}_1 \tag{2.5}$$

If A>R, where R is a random number between zero and one, the new position is accepted; otherwise, the previous position is saved and the iteration continues from the second step. The iteration finalizes when the equilibrium is achieved [5].

### 2.1.3 Molecular Dynamics

Molecular Dynamics is a computer simulation method which helps to explain atomic motions as a function of time and describes the behavior of the system with the help of inter-atomic potentials. For this purpose, classical equations of motion, specifically Newton's Law, is numerically integrated for the time evolution of interacting atoms by the variety of numerical algorithms [42]. In molecular dynamics method, atoms interact through the specified inter-atomic potentials in periodic boundary conditions.

Molecular dynamics simulations can generate more realistic growth kinetics than Monte Carlo simulations because they can reproduce physical atomic trajectories. The use of MD is especially important in nanoparticles, where the variety of possible structures does not allow using the coarse-grained lattice models that are appropriate for the simulation of bulk crystal growth [43]. Also, molecular dynamics method is appropriate to study the non-equilibrium systems and kinetic phenomena [5].

The molecular dynamics method can be summarized by the following steps [35, 44];

1. Initial coordination of atoms is defined with other simulation parameters such as cut-off distance, time-step, and potential function parameters.
2. The energy of the system is calculated.

$$\phi = \phi\left(r_1, r_2, r_3 ... r_N\right) = \mathrm{E} \tag{2.6}$$

3. The velocity of the particles is determined by Maxwell distribution for the specified temperature.
4. Particles are moved to a new position for a time step (dt) and the energy for the new configuration is calculated.
5. By using equation 2.7, forces are calculated by the gradient of the inter-atomic potentials as a function of atomic positions. Also, by using equation 2.7, velocities of the particles are derived.

$$F_i = -\nabla_i \phi = m_i \frac{dv_i}{dt} \tag{2.7}$$

6. Iteration continues until the equilibrium is reached. The variation of energy of the system with respect to molecular dynamics time step is shown in Figure 2.1

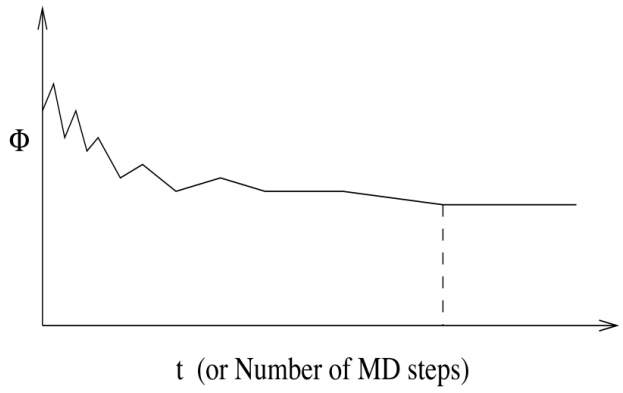


Figure 2.1: The variation of energy of the system with respect to molecular dynamics time step [5]

The accuracy and reliability of molecular dynamics simulations depend on the selected atomistic interaction potentials for calculations.

#### 2.1.3.1 Inter-Atomic Potential Energy Functions

Many of these simulation techniques (atomistic-level simulations) such as molecular dynamics, Monte–Carlo, static (energy and/or force minimization), and lattice–dynamics, are based on potentials which describe interactions between atoms in the system [44].

Inter-atomic potential energy functions are important to describe the atomic interactions to increase the accuracy of the simulation and to decrease the computational effort for complex systems [45]. The concept of the inter-atomic potentials mainly relies on the Born-Oppenheimer approximation which is briefly described in the quantum mechanical methods.

The total energy of a system is expressed as the equation 2.8 if the external energy is neglected [35].

$$\mathrm{E}_N = \phi_1 + \phi_2 + ... + \phi_n + ... \tag{2.8}$$

In this expression, $\phi_1$ represents the total energy of non-interacting particles; $\phi_2$, $\phi_3$ and $\phi_n$ represent the total energy of two, three, and n-body interactions, respectively. Therefore, total interaction energy of a system with N interacting particles as a function of their positions is shown in the equation 2.9 [35].

$$\phi\left(r_1, r_2 ... r_N\right) = \mathrm{E}_N - \phi_1 = \phi_2 + \phi_3 ... + \phi_n + ... \tag{2.9}$$

Here, the interaction energies of N particle systems are expressed in term of many-body interactions, $U_n$ [35].

$$\phi_n = \sum_{i<j<k<..<n} U_n\left(r_i, r_j, r_k, ..., r_n\right) \tag{2.10}$$

For the atomistic-level simulations, there are several inter-atomic potential energy functions to determine the different properties of the systems. The inter-atomic potentials are mainly classified into two categories; empirical inter-atomic potentials and semi-empirical potentials [18].

In empirical potentials, the pair interactions are considered and others are neglected (Lennard-Jones potentials). This approximation is also called as a first-order approxi-

mation and it is usually applicable for rare gases rather than metallic systems [46, 44]. In pairwise inter-atomic potentials, atoms are considered as neutral and point–like particles which means electronic information or angular momentum is not counted.

On the other hand, some potentials consider multi-body interactions (like four or five body interactions) or many-body effects (like angular momentum). For example, embedded atom model depends on the density functional theory to calculate the ground-state properties of metal systems [35].

Generally, inter-atomic potentials are applicable in infinite range; however, it is important to establish a cut-off radius. When a cut-off radius ($R_c$) is defined, interaction between a pair of particles is ignored, if the distance between the particles is greater than $R_c$ [44].

#### 2.1.3.2 Geometrical Constraints

For molecular dynamics simulation, a system is defined in a simulation box with a specified size which is determined by boundary conditions. Generally, there are two types of boundary conditions. First one is isolated boundary condition (IBC) which is applicable especially for clusters and molecules. The second one is periodic boundary conditions (PBCs). PBCs are useful for bulk solids and liquids [7].

Periodic boundary condition which is illustrated in Figure 2.2 is necessary to remove surface effects and allows the study of infinite systems. If PBC is defined in the simulation, particles are placed in a box which is surrounded by its replicas. Therefore, the interaction between particles in the box represents also the interaction between their images in neighboring boxes [44].

#### 2.1.3.3 Canonical Ensemble

For the simulation of large systems, several differential equations should be determined with a degree of freedom of each atom. In order to handle this complexity, ensemble theory is applied, which defines the characteristic of all whole system. Main ensembles for molecular dynamics simulation are the microcanonical ensem-

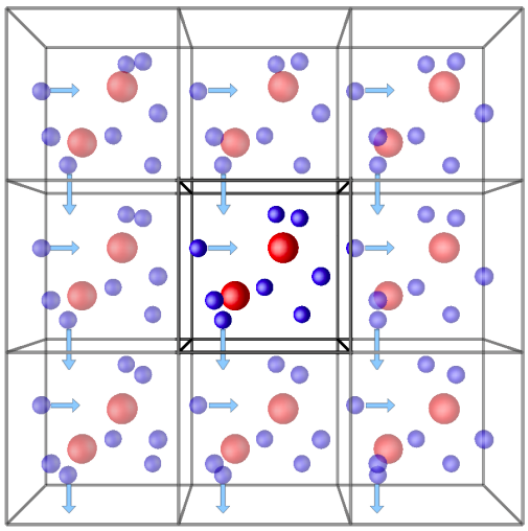

Figure 2.2: Illustration of the periodic boundary condition [6]

ble, canonical ensemble, grand canonical ensemble and isothermal-isobaric ensemble [7, 47].

In the microcanonical ensemble (NVE), the number of atoms, volume, and total energy remains constant. Usually, isolated systems are described with the microcanonical ensemble. In classical molecular dynamics, the microcanonical ensemble is used.

In the canonical ensemble (NVT), the number of atoms, volume, and temperature are kept fixed by interacting the system to a thermostat. In general, the canonical ensemble is used to observe the system at a specific temperature [48].

Also, in the grand canonical ensemble ($\mu$VT), chemical potential and temperature remain constant.

In the isothermal-isobaric ensemble, both the temperature and the pressure are kept constant during simulation using both thermostat and barostat [7, 47]. Most of the experiments are conducted under non-isolated, constant temperature and pressure conditions; therefore, the isothermal-isobaric ensemble is very useful to reproduce laboratory conditions. Also, NPT ensemble is important to compute equilibrium properties under isobaric condition [49].

In order to simulate and obtain the behavior of the system from these ensembles,

different combinations of thermostats and barostats can be used, such as Anderson, Brendsen, Nose-Hoover, Parrinello-Rahman and Langevin thermostats and barostats. However, in molecular dynamics simulations, mainly Nose-Hoover is used.

In Nose-Hoover thermostat, the thermal relaxation time is controlled to reach an equilibrium state with the desired temperature. If the relaxation time is high, the heat flow decreases and the system becomes over-damped. On the other hand, if it has a low relaxation time, the temperature may fluctuate.

#### 2.1.3.4 The Time Integration Algorithms

Molecular dynamics is a time-dependent method, and it needs to integrate the equation of motion. Although there are different integration algorithms with some advantages and disadvantages, the most common integration method for molecular dynamics is Verlet algorithm. By the help of the Verlet algorithm, simple, accurate and long-term stable results are derived for the specified ensembles in molecular dynamics [44].

Verlet algorithm, which is obtained by the summation of forward and backward Taylor expansion for the position r(t), is shown in the following equations [44, 50].

$$r\left(t+\Delta t\right)=2r\left(t\right)-r\left(t-\Delta t\right)+a\left(t\right)\Delta t^{2}+O\left(\Delta t^{4}\right) \tag{2.11}$$

Here, a is acceleration and $O\left(\Delta t^{4}\right)$ is the truncation error which is related to the accuracy of the method compared to the true solution [44].

Since equation of motion is required to be integrated (equation 2.7), the steps of the Verlet algorithm for the molecular dynamics simulations start with the approximation of acceleration which is derived from the equation 2.7.

$$a\left(t\right)-\frac{1}{m}\nabla\phi\left(r\left(t\right)\right) \tag{2.12}$$

The velocity of the particles is derived from kinetic energy in the standard Verlet algorithm, so according to the dependence of the accuracy on velocity, some variants of Verlet algorithm have been developed, such as the leap-frog algorithm or the velocity Verlet scheme.

## 2.2 Previous Studies

Computer simulation techniques have been widely used to investigate structural properties of the Fe-Ni based bulk and nanostructured alloys for a long time. Atomic and magnetic ordering, order-disorder and ferromagnetic-paramagnetic transformation characteristics and also interrelation between atomic and magnetic ordering phenomena in binary $FeNi_3$ and ternary $Ni_3$(Fe, Me) (Me= W, Mo, Cr, Mn, Nb, etc.) bulk intermetallics have been widely investigated in terms of classical theory of ordering and electronic theory of binary and multicomponent alloys in ab-initio pseudopotential approximation by A.O. Mekhrabov and co-workers [51, 52, 53, 54]. Although the first principle calculations on the Fe-Ni based alloys have been used to predict the properties from atomistic level [55, 30], the molecular dynamics simulations with many-body potentials are mainly preferred because of its applicability to the large systems having more than hundreds of atoms.

Furthermore, the accuracy and consistency of embedded atom model (EAM) based potentials for Fe-Ni systems have been tested with experimental or DFT studies or other potentials in the literature. Even though the applicability EAM potentials for the metallic systems has been examined [56, 57, 58] to study the structural properties of the Fe-Ni bimetallic systems, some optimizations needed to achieve more accurate results.

Grujicic et al. [59] studied on the FCC to BCC martensitic transformation of the Fe-Ni bulk alloys by using MD simulations with EAM pseudomonoatomic potential in which Fe and Ni atoms were considered as identical atoms to investigate the stability of the BCC and FCC structures. Meyer and Entel [60] also developed a potential that relies on EAM based potential to exhibit the stability boundaries of the martensite-austenite transition as a function of Ni content by molecular dynamics technique. Moreover, Mishin et al. [30], worked on a new semi-empirical potential, angle-dependent potential, which is the combination of the EAM potential with the bond-angle dependencies, by fitting the data from the first principle calculations to reproduce the formation energies and structural properties. Finally, Bonny et al. [29], developed EAM based potential in order to reproduce the Fe-Ni phase diagram for whole concentration range, defect energetics and vacancy migration barriers. It

has been seen that the equilibrium phase diagram and defect properties of Fe-Ni system were in agreement with the DFT calculations, other potentials and experimental results in the literature.

While several molecular dynamics studies with embedded atom model have been carried out for the Fe-Ni bulk systems, there is limited available literature for the determination of the structural properties of Fe-Ni nanosystems in molecular dynamics simulations with EAM based models. On the other hand, Kadau et al. [61] studied on the martensitic transformations of the Fe-Ni nanoparticles (having more than 1000 atoms) via first molecular-dynamics simulations with the embedded-atom model (EAM) proposed from Meyer and Entel [60] and NPT ensemble. By applying NPT ensemble (0 GPa and 800 K) the system was relaxed for 0.1 ns and 0.58 ns. Longer relaxation led to about 98% of the ideal density of a single crystal, but the faster one caused amorphous zones. Also, the martensitic transformation was observed at the grain boundaries from radial distribution function by cooling down the polycrystalline solid from 800 to 25 K, gradually.

Recently, Byshkin et al. [62] studied to investigate the BCC/FCC phase transformation and segregation properties for the varying compositions and temperatures of the Fe-Ni bimetallic bulk and nanosystems in molecular dynamics and Metropolis Monte Carlo method (MMC) with EAM based model. MMC method was utilized to examine the stable phases of the bulk and nanoparticles in Fe-Ni phase diagram. Besides, MD simulations were performed to demonstrate the kinetic path of FCC to BCC and BCC to FCC transformation because MD considers velocity effect on the structural evolution in addition to the configuration of the atoms. The order-disorder transition of $L1_2$ and $L1_0$ structured Fe-Ni nanoparticles with 1289 atoms occurred at about 950 K. The nanoparticles owing 1289 atoms and the Ni fraction close to 0.2, exhibited a core-shell structure where the core was $L1_0$ and shell was pure Fe. Above 0.2 Ni fraction, phase separation occurred and the $L1_0$ core structure dominated the particle

Moreover, Guojian Li et al. [63] observed the BCC/FCC phase transformation in Fe-Ni nanoparticles (1639 atoms) with different structures, sizes and varying Ni content during heating by molecular dynamics simulation with an embedded atom method for the nanoparticles. According to the study, the melting points of the Fe–Ni nanopar-

ticles with different initial structures and Ni contents were determined. Clearly, the melting point decreased with higher Ni content. It has been proven that the transition was dependent on the Ni content; for example, BCC structure was the stable form for the low Ni fraction, but FCC was the stable phase for the higher Ni content.

## 2.3 Methods and Simulation

In this chapter, the structural evolutions of Fe-Ni based nanoalloys were studied by using molecular dynamics simulations in LAMMPS.

MD simulations were performed with the embedded atom model (EAM) which is capable of describing Fe-Ni bimetallic systems. EAM is based on the density functional theory and it considers many-body interaction because of the electron density in the system. Therefore, EAM gives more accurate results than the pairwise interaction models with reasonable computational time for Fe-Ni systems [29].

According to EAM model, the energy of the system which consists of N-atoms is expressed as equation 2.13.

$$\mathrm{E} = \sum_{i} F_i\left(\rho_i\right) + \frac{1}{2}\sum_{ij} V_{ij}\left(r_{ij}\right) \tag{2.13}$$

$$\rho_i = \sum_{i \neq j} \psi\left(r_{ij}\right) \tag{2.14}$$

Here, $\mathrm{F}_i$ represents the embedding function which depends on the electron density ($\rho_i$) and many body interaction of the system. $\mathrm{V}_{ij}$ denotes the pair potential as a function of the distance between atoms and $\psi$ is the electronic potential function. In equation 2.13, i and j represent the different atoms, rather than the different type of atoms.

For an accurate description of a system, the potential parameters should be fitted to the thermodynamics, kinetics and defect interactions of each system. In this study, the EAM parameters formalized by Bonny et al. [29] were utilized to investigate the structural evolution of the $\mathrm{FeNi_3}$ system. In Figure 2.3-Figure 2.5, the EAM pair

potential interaction, embedding energy and electron density graphs are shown for the given parameters of $FeNi_3$. According to the pair potential interaction graph, the cut-off distance identified as 5.0 Å for the molecular dynamics simulations.

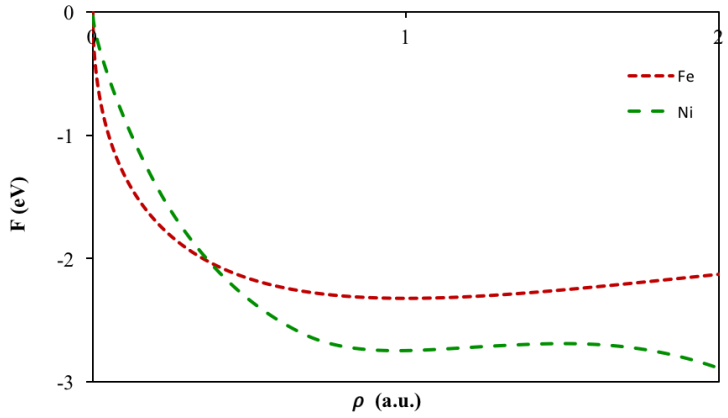


Figure 2.3: Embedded energy change with respect to electron density of Fe-Ni system

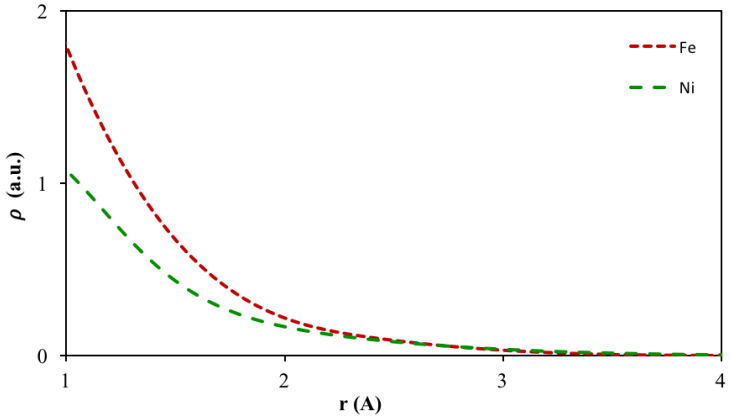


Figure 2.4: Electronic density change with respect to the distance between atoms in Fe-Ni system

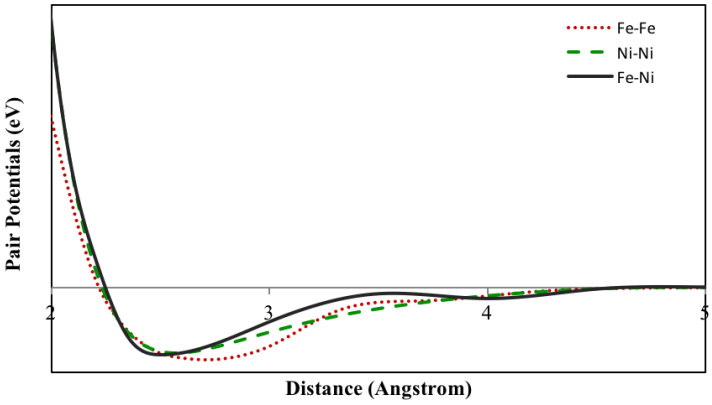


Figure 2.5: Pair interaction change with respect to the distance between atoms in Fe-Ni system

During solving of the equation of motions of atoms in MD, Verlet algorithm was considered with Nose-Hoover thermostat and barostat. Among the ensembles typically used for molecular dynamics, namely the microcanonical (NVE), canonical (NVT) and isothermal–isobaric (NPT) ensembles, the NPT ensemble was applied in this study because it accurately describes experimental conditions by controlling temperature and pressure at the same time.

The bulk form of $FeNi_3$ alloy, having 27436 atoms, was generated by repeating the $L1_2$ structured unit cell along [111] direction nineteen times. Firstly, the lattice parameter of $FeNi_3$ alloy was optimized and the alloy was relaxed at 0 K under the periodic boundary conditions. Then, the temperature was increased to 2600 K under 1 atm pressure directly with $5x10^5$ steps and the system waited for $5x10^4$ steps. 2600 K is higher than the melting temperature which was enough to homogenize the liquid structure. Then, the temperature decreased to 300 K with 200 K temperature steps and $2.3x10^{11}$ K/sec cooling rate, and at each stage, the system was relaxed until the equilibrium was reached. At 300 K, it was observed that the system had a crystal structure. On the other hand, to obtain the amorphous bulk structure, the system was cooled from 2600 K to 300 K by fast cooling which includes $1x10^5$ steps ($2.3x10^{13}$ K/sec). During the simulations, the time step was specified as one femtosecond.

The nano-systems with more than 100 atoms are assumed to have the same crystal

structure with their bulk counterparts and because our systems have at least 2nm diameter, nanocrystalline $FeNi_3$ alloys were modeled with this assumption. Size and the shape of the nanoparticles, thus the number of atoms of each nanoparticle varied. Three different spherical crystalline nanoparticles with diameter 2 nm, 4 nm, 6 nm and one crystalline nanoparticle with cubic structure (the length of one edge was 2.8 nm) were prepared (the total number of atoms are 360, 2952, 10168 and 2048, respectively). For generating the crystalline nanoparticles, MEDEA software was used. The temperature dependence of the structural evolution was investigated by raising the temperature to 1700 K with 200 K temperature intervals under vacuum condition. Before the simulation of each particle, the systems were relaxed by the conjugate-gradient energy minimization method.

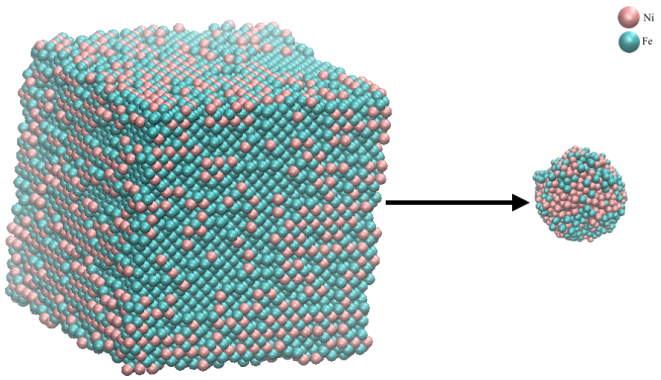


Figure 2.6: Amorphous nanoalloy which is subtracted from the bimetallic bulk alloy

However, during the simulation of the amorphous nanoalloys, a different method was applied. Firstly, a nanoparticle was subtracted from the simulated amorphous bulk alloy (Figure 2.6). Nonperiodic boundary condition was applied to simulate the amorphous bimetallic $FeNi_3$ nanoparticle. Then, the subtracted nanoparticle was melted and equilibrated at 1900 K in order to remove local atomic configurations from the solid phase. Finally, the temperature of nanoparticle was decreased to room temperature, gradually. To obtain accurate results from molecular dynamics simulations, we needed to decrease the temperature of the amorphous particles with the same cooling rate ($2x10^{12}$ K/sec) and equilibrate the system at each stage by waiting for 10 nanoseconds. The simulations of the amorphous nanoalloys were conducted for 2

nm, 4 nm and 6 nm diameters (the total number of atoms are 368, 2913 and 9784, respectively).

The radial distribution function (RDF) can be used to verify the structure evolution of bulk and nanostructured alloys during heating and cooling. Considering a homogeneous distribution of the atoms in space, the RDF represents the probability to find an atom in a shell (dr) at the specified distance (r) of another atom chosen as a reference point. The illustration of the radial distribution function determination is shown in Figure 2.7. Therefore, the structure formation, development, and stability of the amorphous and crystalline $FeNi_3$ cubic and spherical nanoparticles with 2-6 nm diameters were investigated by calculating radial distribution functions at a wide temperature range (300-1700 K). Additionally, the lattice constant for each particle has been calculated by using the second peak in radial distribution functions at 300 K [64].

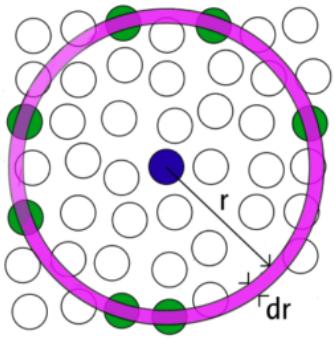


Figure 2.7: The illustration of the radial distribution function determination [7]

Although radial distribution functions commonly use 2-D functions to represent the 3-D atomic distribution of the nanoalloys, sometimes they remain incapable of describing several structures. Voronoi analysis gives distribution function of the polyhedral structure of space closer to an atom than any other particle, so it defines the characteristic arrangement of near neighbors [65]. Amorphous structures, unlike crystalline ones, do not have periodic and symmetric atomic arrangements; thus, Voronoi analysis is important to define the polyhedral types and local atomic configuration of the amorphous nanoparticles which has lack of long-range order. In this regard, Voronoi

tessellation analysis was implemented to investigate the local atomic structures in the amorphous systems, but Voronoi analysis was also applied to the crystalline nanoparticles in order to investigate any distortion in the crystalline structure and to compare the polyhedral structures in the crystalline and amorphous nanoparticles.

In this study, Voronoi polyhedrons were obtained by using OVITO's Python scripting. It is known that Voronoi polyhedra become unstable when small perturbations occur, so the modifier of the OVITO provides threshold length and area to eliminate very small and almost degenerate faces and edges [66]. As an output of the Voronoi tessellation analysis, local symmetry around each atom is indexed by vector indices ($n_3$, $n_4$, $n_5$, $n_6$), where $n_i$ represents the i-edged faces of the Voronoi cell [67]. Some examples for the Voronoi polyhedra are shown in Figure 2.8.

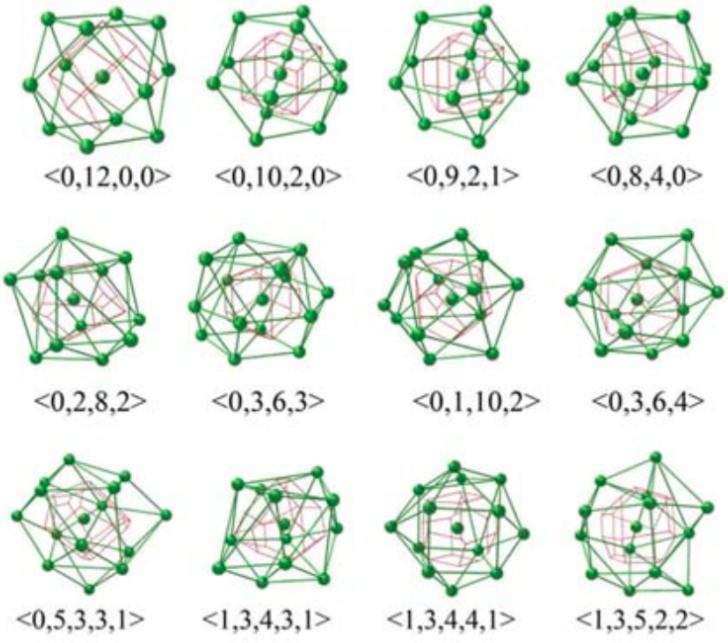


Figure 2.8: Some examples for the Voronoi polyhedra. The local structures and their Voronoi cells are illustrated with green and red lines, respectively [8]

.

Although the most common polyhedron indices are listed from the Voronoi analysis, it is difficult to interpret a definite polyhedron type because small perturbations lead to the distortion in the polyhedral forms. Therefore, it is essential to determine the

ratio of the i-edged faces to the total number of the faces in a polyhedron to investigate the main polyhedral forms in the particles [68].

Moreover, the Voronoi tessellation is important to determine the coordination numbers (CN) which is related to the lattice structure. Coordination number is the number of contacted particles and it is hardly measured experimentally, so obtaining CN by computational methods is very important. CN can be measured by the integration of the first peak in the radial distribution function graphs; however, this calculation method strictly depends on the cut-off value that is set during molecular dynamics method. On the other hand, the total coordination number can be calculated from the summation of the indices in Voronoi tessellation. CN determined from Voronoi analysis usually has a higher or equal value because it considers both the contacted particles and the other particles which are geometrically sharing a common Voronoi face [8].

Also, to verify the structure of the nanoparticles and observe the change in atomic positions during heating or cooling process, core-to-surface concentration profiles were determined. For this purpose, firstly, the center of mass (CM) of each sphere was calculated. Then, the origin is shifted to the center of mass and the distances of each of atoms with respect to the origin were calculated. Finally, the number of the two constituent atoms with respect to the origin was obtained.

Surface energy is one of the most important parameters for free nanoparticles because it is strongly size and shape dependent. The surface to volume ratio becomes higher as the particle size decreases which influences kinetics and thermodynamics of processes at the surface of the material. Also, surface energy represents the stability of the nanoparticles that affects the oxidation or degradation behavior of the particles. Although the underlying theory for the surface energy and surface tension of liquids has been clarified, many studies for the surface energy and surface properties of the nano solids are not completely compatible with each other, but generally, the surface energy increases as the size of the free nanoparticle decreases. To determine the size, shape and temperature dependent surface energy of the nanoparticles, the computational studies are critical. In this study, surface energy was calculated by using equation 2.15 [69].

$$\mathrm{E}_{surface} = \frac{\mathrm{E}_{p,nanoparticle} - N\mathrm{E}_{p,bulk}}{A_{nanoparticle}} \tag{2.15}$$

Here $\mathrm{E}_{surface}$ and $\mathrm{E}_{p,nanoparticle}$ are the surface energy and the potential energy of the nanoparticle, respectively. $\mathrm{E}_{p,bulk}$ is the potential energy per atom in the bulk system, N is the total number of atoms in the nanoparticle and A represents the surface area of the particle.

Moreover, melting points of the crystalline $FeNi_3$ nanoparticles with respect to different size has been determined from the heating of the nanoparticles to 1900 K and the point at the sharp variation of the total energy of each particle with temperature gave the melting point.

Finally, visualization of results of the nanoparticles was illustrated by using VMD molecular graphics program to investigate the morphological change during heat treatment.

## 2.4 Results and Discussion

### 2.4.1 Structural Properties and Radial Distribution Function for the $FeNi_3$ Bulk System

Before the investigation of the structural evolution of the $FeNi_3$ bulk system, the lattice parameter was optimized. In this regard, crystal structures were generated with different lattice parameters (from 3 Å to 4 Å). Then, the systems were minimized by conjugate gradient method in MD, and the total energies of the crystal structures were calculated. Afterward, the crystal structure owing to the minimum total energy was obtained with the lattice parameter, a=3.46 Å. Then, the input file of the $FeNi_3$ bulk system was prepared according to the minimized lattice parameter, a=3.46 Å. The total energy change with respect to the various lattice parameters is shown in Figure 2.9.

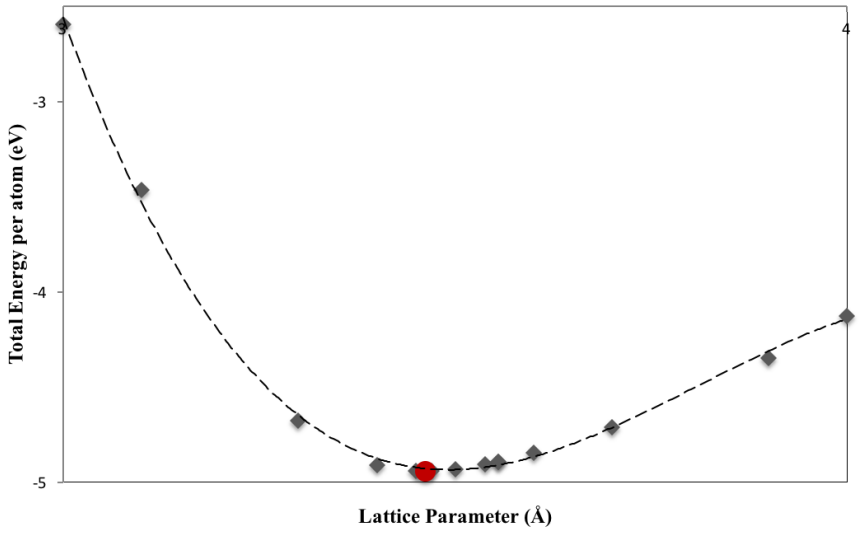


Figure 2.9: The total energy change according to the various lattice parameters for the Fe-Ni system

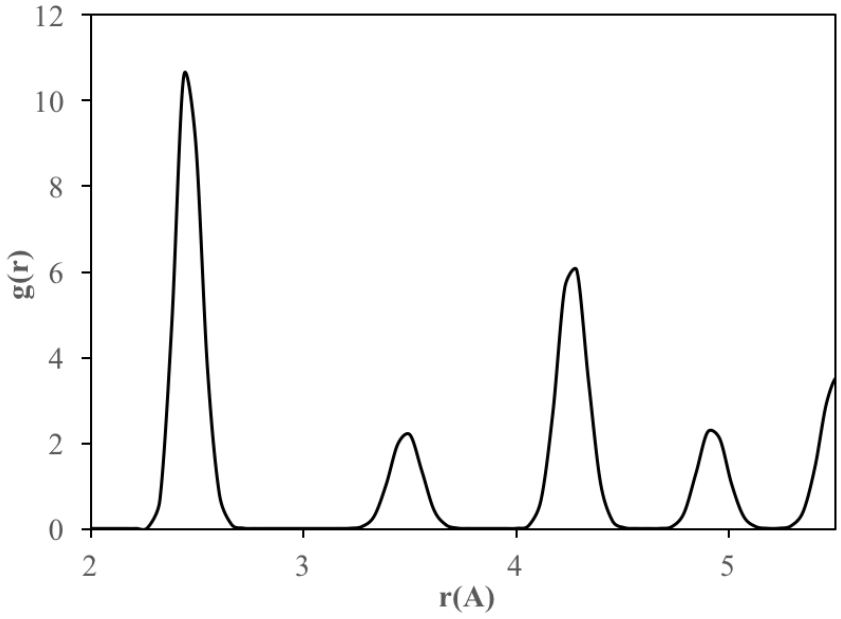


Figure 2.10: Radial distribution function of the crystal $FeNi_3$ bulk alloy

RDF for the crystalline bulk phase of $FeNi_3$ system after slow cooling is illustrated in Figure 2.10. The RDF of the crystal bulk structure had a regular structure and there

wasn't any possibility of finding a particle between the peaks.

The location of the first peak in RDF graph corresponds to the nearest inter-atomic distance which was estimated as 2.44 Å at 300 K. The location of the second peak, which corresponds to the alloy lattice parameter was found to be 3.50 Å. This proves that the final bulk structure is $Ll_2$ type a face-centered cubic lattice.

To obtain the amorphous bulk structure, the system was cooled from 2600 K to 300 K by fast cooling with $2.3x10^{13}$ K/sec cooling rate. The volume change during heating and fast cooling for the bulk $FeNi_3$ alloy is shown in Figure 2.11.

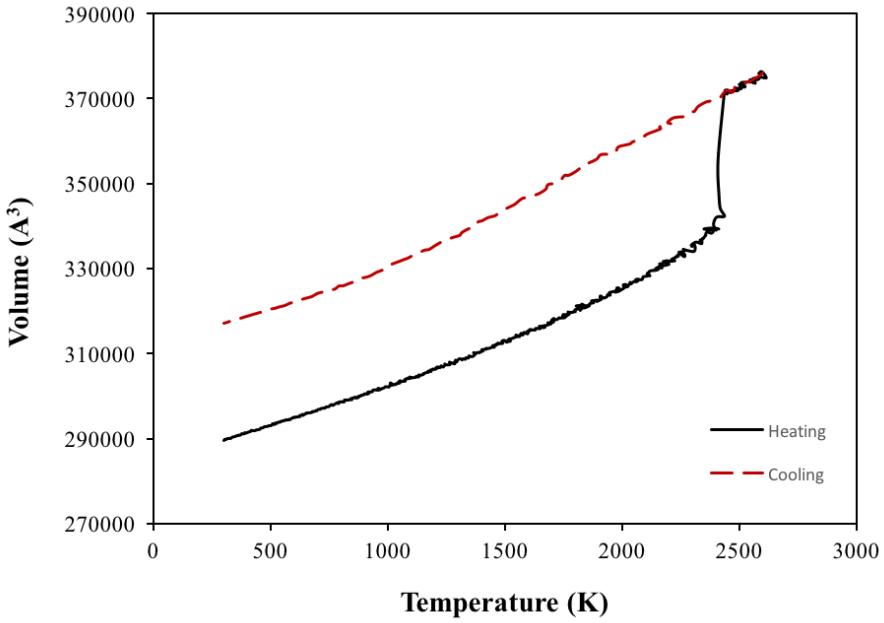


Figure 2.11: The volume change during heating and fast cooling processes of the $FeNi_3$ alloy

During the heating process, there was a sudden jump in the volume curve which is the sign of the melting. However, we did not observe any sudden change in the volume during fast cooling with $2.3x10^{13}$ K/sec rate, which indicated that no crystallization occurred and the amorphous structure was preserved at room temperature. Also, this amorphous structure was proven by the radial distribution function which is illustrated in Figure 2.12.

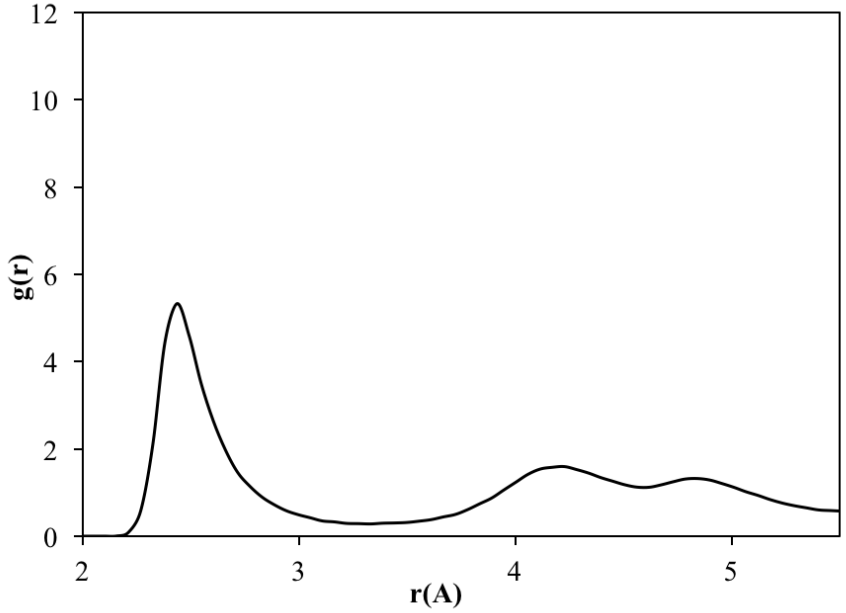


Figure 2.12: Radial distribution function of the $FeNi_3$ amorphous bulk alloy

The coordination numbers and neighbor distances of the amorphous and crystal structures of the bulk $FeNi_3$ alloy are tabulated in Table2.1. The total coordination number of the crystalline structure obtained from the radial distribution function was 12 which is the sign of having FCC lattice, but according to Figure 2.12, the amorphous structure of $FeNi_3$ alloy had 13.2 coordination number.

Table 2.1: The coordination numbers and neighbor distance of the amorphous and crystal structure of the bulk $FeNi_3$ alloy

| | $N_{Fe-Fe}$ | $N_{Fe-Ni}$ | $N_{Ni-Ni}$ | $d_{Fe-Fe}$ | $d_{Fe-Ni}$ | $d_{Ni-Ni}$ |
|---|---|---|---|---|---|---|
| Amorphous Structure | 4.3 | 9.0 | 10.2 | 2.5 | 2.4 | 2.4 |
| Crystal Structure | 6.0 | 12.0 | 8.0 | 3.5 | 2.4 | 2.4 |

### 2.4.2 Structural Properties of the $FeNi_3$ Nanocrystalline Systems

#### 2.4.2.1 Radial Distribution Functions

The nanoparticle having the diameter equal to 2 nm consists of 360 atoms in total, with 90 iron atoms and 270 nickel atoms. To study the temperature effect on the structural evolution of the nanoparticles, the temperature was increased from 300 K to 1700 K by 200 K interval. The radial distribution function graphs of the 2 nm crystalline nanoparticle at each temperature are shown in Figure 2.13.

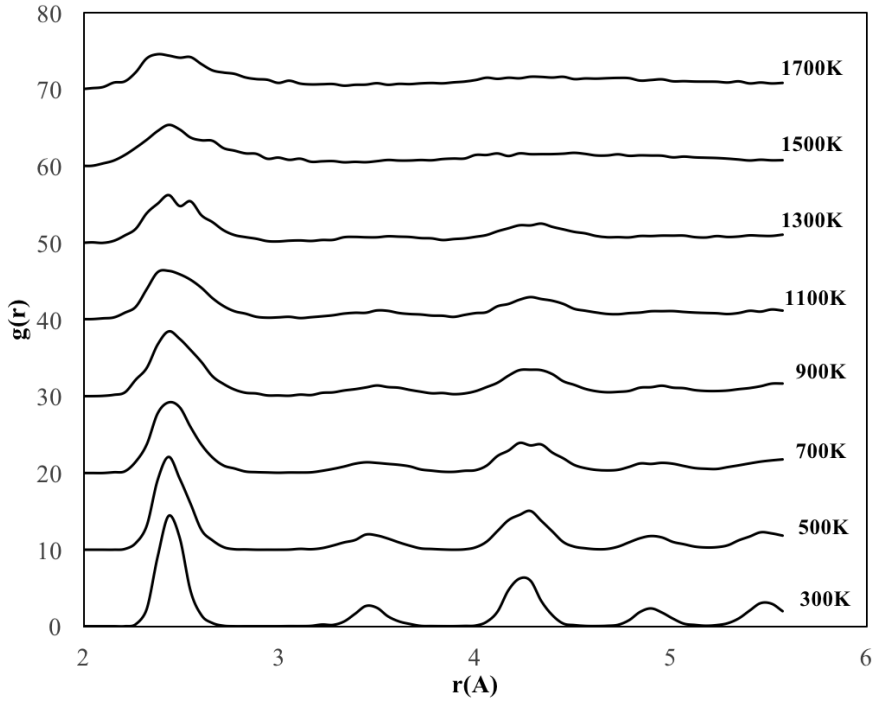


Figure 2.13: RDF graphs of the 2 nm $FeNi_3$ crystalline nanoparticle for different temperatures

As it is seen in Figure 2.13, $FeNi_3$ spherical crystalline nanoparticle with 2 nm diameter kept its ordered structure with 3.44 Å lattice parameter up to 700 K. After that point, the nanoparticle started to lose its initial structure, and a split at the second peak was observed which is the sign of the amorphous structure. After 900 K the outer surface melted, even though the ordered structure was preserved on the inner

part of the nanoparticle until 1300 K. As a result of this, the peak positions remained constant, only the peak shapes broadened, the height of the peaks and the depth of the valley between the peaks decreased. When the temperature reached to 1500 K, the particles melted and the ordered atomic arrangement even on the inner part vanished.

The 4 nm nanoparticle is constituted of 2952 atoms in total, with 738 iron atoms and 2214 nickel atoms. To investigate the temperature effect on the structural evolution of the nanoparticles with 4 nm diameter, the same procedure that applied to 2 nm nanoparticles was repeated. The radial distribution function graphs of the 4 nm crystalline nanoparticle for different temperatures are shown in Figure 2.14.

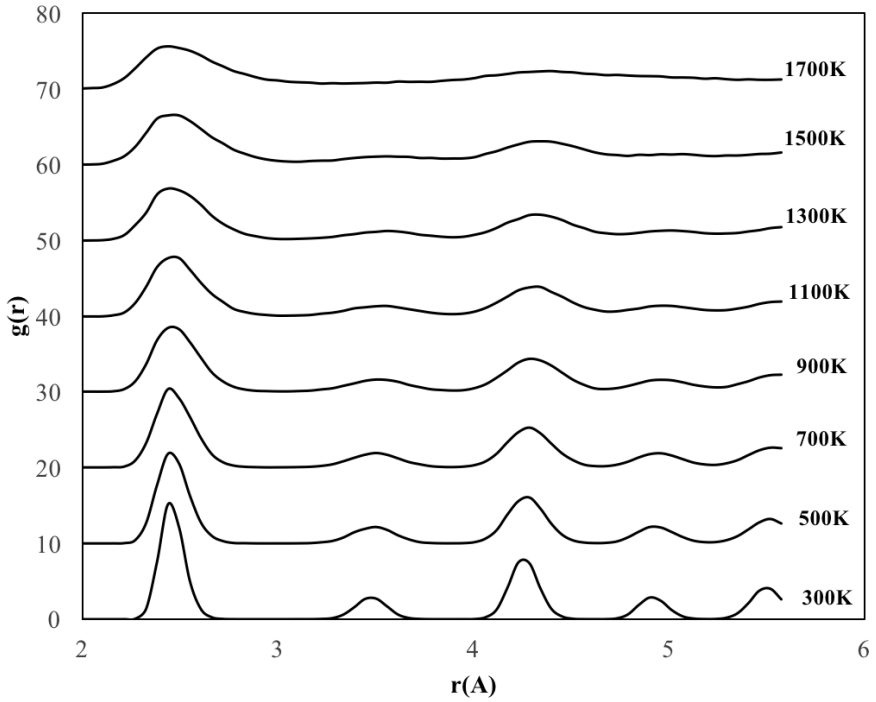


Figure 2.14: RDF graphs of the 4 nm $FeNi_3$ crystalline nanoparticle for different temperatures

The RDFs of the 4 nm crystalline nanoparticle exhibited mainly similar trend with the nanoparticle having 2 nm diameter, but the ordered structure preserved at higher temperatures in the 4 nm nanoparticles. On the other hand, differently from the 2 nm crystalline nanoparticle, no amorphous phase was observed during the heating process. Although the ordered structure started to deform at 1100 K, and consequently

the height of the peaks was decreased and the peak width increased, the peak position of the radial distribution function remained almost constant until 1500 K which shows that the ordered crystal structure was partially preserved till this point. However, at 1700 K, it is seen that the particles melted.

The structural deformation in the 4 nm crystalline was also observed from the lattice parameter change. Until 1100 K, the lattice constant of the crystalline nanoparticle with 4 nm diameter remained constant at 3.5 Å; however, it increased to 3.56 Å later on.

The crystalline nanoparticle with 6 nm diameter includes 2542 Fe atoms and 7626 Ni atoms (10168 atoms in total). For the nanoparticles with 6 nm diameter, the radial distribution function graphs are illustrated in Figure 2.15.

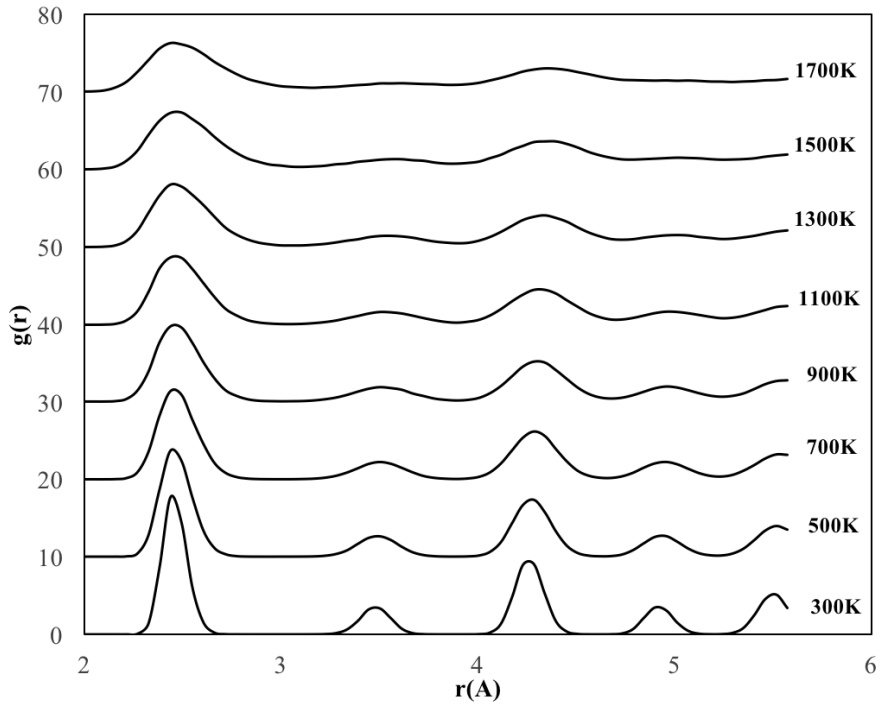


Figure 2.15: RDF graphs of the 6 nm $FeNi_3$ crystalline nanoparticle for different temperatures

According to the RDF of the crystalline nanoparticle with 6 nm diameter, because of the melting at the surface, the depth of the valley between peaks and the height of the

peaks are reduced, but on the inner side of the particle, some ordered atomic arrangement with 3.5 Å lattice parameter was preserved until 1300 K which is the higher than the deformation temperatures of the 4 nm and 2 nm nanoparticles. This means the nanoparticle with 6 nm presented the most stable structure at higher temperatures. After 1300 K, the initial ordered crystalline structure of the nanoparticle with 6 nm diameter started to disappear with increasing lattice parameter.

From the radial distribution functions of the spherical nanoparticles with the crystalline structure, it has been seen that nanoparticles deformed gradually because of the temperature augmentation process. However, as the size of the particle increased, the crystalline nanoparticles preserved their initial structure at higher temperatures due to the decrease in the fraction of surface atoms. For example, although the crystalline nanoparticles with 2 nm diameter started to lose its initial ordered structure at 700 K, the nanoparticles having 4 nm and 6 nm diameter started to deform after 1100 K and 1300 K, respectively.

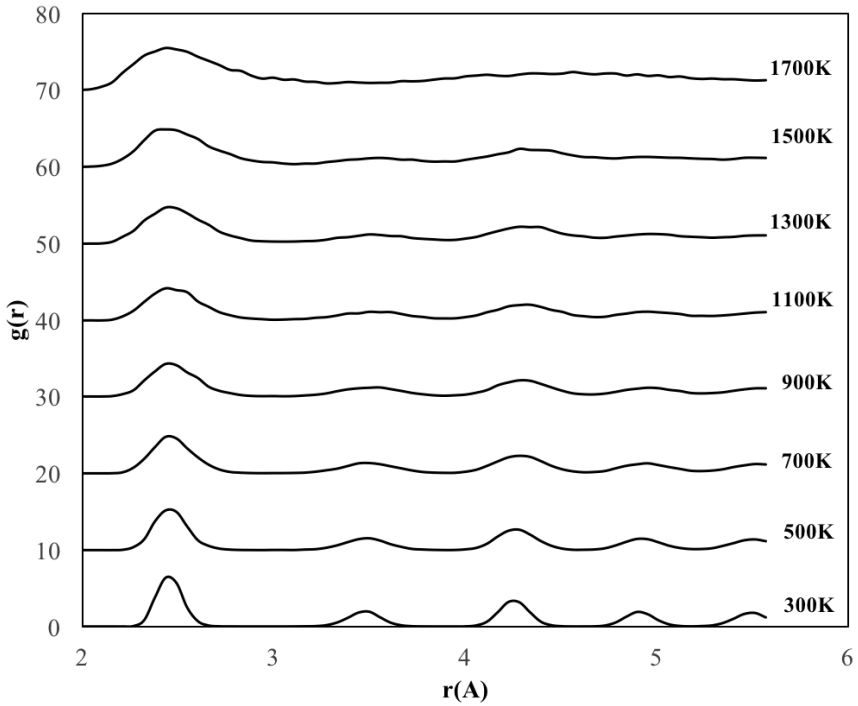


Figure 2.16: RDF graphs of the cubic $FeNi_3$ crystalline nanoparticle for different temperatures

The crystalline nanoparticle with the cubic structure having 2.8 nm length was formed by 2048 atoms in total, with 512 iron atoms and 1536 nickel atoms. The radial distribution function graphs of the nanoparticles with cubic structure are illustrated in Figure 2.16.

According to Figure 2.16, the radial distribution functions showed the similar trend with the 4 nm crystalline nanoparticle as the temperature increased and it started to deform at 1100 K, although the crystalline nanoparticle with cubic structure had fewer atoms than the 4 nm crystalline nanoparticle. This is probably as a result of having the similar initial surface area (43.6 $m^2$) with the surface area of the 4 nm crystalline nanoparticle (42.5 $m^2$). During the temperature augmentation, the crystalline nanoparticle with cubic structure mainly preserved its lattice parameter at 3.5 Å until it melted.

The coordination number (CN) change of the crystalline nanoparticles with respect to temperature is shown in Figure 2.17.

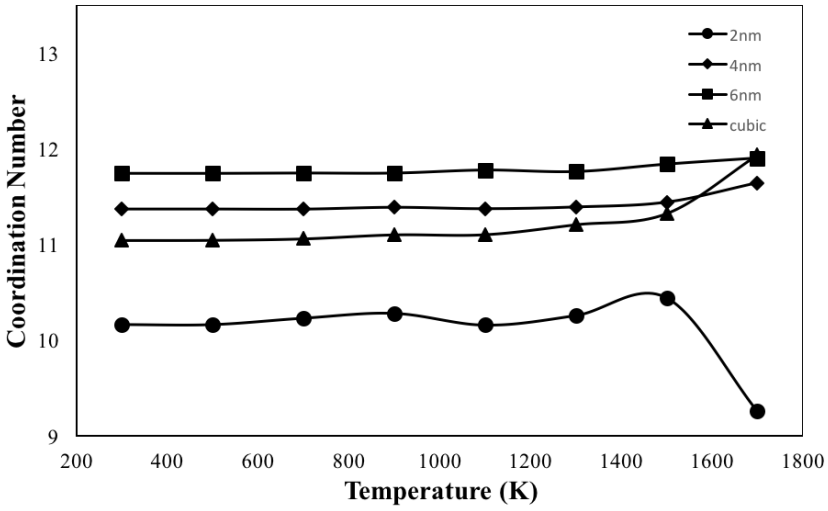


Figure 2.17: Coordination number change of the crystalline $FeNi_3$ nanoparticle with with respect to temperature

According to Figure 2.17, the coordination number of the 6 nm particle was 11.2 at 300 K and remained almost constant between 11.5 and 12 during heat treatment,

which is the closest value to the CN of the $FeNi_3$ with $L1_2$ structure in bulk phase (12) at room temperature. Also, the CN of 4 nm particle also did not change significantly during the heating process, but it stayed lower (around 11) then the CN of 6 nm particle. In the beginning, the cubic nanoparticle had the coordination number of 10.5, but after 1500 K, it got higher dramatically. On the other hand, the coordination number of the particle with 2 nm diameter fluctuated during the heat treatment, and at the end, it reached the minimum value of 8.7. The reason of this is that 2 nm nanoparticle had the highest surface to volume ratio, and the loose structure of the surface atoms probably dominated the system after melting.

#### 2.4.2.2 Spatial Ordering and Morphology

The core-to-surface concentration graphs provide a profile of the spatial ordering of the atoms. The core-to-surface concentration profiles of Fe and Ni atoms in the 2 nm nanoparticle with crystalline structure are shown in Figure 2.18.

From the figures, it has been seen that, in the beginning, the 2 nm bimetallic nanoalloy had an ordered mixed pattern. As the temperature increased, firstly, surface started to melt at 500 K. Then, the ordered structure deformed and Fe atoms started to move towards outer shell of the particle after 700 K. At 1500 K, the particle had a mixed shell of Fe and Ni atoms surrounding the Ni core.

Also, from the morphological view of the nanoparticles, the spherical shape of the 2 nm spherical nanoparticle changed, especially after 700 K. Afterward, the ordered structure with spherical shape completely disappeared by forming a new shape when 1500 K was reached which is consistent with RDF graphs of the 2 nm crystalline nanoparticle.

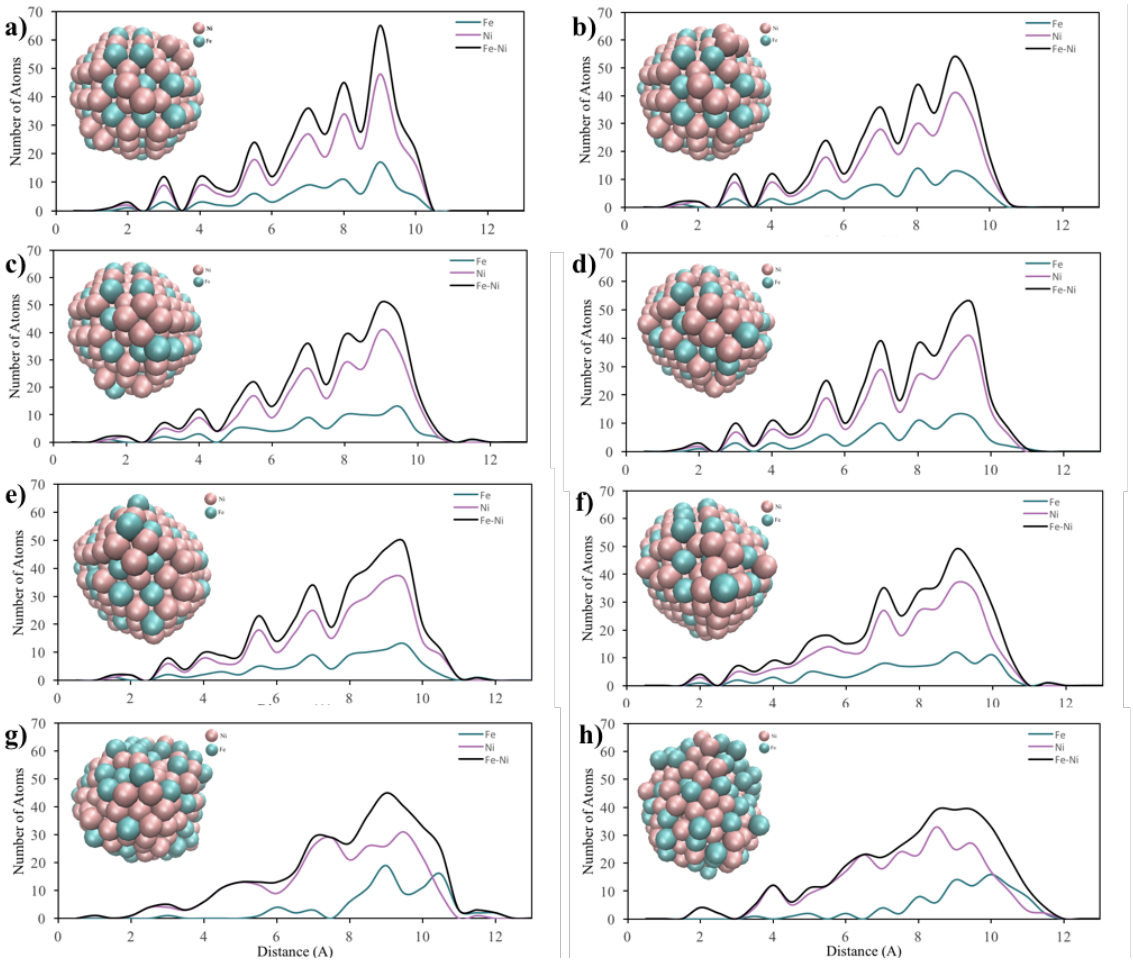


Figure 2.18: Core-to-surface concentration profiles of Fe and Ni atoms in 2 nm crystalline nanoparticles at a) 300 K b) 500 K c) 700 K d) 900 K e) 1100 K f) 1300 K g) 1500 K h) 1700 K

Furthermore, the core-to-surface concentration profiles of the 4 nm nanoparticles with crystalline structure are shown in Figure 2.19.

According to the core-to-surface concentration profile of the nanoparticle with 4 nm, it was observed that although the surface atoms of the ordered mixed nanoparticle started to melt at 500 K, it preserved its cage structure until 1500 K. After that point, a random mixing pattern was obtained throughout the particle with the outer shell composed of mainly Fe atoms. Also, as it can be seen from the visualization of the crystalline nanoparticles with 4 nm diameter, the initial structure started to be lost after 1100 K, and at 1700 K, the spherical structure deformed because of melting.

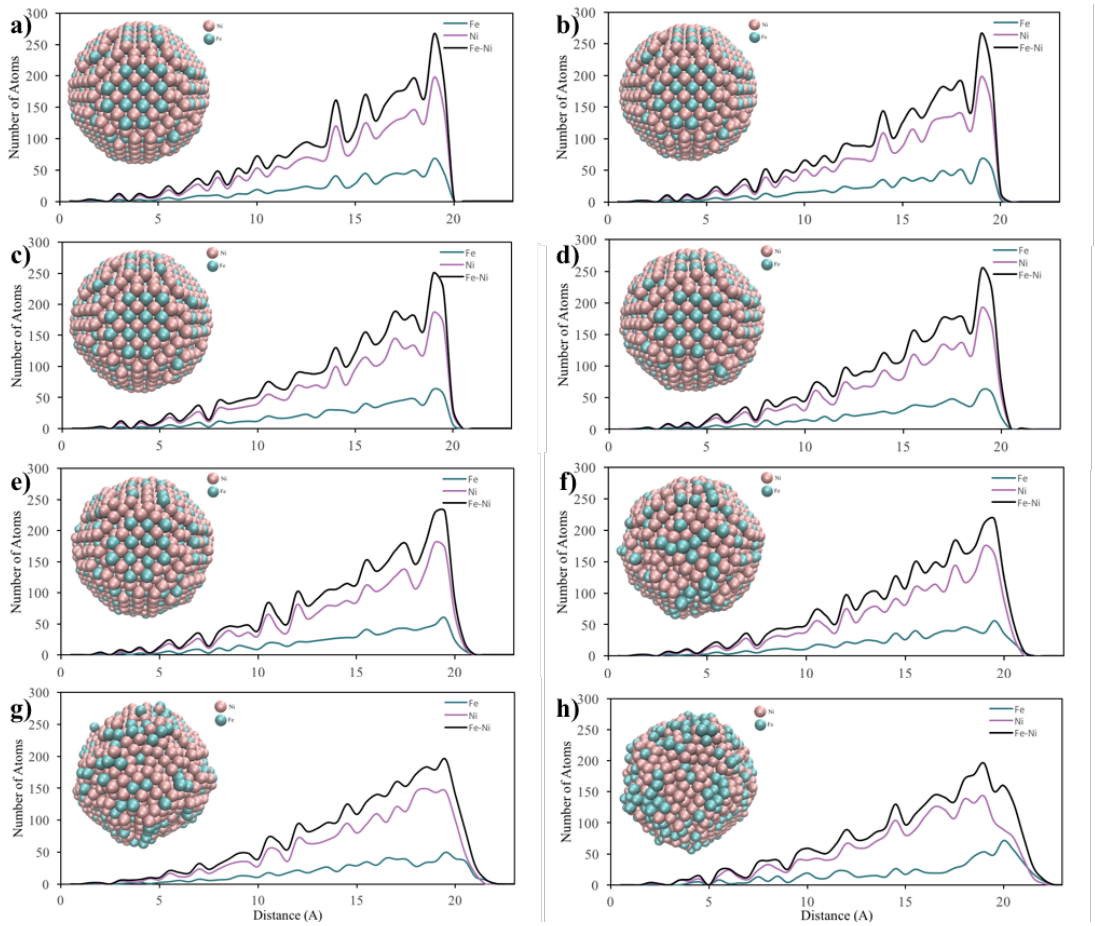


Figure 2.19: Core-to-surface concentration profiles of Fe and Ni atoms in the 4 nm crystalline nanoparticles at a) 300 K b) 500 K c) 700 K d) 900 K e) 1100 K f) 1300 K g) 1500 K h) 1700 K

For the 6 nm crystalline nanoparticles, the core-to-surface concentration profiles are shown in Figure 2.20. In the core-to-surface concentration profile of 6 nm nanoparticle, there was no melting at the surface until 1100 K, but the initial ordered structure remained until 1500 K. After that, although the atomic concentration at the surface changed, some ordered atomic arrangement remained same throughout the particle and no core-shell structure was observed. Moreover, from the morphological view, it was clearly seen that the 6 nm crystalline nanoparticle mostly preserved its spherical shape even at high temperatures.

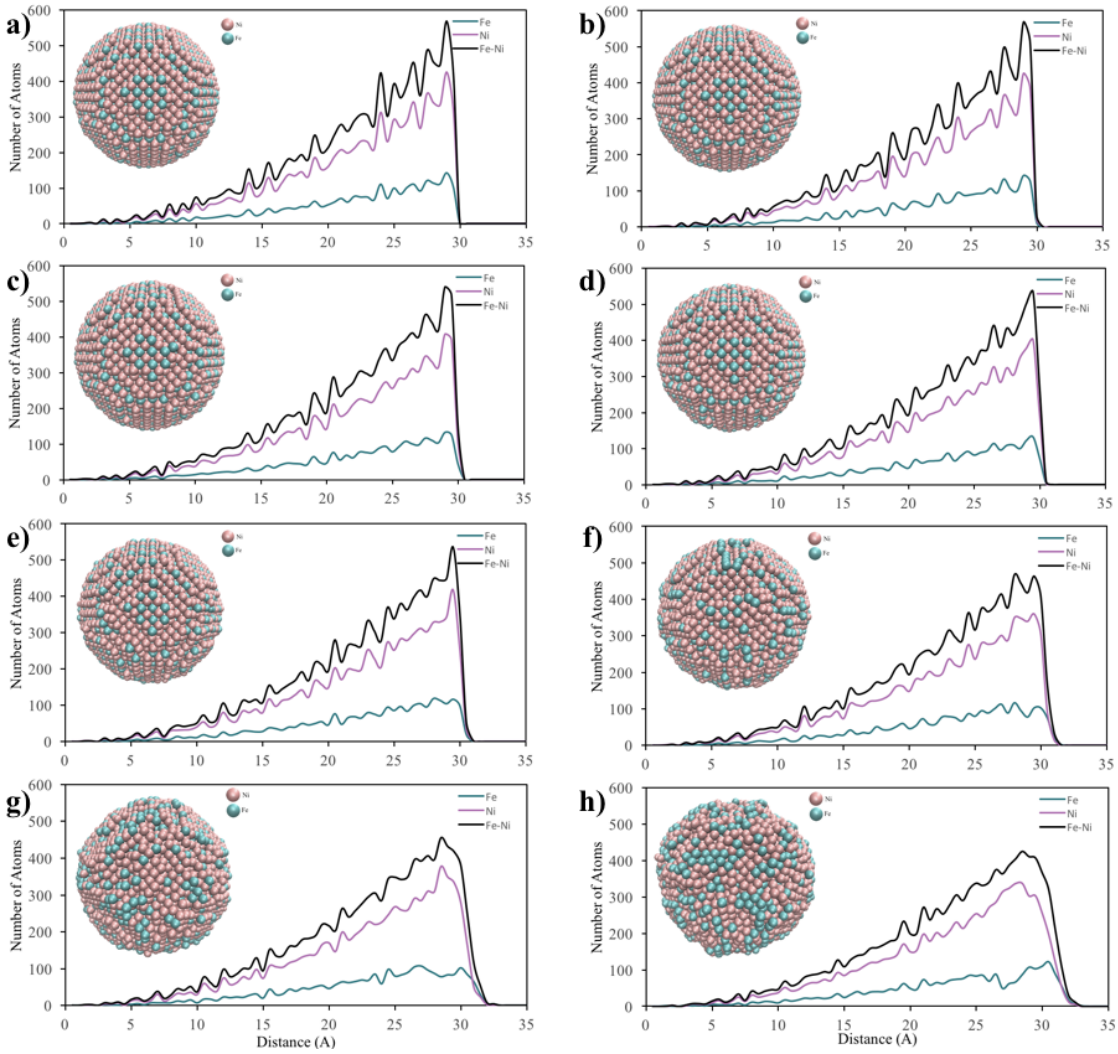


Figure 2.20: Core-to-surface concentration profiles of Fe and Ni atoms in the 6 nm crystalline nanoparticles at a) 300 K b) 500 K c) 700 K d) 900 K e) 1100 K f) 1300 K g) 1500 K h) 1700 K

From Figure 2.21, the initial structure of the cubic nanoparticle with ordered mixing pattern remained same until 900 K. The particle was completely deformed when the temperature reached to 1500 K at which the atomic concentration profile evaluated to the profile of a spherical particle which was covered with Fe atoms at the surface. This deformation mechanism was also proven by the illustrations of the crystalline nanoparticles with cubic structure.

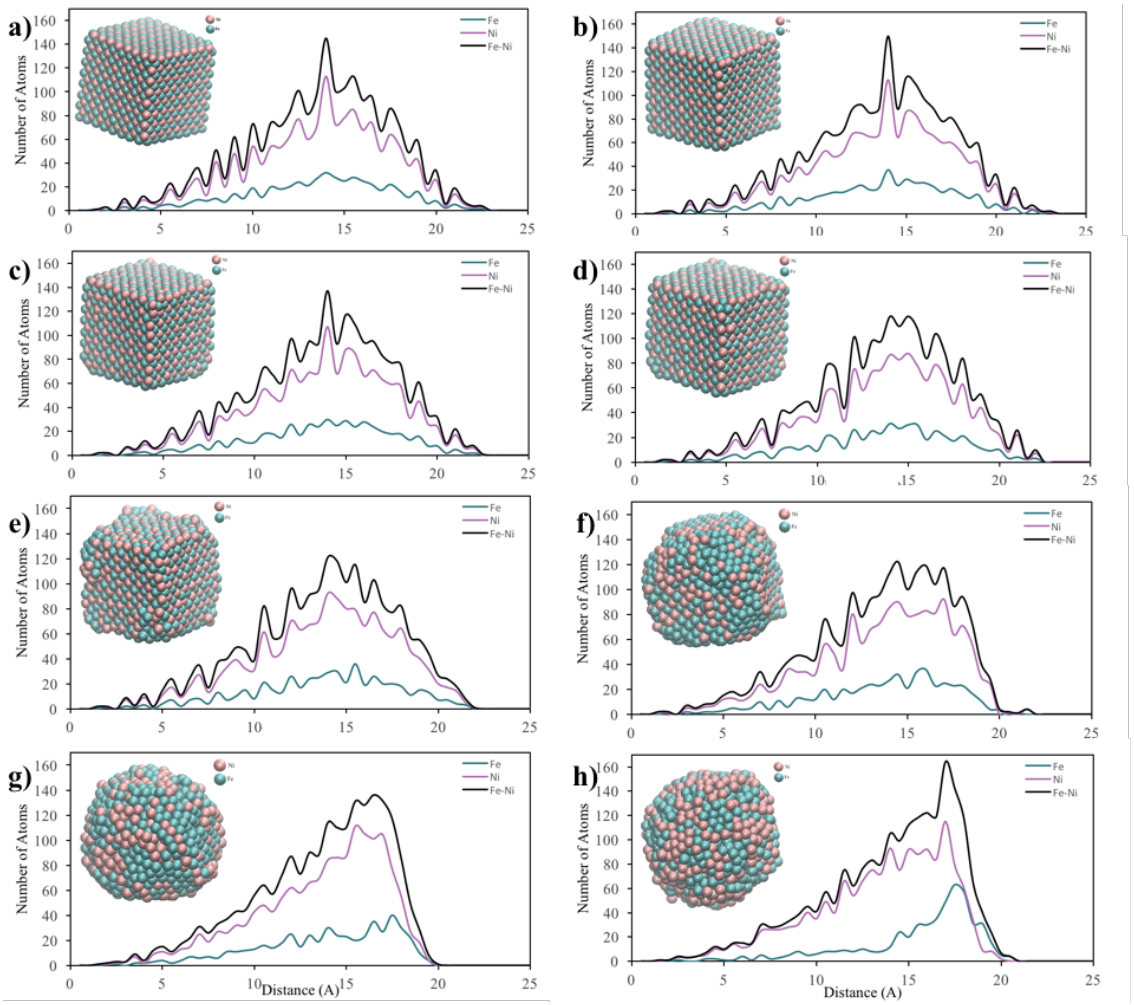


Figure 2.21: Core-to-surface concentration profiles of Fe and Ni atoms in the crystalline nanoparticles with cubic structure at a) 300 K b) 500 K c) 700 K d) 900 K e) 1100 K f) 1300 K g) 1500 K h) 1700 K

Among the core-to-surface concentration profiles of the nanoparticles with different shape and size, it can be deduced that the 6 nm crystalline nanoparticle took a longer time to deform and it mainly preserved its initial ordered mixing pattern at high temperatures.

As it is clearly seen in the figures, the morphology of the nanoparticles was strongly dependent on the temperature, size, and shape. Also, the deformation mechanism of the crystalline nanoparticles was mainly in a good agreement with the RDFs and core-to-surface concentration profiles. For example, as the temperature increased, all the

particles deformed, but 6 nm crystalline nanoparticle mostly preserved its spherical shape even at high temperatures. However, the maximum change in the visualized crystalline nanoparticles was observed in the cubic nanoparticles. As the temperature increased from 300 K to 1700 K, the initial cage structure was completely disappeared and a spherical particle was obtained.

#### 2.4.2.3 Voronoi Analysis

Voronoi analysis results for the nanoparticles with 2 nm, 4 nm, 6 nm diameter and cubic structure are shown in Figure 2.22. In the Figures, top ten common Voronoi polyhedra are listed for each nanoparticle. Due to having stable crystalline structure, the polyhedra found in the liquid phase and solid phase were completely different from each other.

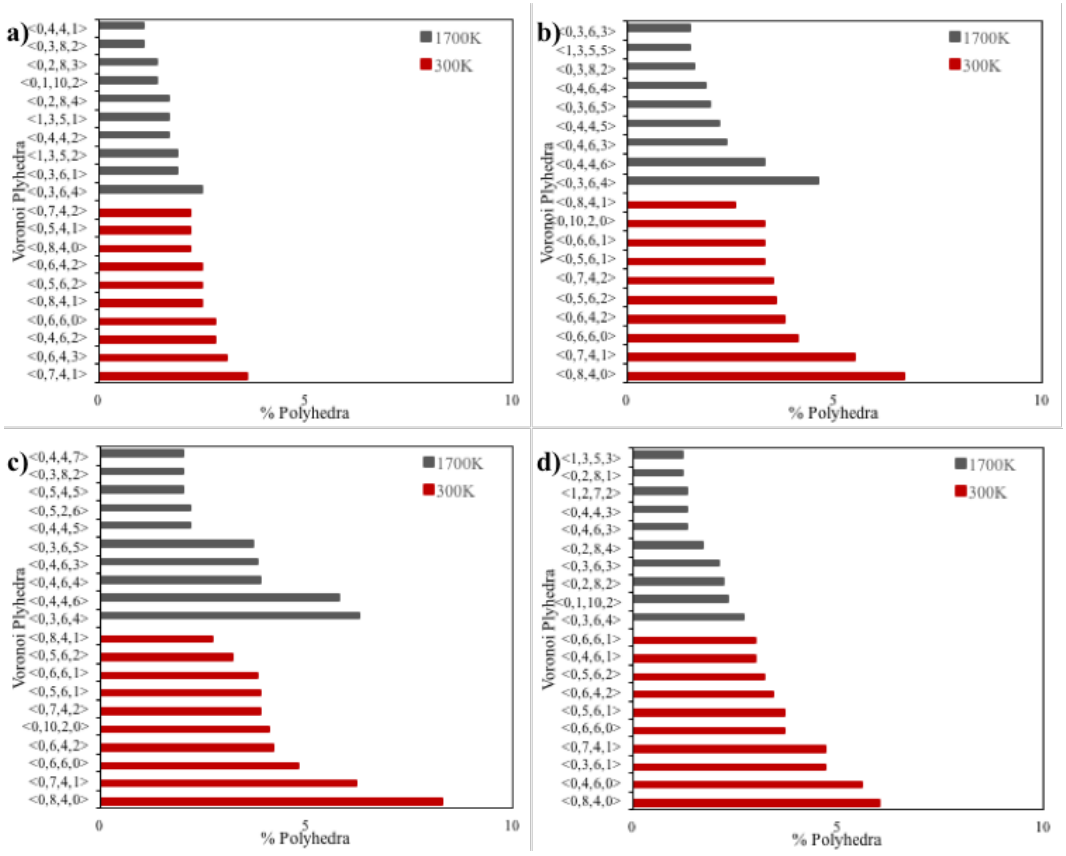


Figure 2.22: Voronoi analysis of crystalline $FeNi_3$ nanoparticles with a) 2 nm diameter b) 4 nm diameter c) 6 nm diameter d) cubic structure

Wigner-Seitz cell (a special case of the Voronoi cells and deals with lattice vectors) of the FCC lattice is rhombic dodecahedron (<0,12,0,0>) which has high rectangularity [70]. On the other hand, at the nanoscale, the most stable polyhedral structures are cuboctahedron and truncated octahedron for FCC lattice [69].

According to the Voronoi tessellations of the crystalline nanoparticles, nanoparticles with 4 nm and 6 nm diameter had almost the same topological structure when they are in solid phase at 300 K. Although some polyhedrons on the 2 nm and cubic nanoparticles differed from the nanoparticles with 4 nm and 6 nm diameter, <0,6,4,2>, <0,8,4,0>, <0,7,4,1>, and <0,5,6,2> were the main polyhedrons at solid phase of the cubic and spherical nanoparticles with crystalline structure. These polyhedrons consisted of pentagonal, hexagonal and rectangular faces which corresponded to the truncated octahedron and tetradecahedron- a regular form of the truncated octahedron [71]. Moreover, as the particle size increased to 4nm and 6nm, the deformed rhombic dodecahedron structures (<0,10,2,0>) with more than 80% rectangular faces started to be observed in a small amount.

#### 2.4.2.4 Surface Energy and Melting Point

Surface energy change of the crystalline nanoparticles with respect to temperature is illustrated in Figure 2.23.

In Figure 2.23, it is seen that at room temperature, the cubic and spherical nanoparticles had similar surface energies. Among the spherical ones, the 6 nm crystalline nanoparticle had the lowest surface energy value due to having low surface to volume ratio, 0.924 among the others (2.776 surface to volume ratio for the 2nm nanoparticle and 1.269 for the 4nm nanoparticle). Although the cubic nanoparticle had a higher surface to volume ratio (1.929) than the 6 nm nanoparticle, the surface energy value of the cubic nanoparticle remained at the lowest value because of the low surface area.

In general, surface energy decreases at higher temperatures because of the increasing entropy ($d\gamma/dT=-S_{surface}<0$). During the temperature augmentation process, the surface energies tended to decrease until 1300 K as it was expected. However, the surface energies started to increase while minimizing the surface entropy. This is

probably because the surface atomic arrangement was different from the inner part and a denser structure was occurred in liquid phase compared to the solid phase.

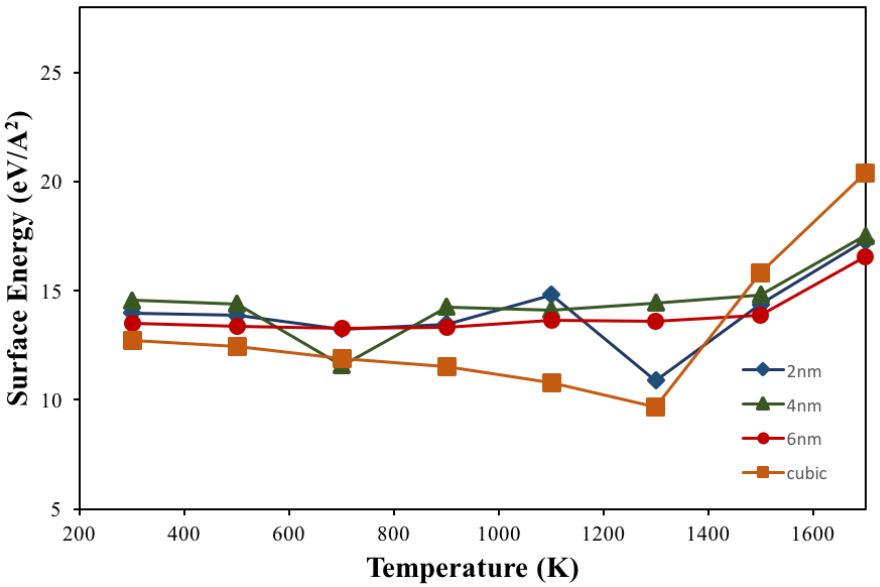


Figure 2.23: The surface energy change with respect to temperature for different size of the crystalline $FeNi_3$ nanoparticles

Like surface energies, the melting point is also directly related to the surface-to-volume ratio and an increase in the surface to volume ratio leads to decrease in the melting temperature of the particles because of the high percentage of the less coordinated and less bounded surface atoms [72]. This has been proven from the molecular dynamics simulations for the spherical nanoparticles with different diameters. Corresponding to the surface to volume ratio, the 2 nm, 4 nm and 6 nm nanoparticles melted at 1381.70 K, 1600.81 K and 1715.81 K, respectively. On the other hand, the crystalline nanoparticle with cubic structure behaved differently. Although the cubic nanoparticle had the large surface to volume ratio, it started to melt at 1645.48 K which was very close value to the melting point of the 4 nm nanoparticle, probably because of having the similar surface area. This result showed the strong size and shape dependence of the melting behavior of the nanoparticles.

### 2.4.3 Structural Properties of the $FeNi_3$ Nanoamorphous Systems

#### 2.4.3.1 Radial Distribution Functions

The nanoparticle with the diameter equal to 2 nm consists of 368 atoms in total, with 112 iron atoms and 256 nickel atoms. To determine the temperature effect on the structural evolution of the nanoparticles, the systems were cooled from 1900 K to 300 K by 200 K interval. The radial distribution function graphs of the cooled amorphous nanoparticle with 2 nm diameter from 1700 K to 300 K are illustrated in Figure 2.24.

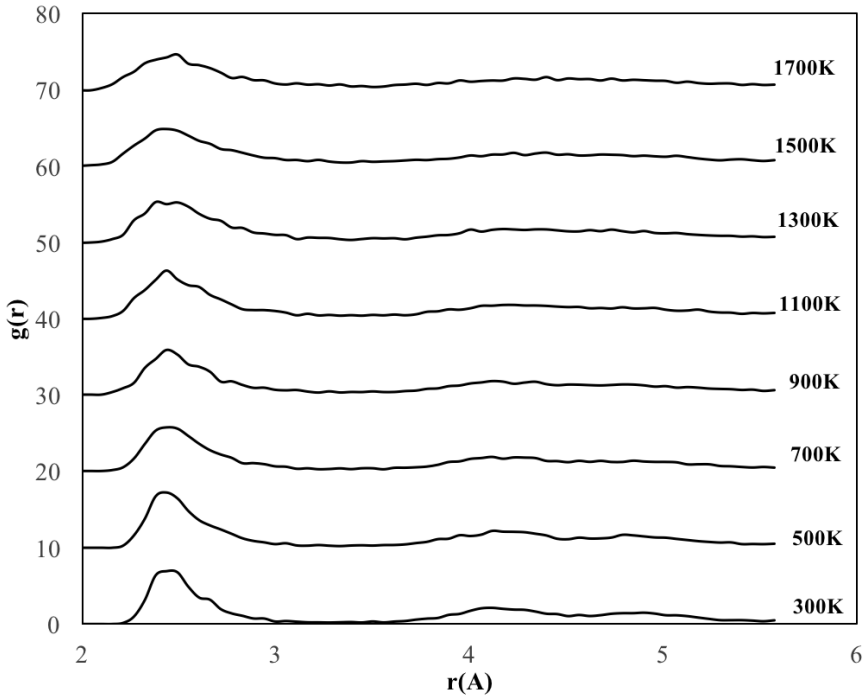


Figure 2.24: RDF graphs of the 2 nm $FeNi_3$ amorphous nanoparticle for different temperatures

According to Figure 2.24, we clearly observed that, at high temperatures, there was an absence of order between atoms, but the first peaks were always clear at high temperatures. As the temperature decreased, the first peak steepened and the structure between the first neighbors approached to the crystalline phase, even though the

amorphous and disordered phase remained between the second and third neighbors of the atoms.

The nanoparticle having the diameter equal to 4 nm consists of 2913 atoms in total, with 761 iron atoms and 2152 nickel atoms. In Figure 2.25, even though the first peaks were always observed during the cooling process, the disordered structure was mainly preserved until 900 K. After that point, the second and third peaks appeared, and at 300 K, mainly, a crystal structure was obtained.

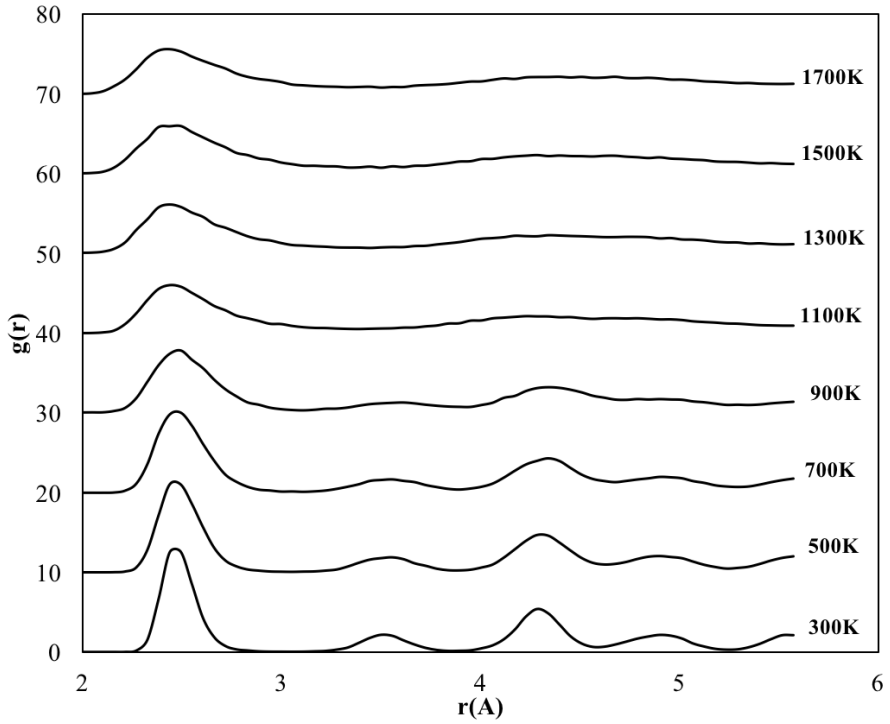


Figure 2.25: RDF graphs of the 4 nm $FeNi_3$ amorphous nanoparticle for different temperatures

Compared to Figure 2.14, at 300 K, all the peaks in Figure 2.25 have a broadened shape but the first, second and third peaks located at the same positions. This means the inner side of the amorphous 4 nm nanoparticle (until $3^{rd}$ nearest neighbor distance) mostly transformed to the crystal structure at room temperature although the remaining part preserved its disordered amorphous structure. Throughout the amorphous to the crystalline transition process, lattice parameter decreased from 3.612 Å at 900 K and reached to 3.5 Å at 300 K that is the same value with the lattice

parameter of the initially crystalline nanoparticle with 4 nm diameter.

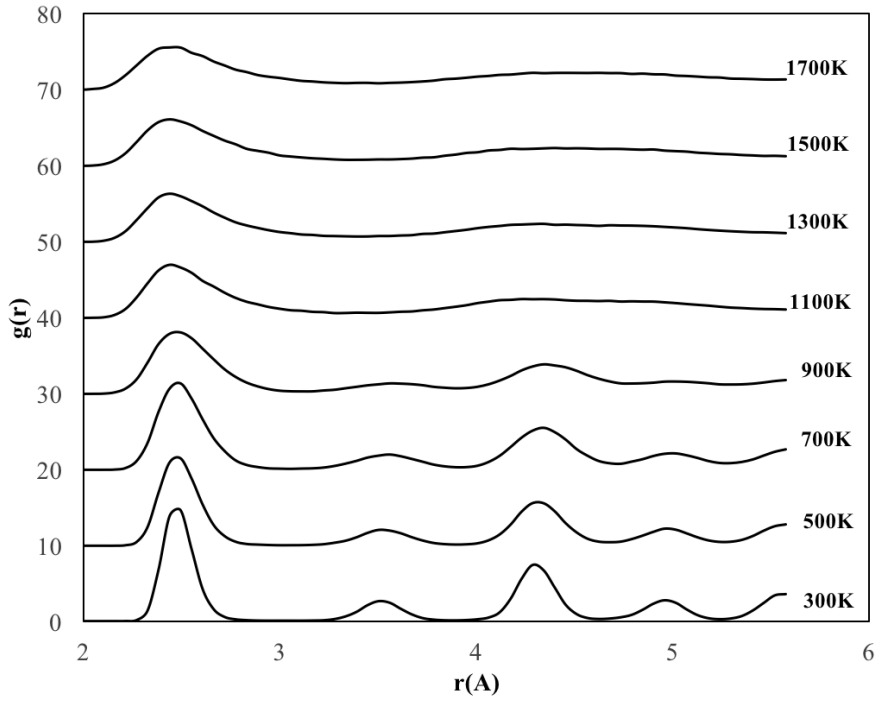


Figure 2.26: RDF graphs of the 6 nm $FeNi_3$ amorphous nanoparticle for different temperatures

The amorphous nanoparticle with 6 nm diameter includes 2450 Fe atoms and 7334 Ni atoms (9784 atoms in total). Like 4 nm amorphous nanoparticle, the peaks started to appear and the valley between the peaks became deeper at 900 K, but the amorphous-to-crystalline transformation occurred in a faster and sharper way. At 300 K, the first and the second peak of the overall radial distribution of the initially amorphous 6 nm nanoparticle had almost the same height and width with the RDF of 6 nm crystalline nanoparticle (Figure 2.15). Although the other peaks were located in the same position, they had a broader shape compared to the peaks in the RDF of the initially crystalline nanoparticle with 6 nm. This means that the 6 nm nanoparticle, which owned amorphous phase at the beginning, completely transformed to the crystalline phase, even though the final structure has not been as compact as the structure of the initially crystalline nanoparticle with the 6 nm diameter at room temperature. Moreover, during the cooling process, the lattice parameter of the 6 nm particle changed

from the 3.556 Å at 900 K, where crystallization started, to 3.5 Å at room temperature which is consistent with the lattice parameter of the initially crystalline nanoparticle explained in the previous section and the value stated in the literature [73].

Overall, we observed clearly that, at high temperatures, there was an absence of an order for all initially amorphous nanoparticles. From the RDF graphs of the 2 nm nanoparticles, it has been seen that amorphous structure was preserved during the cooling process even at 300 K. On the other hand, in the RDF figures of the nanoparticles with 4 nm and 6 nm diameter, there was a transition from amorphous phase to the crystal structure at lower temperatures, and 300 K, the complete crystalline structure was obtained in 6 nm nanoparticle with 3.5 Å lattice constant. Although at 300 K, the lattice parameter of both 6 nm and 4 nm nanoparticles reached to 3.5 Å value, the variation in lattice constant of the nanoparticle with 4 nm diameter was higher than 6 nm diameter because of the size effect on the lattice parameter [74].

Moreover, the coordination number change of the 2 nm, 4 nm and 6 nm amorphous nanoparticles with respect to temperature is illustrated in Figure 2.27.

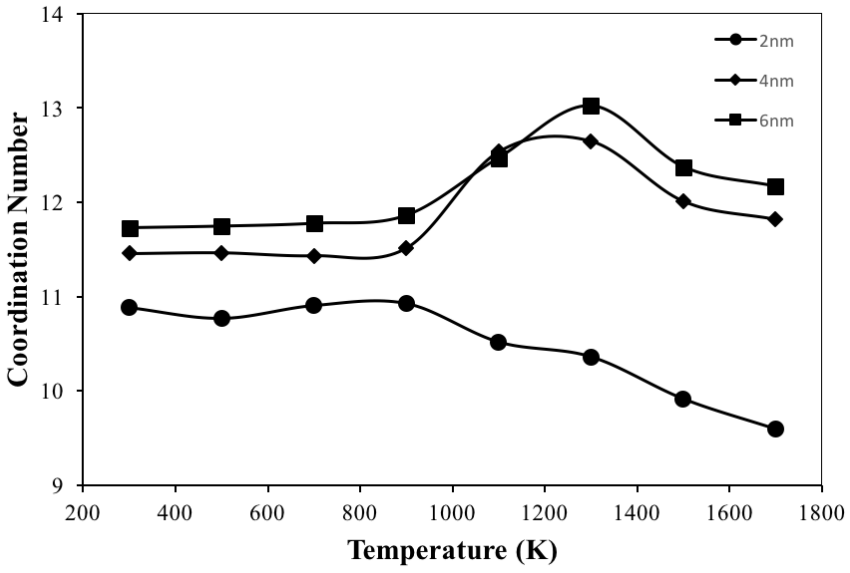


Figure 2.27: Coordination number change of the amorphous $FeNi_3$ nanoparticle with with respect to temperature

According to Figure 2.27, the coordination number of the amorphous 2 nm particle continuously increased as the temperature approached 300 K, even though it preserved its amorphous structure during the cooling process. On the other hand, the coordination number of the amorphous nanoparticle with 4 nm diameter reached its maximum value at 1300 K probably because of the sublimation. Then, it stayed at balance around 11 that is very close value with the completely crystalline 4 nm nanoparticle (10.9).

The 6 nm amorphous nanoparticle exhibited a similar trend with the 4 nm nanoparticle, but the coordination number of the 6 nm amorphous nanoparticle reached to 11.2 which is the same coordination value of the initially crystalline 6 nm nanoparticle. This means the initially amorphous nanoparticle with 6 nm diameter completed its crystalline transformation by obtaining same CN value with the initially crystalline nanoparticle.

#### 2.4.3.2 Spatial Ordering and Morphology

Core-to-surface concentration profiles are essential to observe the atomic movement during heat treatment. The change in the number of Fe and Ni atoms throughout the particles having 2 nm, 4 nm and 6 nm diameter are shown in the following figures.

In Figure 2.28, it is seen that the random mixed atomic patterns of the 2 nm amorphous nanoparticle were preserved as the temperature decreased. However, Fe atoms diffused from the core to surface, and the initial Fe atomic positions at the core side started to be filled with Ni atoms at lower temperatures. In the end, the main atomic distribution peak of the Fe atoms located at the surface, but Ni atoms spread throughout the particle.

From the morphological point of view, it is known that amorphous nanomaterials have unstable structures compared to their crystalline counterparts, so during MD simulations, the shape and surface area of the particles changed to have more stable structures. For example, as the temperature decreased, the irregular shape of the amorphous 2 nm nanoparticle converted to the spherical shape.

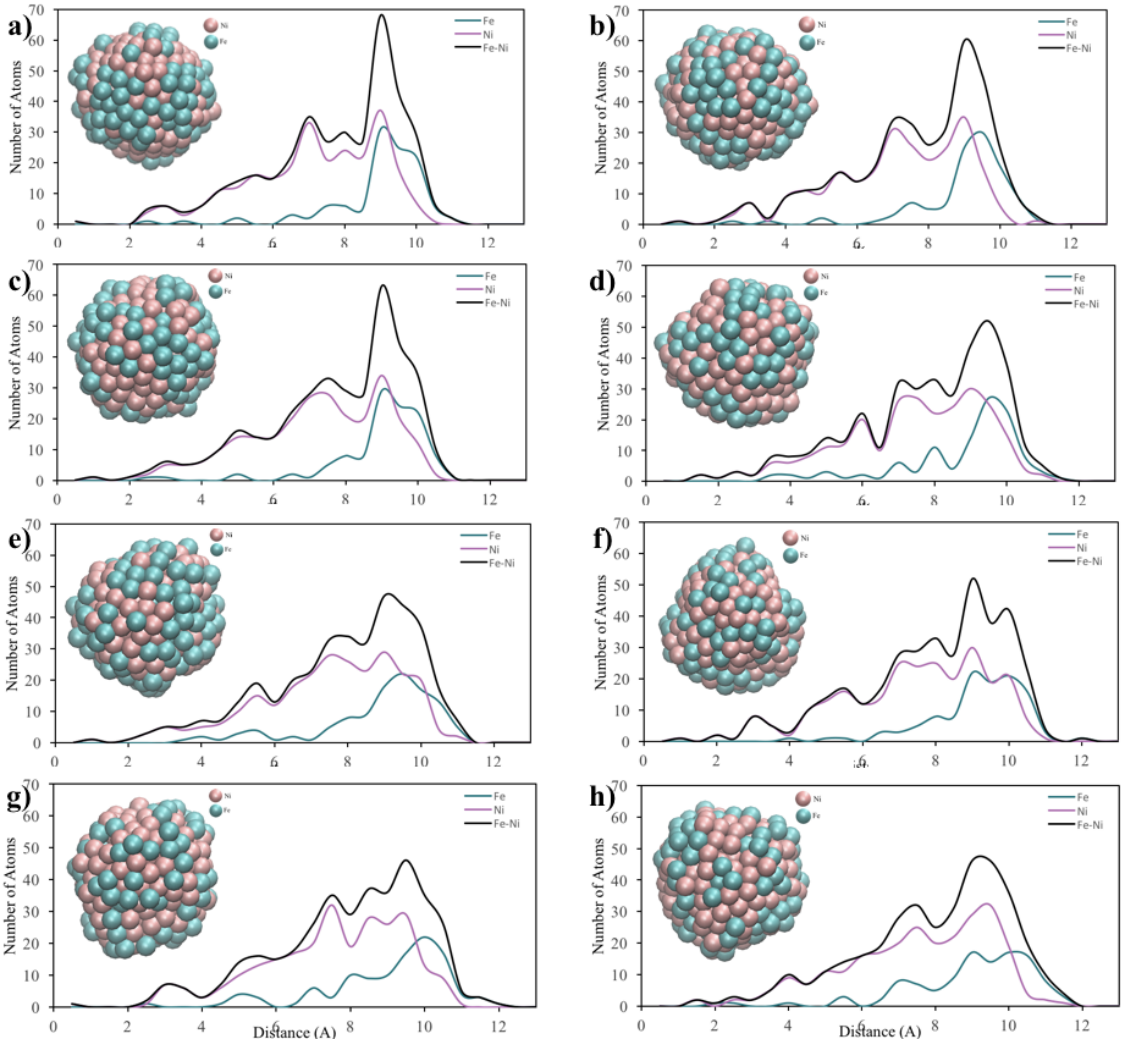


Figure 2.28: Core-to-surface concentration profiles of Fe and Ni atoms in the 2 nm amorphous nanoparticles at a) 300 K b) 500 K c) 700 K d) 900 K e) 1100 K f) 1300 K g) 1500 K h) 1700 K

According to Figure 2.29, the melted Fe atoms at the surface stayed during the cooling process and Ni atoms diffused towards the inside of the 4 nm amorphous particle. Although Ni atoms dominated the core and most of the Fe atoms were located at the surface, the random mixed pattern in the intermediate shell preserved at 300 K.

For the 4 nm nanoparticle, it has been observed that the irregular shape of the particles transformed the spherical shape at the onset of the melting; afterward, they reached to a more stable sharp-sphere.

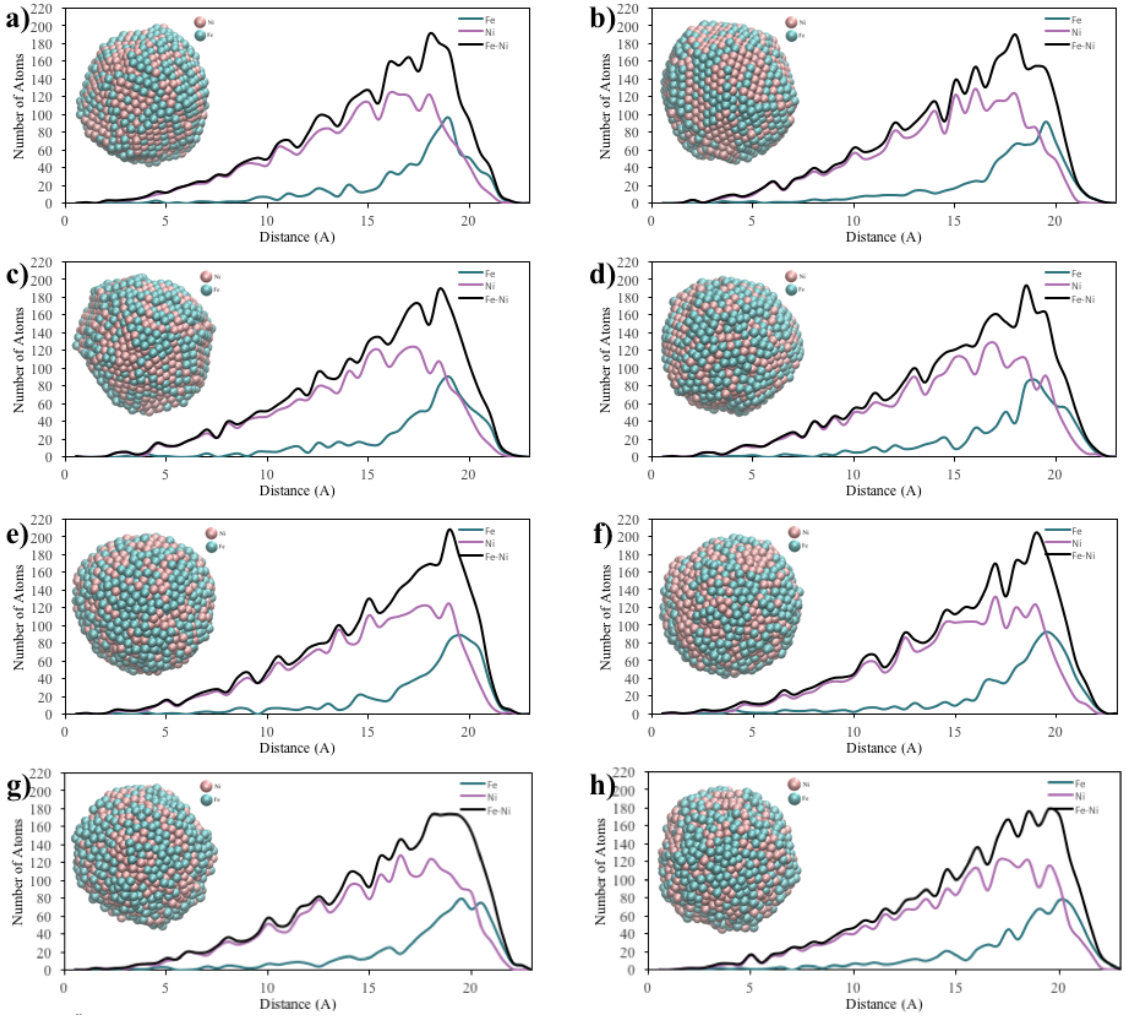


Figure 2.29: Core-to-surface concentration profiles of Fe and Ni atoms in the 4 nm amorphous nanoparticles at a) 300 K b) 500 K c) 700 K d) 900 K e) 1100 K f) 1300 K g) 1500 K h) 1700 K

In Figure 2.30, mainly mixed pattern of Fe and Ni atoms obtained at the end of the cooling process, but Ni atoms still dominated the core and melted Fe atoms stayed at the surface, similar to the 4 nm nanoparticle. Moreover, 6 nm nanoparticle also showed a similar trend with the 4 nm nanoparticle in terms of morphological transformation during the cooling process. With the decreasing temperature, the irregular shape of the 6 nm nanoparticles evaluated smoothly to the spherical shape while melting, and a shape of sharp-sphere was obtained at 300 K which means the 4 nm and 6 nm nanoparticles had a capability of undergoing a transformation from their initial

shapes to geometrically more stable shape.

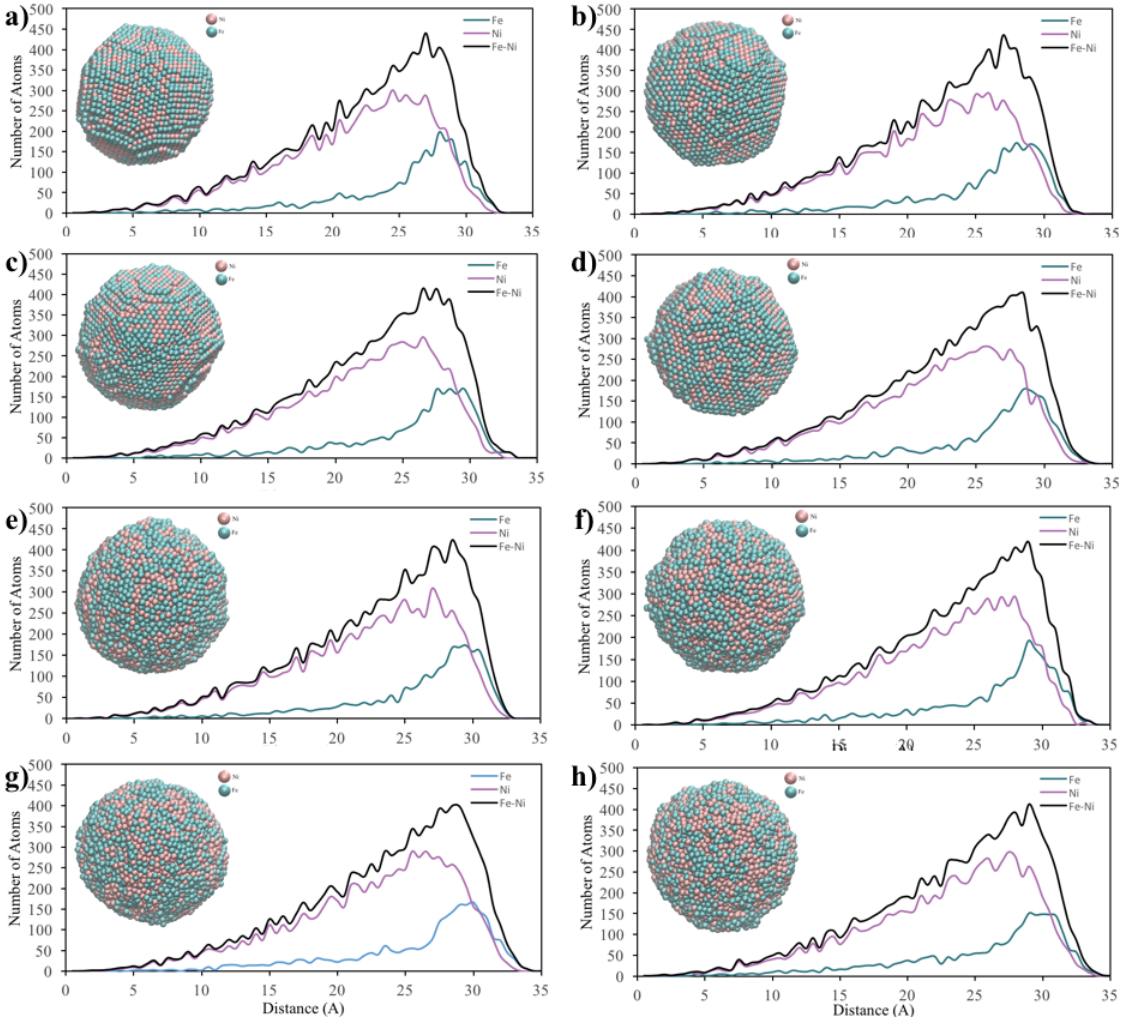


Figure 2.30: Core-to-surface concentration profiles of Fe and Ni atoms in the 6 nm amorphous nanoparticles at a) 300 K b) 500 K c) 700 K d) 900 K e) 1100 K f) 1300 K g) 1500 K h) 1700 K

As it has been explained in the Introduction Section, the difference between atomic sizes of the constituents leads to core-shell structure, in which small atoms are located in the core-side but the bigger ones form an outer shell that surrounds the core. Also, a large difference in the cohesive energy of the atoms causes segregation. In this system, Fe and Ni atoms have a similar radius and cohesive energy, such as Fe atoms have the 0.126 nm radius with 4.28 eV/atom cohesive energy and Nickel atoms own 0.125 nm radius with 4.44 eV/atom cohesive energy [75]. Therefore, the nanopar-

ticles having equal to/larger than 4 nm diameter formed an ordered mixing pattern, rather than segregated or core-shell structure, as it has been expected. Although at room temperature, some Ni atoms stayed at the core side of the smaller particles, as the diameter of the particle size increased to 6 nm, the atomic pattern mainly transformed to the ordered mixing pattern and no segregation was observed.

#### 2.4.3.3 Voronoi Analysis

The Voronoi tessellations of the amorphous nanoparticleswith 2 nm, 4 nm and 6 nm diameter at 1700 K and 300 K are shown in Figure 2.31.

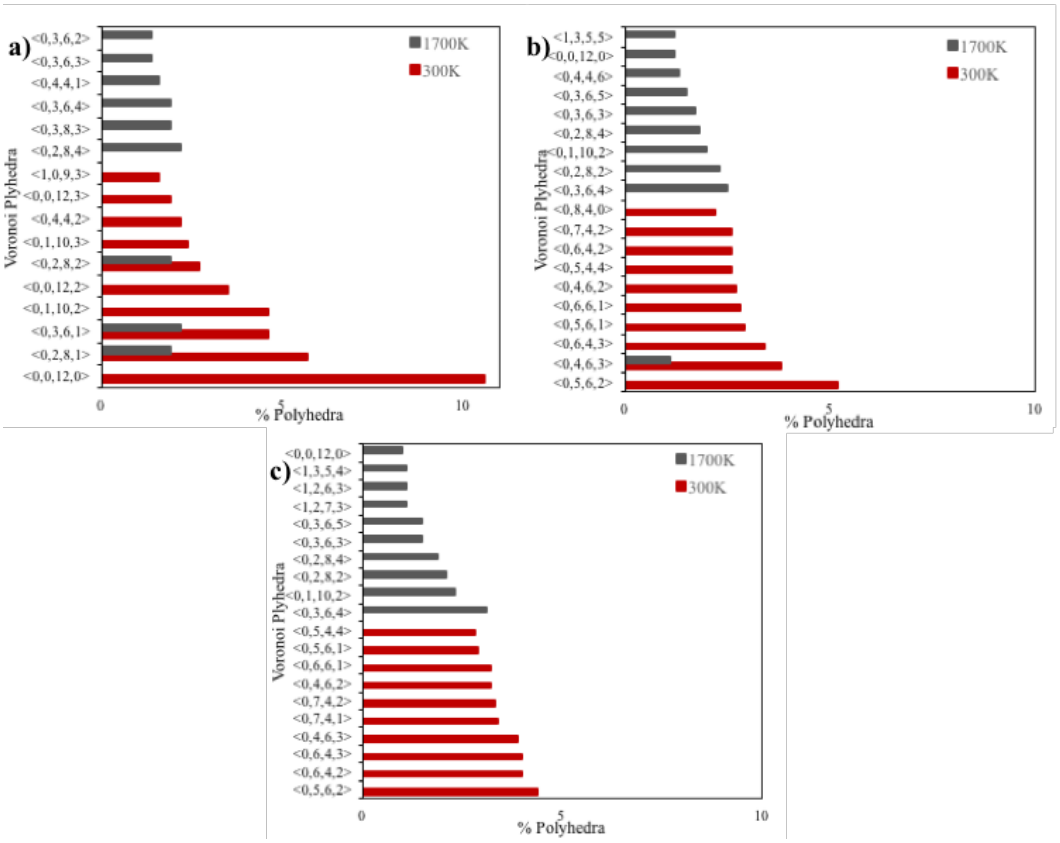


Figure 2.31: Voronoi analysis of amorphous $FeNi_3$ nanoparticle with a) 2 nm diameter b) 4 nm diameter c) 6 nm diameter

According to Figure 2.31a, none of the polyhedrons in 2 nm amorphous nanoparticle was found in the 2 nm crystalline nanoparticle. This means that amorphous nanoparti-

cle with 2 nm diameter conserved its amorphous structure during the cooling process from 1700 K to 300 K. The vast majority of the Voronoi tessellation of the 2 nm amorphous nanoparticle belonged to <0,0,12,0> polyhedron which showed that the fully icosahedral structure and its deformed forms (<0,1,10,2>, <0,2,8,2>) covered the 2 nm nanoparticle. The other <0,2,8,1> and <0,3,6,1> polyhedral structures correspond to deformed trigonal prism were also observed in both liquid and solid phase of the 2 nm amorphous nanoparticle.

Due to the fivefold symmetry below the critical sizes, the icosahedral polyhedrons are the stable form of the metallic nanoparticles [76]. However, from the previous studies, it has been shown that the stability of the icosahedral structure decreased when the total number of atoms increased in a nanoparticle [69]. In accordance with the literature, the icosahedral structure <0,0,12,0> disappeared and the trigonal faces decreased to lower than 50% as the size of the particles increased to 4 nm and 6 nm.

According to Figure 2.31b and Figure 2.22b, the main polyhedrons like <0,5,6,2>, <0,6,4,2>, and <0,5,6,1> were found in the both initially crystalline and initially amorphous solid nanoparticles having 4 nm diameter. On the other hand, <0,4,6,3> polyhedron structure was observed in both the liquid and the solid phase of the 4 nm amorphous nanoparticle. This means that although 4 nm amorphous and crystalline nanoparticles had some common local atomic arrangement in the solid and liquid phases, the 4 nm nanoparticle with amorphous phase could not completely transformed to the crystalline structure at 300 K.

In Fe-centered Voronoi polyhedra of the 6nm nanoparticles (Figure 2.31c), it has been observed that all of the local atomic configurations in solid phase were completely different from the liquid phase. Furthermore, most of the polyhedrons in the solid phase were common with the polyhedral shapes of the initially crystalline nanoparticle owing 6 nm diameter in solid phase, such as <0,6,4,2>,<0,5,6,2>, <0,7,4,1>, <0,7,4,2> and <0,5,6,1>. These polyhedrons correspond to the deformed truncated octahedron with its derivatives (tetradecohedron) having $m\bar{3}m$ symmetry. The truncated octahedron is one of the most stable FCC structure because of having the minimum energy for larger nanoparticles [69]. According to the common Voronoi polyhedrons in the 6nm nanoparticle, it has been seen that the number of rectangular faces of the local

polyhedra around Fe atom significantly increased to more than 50% which matched with the distorted FCC lattice structure. Therefore, we can say that the 6 nm amorphous nanoparticle generally transformed to the FCC crystalline lattice structure at 300 K.

Moreover, most of the polyhedron structures in the initially amorphous nanoparticle with 4 nm and 6 nm diameter were common at room temperature, but only a few of them are found in the 2 nm amorphous nanoparticle. This is because 2 nm nanoparticle preserved its amorphous structure throughout the cooling process but the others transformed to the crystalline structure partially or completely.

Considering coordination number from the Voronoi analysis, CN of 2 nm amorphous nanoparticle mainly remained higher than 12 which is another proof for the disordered amorphous structure because the amorphous structures may have a more efficient atomic packing [3]. Also, the total coordination numbers of the 6 nm and 4 nm nanoparticles were between 12 and 13 atoms which is consistent with the coordination number of the FCC lattice structure. Therefore, we can conclude that the initial crystalline or amorphous structure did not affect significantly the final FCC structure of the 6 nm nanoparticle at 300 K.

#### 2.4.3.4 Surface Energy

The surface energy change with respect to temperature for different size of the amorphous $FeNi_3$ nanoalloys is illustrated in Figure 2.32.

The surface energy change of the 4 nm and 6 nm nanoparticles exhibited the similar trend, and the surface energy significantly decreased at lower temperatures because of the transformation from amorphous to the stable crystalline structure. However, this trend was not observed in the surface energy change graph of the 2 nm amorphous nanoparticle due to the lack of the amorphous-crystalline transition.

In general, the surface energy of the nanoparticle increases with decreasing particle size due to the high amount of unbounded surface atoms. However, in Figure 2.32 an opposite trend was seen and the largest nanoparticle with 6 nm diameter had the highest surface energy although the 2 nm nanoparticle had the lowest value. As

it has been stated earlier, the nanoparticles have a high percentage of surface area compared to their bulk counterparts, so sometimes the surface atoms owing lower coordination numbers rearrange themselves [77]. Also, due to the fivefold symmetry which are stabilized at small sizes, metallic nanoparticles, below critical size, formed new icosahedral structure by minimization of the surface energy and optimization of the surface morphology because (111) facets in the icosahedral structure is denser and the surface energy is lower than the (100) facets found in the truncated octahedron. Therefore, in the 2nm nanoparticles, the surface atoms formed more compact configuration with new icosahedral structure by minimization of the surface energy and optimization of the surface morphology [76].

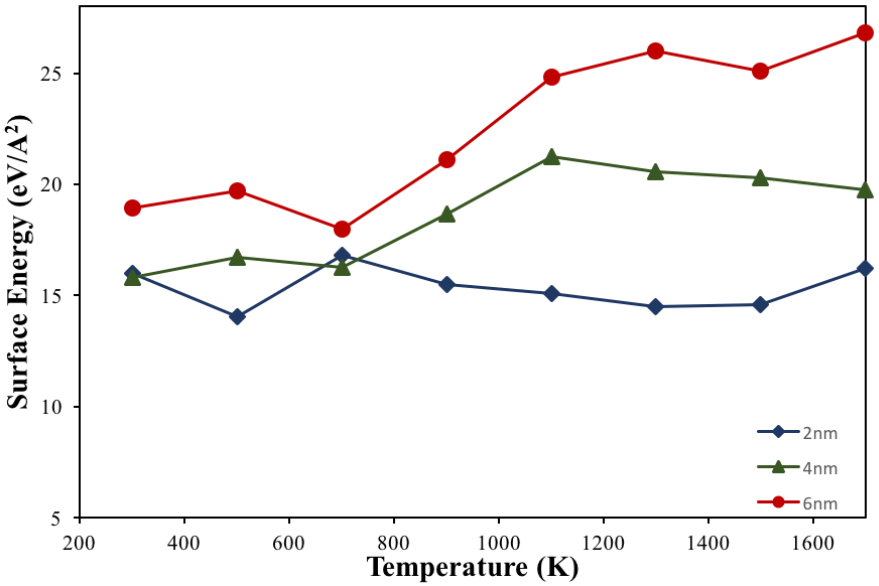


Figure 2.32: The surface energy change with respect to temperature for different size of the amorphous $FeNi_3$ nanoparticles

# CHAPTER 3

# SYNTHESIS AND STRUCTURAL CHARACTERIZATION OF IRON AND NICKEL BASED NANOALLOYS

## 3.1 Background

### 3.1.1 Production Methods of Nanoalloys

There are several chemical and physical methods to synthesize nanoalloys. They are generally classified into two categories which are bottom-up and top-down methods [78].

In the bottom-up technique, nanosized particles are produced by building ions or molecules layer by layer or atom by atom in a gas or in a liquid or in a matrix or on a substrate. Most of the chemical synthesis and self-assembly methods and surface deposition techniques belong to the bottom-up production approach. In this approach, narrow particle size distribution can be obtained with the low amount of impurity and the desired final nanoalloy properties can be controlled. On the other hand, the bottom-up technique has low yield, and because of the reactivity of the small particles, they can quickly agglomerate [14].

In contrast to bottom-up methods, in the top-down approach, the size of a bulk material is reduced to nano-dimensions from micron size or higher. Lithography, mechanical milling and mechanical alloying are considered as top-down production methods. The main disadvantage of the top-down technique is that obtaining nanostructure in narrow size particle distribution is hard by breaking down the large particles. However, it is a fast and easy production method comparing with most of the other techniques. Also, with top-down approaches, it is possible to produce stable and

metastable intermetallic phases in high volume, so it is convenient for the large-scale industrial applications.

### 3.1.2 Mechanical Alloying Methods

In the mechanical alloying method, which is also known as a non-equilibrium processing technique, micron size powders are placed into a mill with balls and the powders are repeatedly deformed, fractured and alloyed by high energy collision under the impact of balls until the desired composition and particle size are obtained [14, 12].

With mechanical alloying, according to the compositions of the powders or the experimental conditions, several ordered and disordered intermetallic phases can be produced [12]. The capability of synthesizing disordered alloys gives an advantage because it is known that the partially ordered phases are stronger than those disordered or fully ordered ones. In mechanical alloying, as the milling time increases, an ordered intermetallic can transform into the disordered solid solution or amorphous phase [21]. Although this transformation depends on several parameters, such as relative free energies of amorphous and crystalline phases, temperature, defect density, and impurity contamination; the mechanism and formation limits could not be strictly defined [79, 21].

Even though the particles are produced over a wide range of sizes, the interest for mechanical alloying has been grown, and several studies have been conducted since the mid-1980s because it is applicable to almost any system for high volume production in low cost and extremely small alloyed particles can be obtained. Also, it has the ability to synthesize equilibrium and non-equilibrium intermetallic phases and different microstructures at room temperature [73, 10].

Thus, it is essential to produce novel nanoalloys by this technique because mechanical alloying is a solid-state processing technique and the limitations of the phase diagram do not affect the end product obtained by mechanical alloying [12]. Also, mechanical alloying is applicable for the pure powders with wide range particle sizes (1-200 micron). The size of the powders is not very critical as long as it is smaller than the size of the milling balls [80].

The nature of the process and the characteristics of the produced nanoparticles (i.e., size distribution, composition) by mechanical alloying in ball mills depends on various parameters which are interrelated with each other [80, 10];

- Type of the mills
- Type of the balls
- Milling temperature
- The weight ratio between the powders and balls
- Mechanical behavior and phase transformations of the powders
- Milling atmosphere
- Milling media
- Milling time
- Milling speed

**Types of Mills for Mechanical Alloying**

Different mill types can be used to produce mechanically alloyed nanoparticles. Some of them are Spex Shaker Mill, Planetary Ball Mills, Attrition Ball Mill and Special Design Mills for specialized purposes [10, 12]. The schematic views of a shaker mill, a planetary ball mill, an attrition ball mill are shown in Figure3.1.

In SPEX shaker mills, the mechanical alloying of the powders is obtained by the several back-and-forths shaking motions with lateral movements of vials [12].

Planetary ball mill, which is also known as Pulverisette, is one of the most common types of the ball milling for mechanically alloying. In mechanical alloying with a planetary ball mill, a few hundred grams of the powder of the constituents are placed into small bottles, and these bottles move like a planet movement. The vials are designed to rotate both on a disk and their own axes. Thus, while the rotating disk acts as a force on the vial contents in one direction, a centrifugal force is acting in the opposite direction due to the rotation of their own axis [12]. The horizontal view

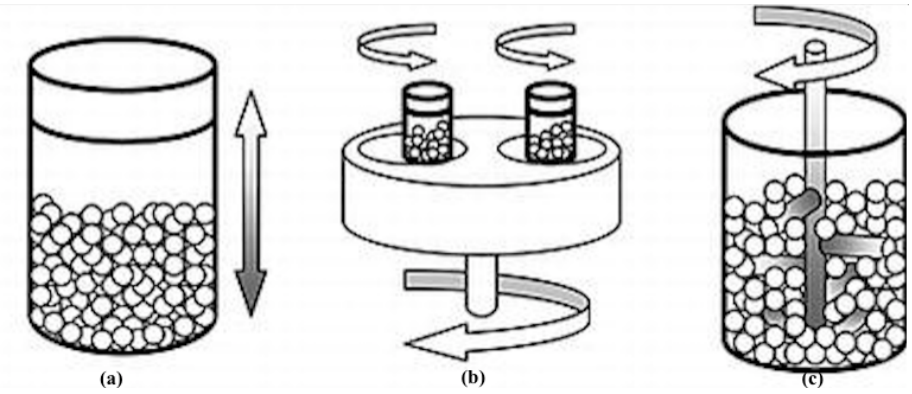


Figure 3.1: Schematic view of mills for mechanical alloying (a) Shaker mill (b) Planetary ball mill (c) Attrition ball mill [9]

of ball milling in a planetary ball mill and the collusion between the balls and the powders are shown schematically in Figure 3.2.

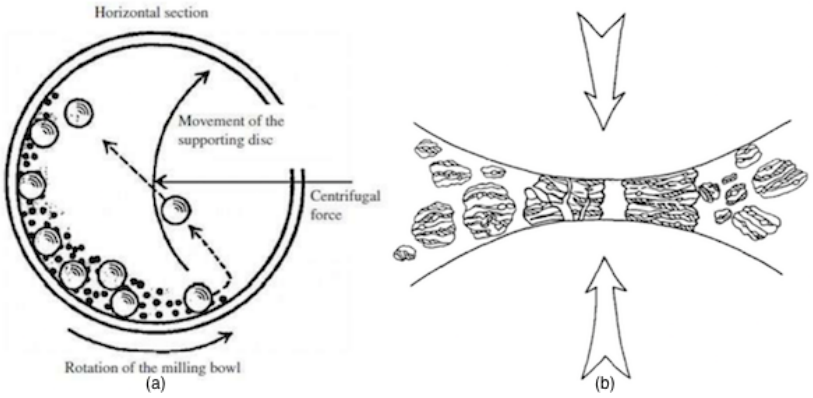


Figure 3.2: Schematioc drawing of collusion between the balls and the powders[10, 11]

Although attrition ball mills have a large capacity of powders, the velocity, and the efficiency are lower than the planetary and shaker mills. In attritors, the powders of constituents are placed into a stationary tank with a grinding media; then, they are mixed with rotating arms to act a force on the powders.

**Type of balls**

Generally, hardened steel, tool steel, hardened chromium steel, tempered steel, stain-

less steel, and bearing steel are used as milling balls for mechanical alloying. The density of the balls is important for the yield of the milling and the characteristics of the synthesized product [80].

The product is produced faster if the mills have higher energy which depends on the mass and the velocity of the balls. Thus, nanosized alloys can be produced in lower milling time by using heavier milling balls, like steel balls, because they provide higher energy than the light balls (i.e., ceramic balls) [10].

**Milling temperature**

The efficiency of mechanical alloying is also dependent on the rate of cold welding which is the function of the milling temperature and the melting point of the material. For instance, if the materials have low melting points (i.e., lead and aluminum), they can be cold welded easily at room temperature with low energy milling. On the other hand, if the materials have high melting points, like iron and nickel, it is needed to apply high energy milling for the welding at reasonable rates [81].

**The weight ratio between the powders and balls**

The weight ratio between the balls and the powders, which is sometimes known as charge ratio, is a crucial parameter for the mechanical alloying. The ratio varies from 1:1 to 220:1 [82] depending on the type and the capacity of the mill. Generally, the most common ball to powder ratio is 10:1 for a SPEX mill or a planetary ball mill. The influence of the ball to powder ratio on the particle size is shown in Figure 3.3.

**Mechanical behavior and phase transformations of the powders**

The final structure of the particles mainly depends on the mechanical behavior of the constituents. If one of the constituents is brittle but the other is ductile, the brittle particles fracture and they are distributed uniformly in the ductile matrix. If two ductile components are milled, they form lamellar and homogeneous equiaxed particles. On the other hand, if two constituents are brittle, both of them fracture and irregularly shaped particles which are also called "popcorn ball" are produced [10].

**Milling speed**

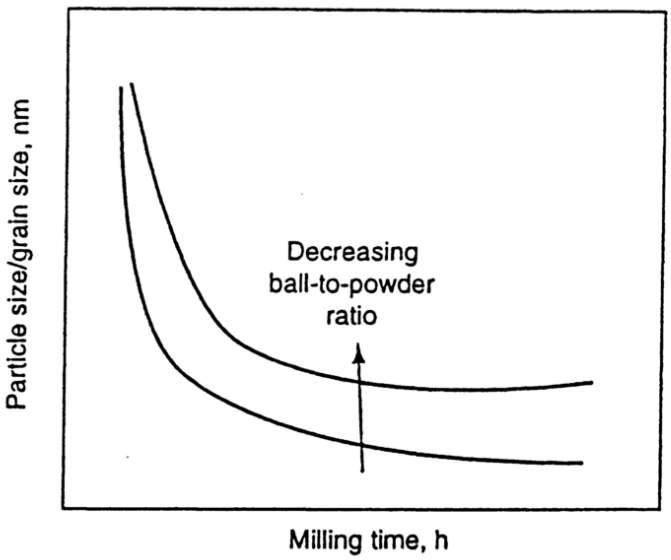


Figure 3.3: The effect of ball to powder weight ratio on particle size refinement [12]

It is known that higher milling speed increases energy and the efficiency of milling. However, it has some limitations according to the type of mills, the raw powders, and the target properties of the end product. For example, if the milling speed is larger than the critical value, the temperature of the vial increases to the undesired values at which agglomeration increases [80].

**Milling atmosphere**

Milling atmosphere is important to avoid contamination and oxidation during the process of mechanical alloying to synthesize nanoparticles. Therefore, the vials are usually evacuated or filled with inert gases, like Argon or Helium. Also, to produce specific compounds in the nanoparticles, like nitrides, hydrides and oxides; nitrogen, hydrogen and air can be inserted [83].

**Milling media**

Sometimes, surfactant-assisted ball milling, in which surfactants are used as a milling media, or wet milling, in which liquid solvent is added to the vial, can be used to reduce contamination and cold welding.

Surfactants produce barrier, reduce the surface energy by forming a thin layer which

prevents the cold welding and agglomeration, and consequently, decreases the size of the alloyed particles in high energy ball milling processes. The type or the physical properties of the surfactants affect the size and shape of the synthesized particles [84].

The appropriate milling media is selected according to the characteristics of the desired final product and the nature of the added powders [80].

**Milling time**

Regardless of the mechanical behavior of the powders, in the beginning, the particles tend to weld; therefore, large particles are obtained together with small particles. At this stage, the alloyed particles have layered structure with different elemental combinations of the constituents [80]. As the collusion between the balls and the powders continues, particles start to get harder, and fatigue failure mechanism starts which lead to generate the alloyed particles in nano-size [12]. Therefore, if the milling time rises, the percentage of the nano-sized alloy particles increases. However, if the milling time increases after the optimum point, nanoparticles begin to agglomerate by cold welding because of the high surface energy which decreases the yield. Agglomeration issue can be solved by using a surfactant-assisted ball milling [10]. However, if surfactants are added to the system at the beginning of the process, they may slow down the mechanical alloying because the solution or the surfactant covers the particle surface [81]. Therefore, it is crucial to determine optimum milling time to avoid re-welding and inhibit agglomeration in mechanical alloying [80].

## 3.2 Previous Studies

There is great research interest on the structural and magnetic properties of the iron and nickel based nanoalloys due to their superior properties.

Several studies considered on the synthesis of the nanostructured Fe-Ni powders by chemical reduction method and characterization of their structural and magnetic behavior[24, 85, 33, 86].

On the other hand, there are various researches on nanostructured Fe-Ni based alloy production and characterization by mechanical alloying. In the studies, different

milling speed or different ball to power weight ratio or different mechanical routes was discussed [19]. In those studies, elemental Fe and Ni powders with high purity were used as raw materials.

In the early 2000's, the different compositions of iron and nickel based alloys were synthesized in a conventional horizontal low energy ball mill at 90 rpm in Argon atmosphere [87]. In this study, to obtain 10 nm grain size, powders were milled for 400 hours. Also, Jartych and his coworkers [88], synthesized Fe-Ni nanoalloys by low (90 rpm) and high energy (300 rpm) milling; then they investigated structural and magnetic properties of the produced nanoalloys. According to the results, it was seen that magnetization increased with the reduction of grain size. The mechanical alloying was completed at higher milling times in low energy milling compared to the high energy milling. However, in the end, the final lattice parameter, crystallite size and strain values obtained from both types of milling was very similar for $Fe_{80}Ni_{20}$ and $Fe_{50}Ni_{50}$.

In 2009, Gheisari et al. [89] considered on the effect of the milling speed on the structural and magnetic properties of the Fe-45%Ni nano powders in mechanical alloying. It was seen that the grain size decreased as the milling speed was increased. Also, with the higher milling speed (up to 400 rpm), while coercivity was decreasing, saturation magnetization increased probably because of the structural properties like an increase in lattice parameter or the phase transformation from nanocrystalline to the amorphous phase.

Also, Gheisari et al. [90] studied on the structural and magnetic properties of the nanostructured permalloy by mechanical alloying in a dry argon atmosphere with a high-energy planetary ball mill and 10:1 the ball-to-powder ratio, recently. To prevent the agglomeration stearic acid was added and the system was milled with the rotation speed of 200 rpm for different milling times. Before characterization, the samples were heat treated. At the beginning of the milling, the lamellar structure of the starting elements was observed with the inhomogeneity of chemical composition. According to the results of the study, mechanical milling of 50 Permalloy was completed in 24 hours with the average crystallite size of 15 nm. Also, during milling process, it was seen that saturation magnetization increased while coercivity fluctuated because of

the internal lattice strain, phase transformation, and contamination.

Two-step mechanical alloying for the nanocrystalline FeNi alloys was conducted by Zhou et al [25] in 2005. In that study, FeNi alloyed nanoparticles with different particle size were obtained by mechanical alloying; then, a medium is added into the system to control the particle size and to investigate the particle size effect on the microwave absorption properties of the nanostructured alloys. At the end of the study, it was shown that the performance of microwave permeability of $Fe_{0.85}Ni_{0.15}$ nanoalloys which is directly related with the microwave absorption behavior was enhanced by the two-step mechanically alloying process.

As a permalloy, $Ni_{78.5}Fe_{21.5}$ was also synthesized by ball milling and characterized to observe the structural and magnetic properties [91]. In that milling process, the ball to powder ratio was taken as 20:1 and the milling speed was arranged to 300 rpm. According to the results, at higher milling time, saturation magnetization increases and the coercivity decreases probably because of the formation of alloy in nano size.

## 3.3 Experimental Method

In this study, The Fritsch Planetary Micro Mill Pulverisette 7 premium was used during the experimental studies to synthesize $FeNi_3$ nanoparticles by mechanical alloying. Fritsch Pulveristte 7 Premium Line which is shown in Figure 3.4, consists of 2 working stations and performs high rotational speed up to 1100 rpm.

### 3.3.1 Experimental Method: Milling Pure Iron Powders

70-micron iron powders with higher than 99% purity were milled in the planetary ball mill. For each grinding bowl, 80 stainless steel balls (each 5 mm in diameter and 0.51 grams in weight) were placed. The sample was prepared according to the 1:10 powder to ball weight ratio. The powders were milled at 250 rpm in 15 minutes grinding cycles. The powders waited for 10 minutes between each cycle to cool the system and to prevent overheating. Also, in order to prevent oxidation and agglomeration, inert gas (Ar) was inserted into the system before milling starts. After the grinding

Figure 3.4: The Fritsch Planetary Micro Mill Pulverisette 7, stainless steel bowl and balls

process was completed, the bowls were allowed to cool to room temperature and powders were collected by opening the bowl under laboratory conditions. In total, the powders were milled for 20 hours and in order to characterize the pure iron powders, the samples were taken before milling starts, after 5 hours, 10 hours and 20 hours. This part of the experimental study only aims to be familiarized with the system and to check the milling parameters.

### 3.3.2 Experimental Method: Mechanical Alloying by High Energy Ball Milling

In this part of the experimental study, the influence of mechanical alloying with two different milling speed (250 rpm and 400 rpm) under dry atmosphere and the two-step mechanical alloying with surfactant usage on the structural and magnetic properties of the $FeNi_3$ nano alloyed particles was investigated and the results were compared with the experimental studies in the literature.

Firstly, iron and nickel powders were milled in the planetary ball milling with 250 rpm milling speed to synthesize $FeNi_3$ nanoalloys, which is considered as a stable phase in the Fe-Ni phase diagram [29]. 70-micron iron powders and 50-micron size nickel powders with higher than 99% purity were added to the milling bowls. Like the milling process of pure iron powders, 80 stainless steel balls were placed into

each grinding bowl. The sample was prepared according to the 1:10 powder to ball weight ratio. In order to avoid oxidation during milling, the vials were filled with spectroscopic grade argon gas. The powders were milled at 250 rpm in 15 minutes grinding cycles. In this part of the study, the cooling time was increased from 10 minutes to 15 minutes after each grinding process because it was seen that 10 minutes were not enough to cool down the sample and to prevent agglomeration in the milled pure iron powders. The powders were milled for 80 hours in total and the samples for characterization was taken after the specified period of time, such as 1 hour, 5 hours, 10 hours, 20 hours, 40 hours, 60 hours and 80 hours. The milling parameters were defined according to the previous studies [92, 93]

Secondly, the same procedure was repeated with 400 rpm milling speed to observe the effect of the milling speed on the structural and magnetic properties of the synthesized nanoparticles.

Afterward, two-step mechanical alloying was applied with 400 rpm milling speed. In this part, dry milling was followed by a second step in which surfactants and solvent were added once the mechanical alloying between constituents was completed to control the particle size of the alloyed $FeNi_3$ nanoparticles. At the beginning, 80 stainless steel balls were placed and Fe-Ni powders were added according to the 1:10 powder to ball ratio into each grinding bowl and ball milling was started. When the mechanical alloying was completed, 3.2 mL heptane as a milling medium, and as surfactants, 0.3mL oleic acid and oleylamine were inserted into the system. To prevent the powders from being oxidized, the bowls were filled with inert Ar gas. The powders were milled for a total of 80 hours at 400 rpm in 15-minute grinding cycles. Like mechanical alloying under the dry atmosphere, after certain time intervals, the bowls were left to cool down to room temperature and a certain amount of colloidal solution was taken out using an injection syringe. Afterward, the taken colloidal solution was subjected to centrifuge at 1000 rpm for 5 minutes for the separation of the powders from the liquid. Then, the mud separated from centrifuge was washed with heptane three times and after each time the mud subjected to centrifuge at 10000 rpm for three minutes. Finally, the mud was dried at 80 °C for 4 hours.

### 3.3.3 Characterization of Samples

In order to observe the mechanical alloying with respect to milling time, the ball milling was stopped at certain time intervals and a small amount of powders was taken from the bowls for the characterization of the produced nanoparticles by X-ray diffraction (XRD), scanning electron microscopy (SEM), energy dispersive spectroscopy (EDS), vibrating-sample magnetometer (VSM).

#### 3.3.3.1 X-Ray Diffraction

The phase analysis of the samples was carried out by using monochromatic X-Ray diffraction in order to investigate the crystal structure, to determine crystallite size and to calculate lattice parameter.

For all X-ray diffraction characterization in this study, a Bruker D8 Advance X-ray diffractometer with Cu-K$\alpha$ at a wavelength of 1.540562 Å was used. Diffractograms were obtained in a range of $2\theta$ = 5-100°with Cu-K$\alpha$ radiation for pure iron powders. On the other hand, in order to observe the superstructure peaks of the ordered phase of the $FeNi_3$ nanoalloys, the diffractogram between $2\theta$ = 20-150°was obtained with a scanning speed of 0.5°/min.

It is known that the angular position of the diffraction lines are changed according to the shape and size of the unit cell. Also, the relative intensities of the lines are modified by the arrangement of the atoms within the unit cell [94]. Thus, with the help of the angular position and intensities of the diffraction lines from XRD data, the crystallite size, lattice strain and lattice parameter of the samples were calculated for each milling time.

The crystallite size of the particles is usually different than the particle size of the sample because of the polycrystalline aggregates [95]. The crystallite sizes of the pure iron powders and alloyed iron-nickel powders were estimated by using the Modified Scherrer Method in which Scherrer equation 3.1 was applied to each peak and the average value for the overall system was obtained from the intercept of the $\ln(B_D)$ vs $\ln(1/\cos\theta)$ graph [96].

In the Scherrer formula which is applicable for very small crystals, the peak broadening of the graph was used to derive the size of the crystallites [94]. However, the width of the peak is affected from the instrument and the sample, so before the calculation of the crystallite size, broadening was corrected according to the standard diffraction pattern of the instrument by using equation [95].

$$t = \frac{0.9\lambda}{B_D \cos\theta_B} \tag{3.1}$$

$$B_D^2 = (B_{measured})^2 - (B_{instrumental})^2 \tag{3.2}$$

Here, t is the crystallite size, $B_D$ is the half width of the maximum intensity after broadening correction in radians, $\lambda$ is the wavelength of the Cu-K$\alpha$ radiation and $\theta_B$ is the Bragg angle at which diffraction occurs if the Bragg law ($\lambda = 2d\sin\theta_B$) is satisfied [94].

However, the modified Scherrer Method was used for the only comparison because it does not consider the effect of strain that contributes the peak broadening and angular shifts of the peak positions in the XRD graph [95]. Especially for the mechanically deformed nanoparticles, microstrain has a considerable effect on the peak broadening in XRD graph. The reasons of the microstrain are the non-uniform lattice distortions, atomic mismatches between constituents, dislocations, high grain boundary volume fraction [89]. According to the literature, an accurate trend for the size variation can be obtained by the Williamson–Hall method [97], so Williams-Hall method was also applied by using equation 3.3 to determine the microstrain in addition to crystallite size [95, 94].

$$B_D \cos\theta = \left(\frac{K\lambda}{D}\right) + 4\epsilon \sin\theta \tag{3.3}$$

When the $B_D\cos\theta$ change with respect to $4\sin\theta$ is drawn, the slope and y-intersect of the graph give strain and crystallite size, respectively.

Moreover, the lattice parameter change of the iron-nickel powders was calculated by using the equation 3.4 which is derived from the combination of the Bragg law and plane-spacing equation for the cubic systems. In this equation, d represents the

distance between adjacent planes of (hkl) and a is the lattice constant [94].

$$\frac{1}{d^2} = \frac{h^2 + k^2 + l^2}{a^2} = \frac{4\sin^2\theta}{\lambda^2} \tag{3.4}$$

It is known that $\sin^2\theta$ always contains small systematic errors which decrease in higher angles [94]. Therefore, during lattice parameter calculation, the highest-angle diffraction lines were considered for each sample.

#### 3.3.3.2 Scanning Electron Microscopy

The microstructure and morphology studies were carried out by using a FEI Nova Nano 430 FEG model scanning electron microscope (FEGSEM). The powders were put on the aluminum sample holder using double-sided adhesive conductive carbon tapes. The scanning electron microscope is one of the most versatile instruments for investigating the microstructure of metallic materials.

#### 3.3.3.3 Energy Dispersive Spectroscopy

The elemental percentage of the particles can be simultaneously determined from the EDS analysis which is normally conducted to obtain elemental percentages of the components observed on SEM. Therefore, to determine the chemical compositions of the alloyed particles and to follow the completion of the alloying, the EDS analysis was used.

#### 3.3.3.4 Vibrating-Sample Magnetometer

The magnetic properties of the powders were examined using ADE Magnetics EV9 model vibrating sample magnetometer (VSM) operating at up to 3 Tesla magnetic field.

In a VSM, a sample is placed within suitably placed sensing coils and it is made to undergo sinusoidal motion, i.e., mechanically vibrated. The resulting magnetic flux

changes induce a voltage in the sensing coils that is proportional to the magnetic moment of the sample.

Magnetic properties are measured by the help of the hysteresis curve (B-H curve). To obtain the hysteresis curve, firstly, the magnetic field is increased and magnetic moments start to align with the field until the saturation flux density ($B_s$) is reached. When the magnetic field is removed, magnetization curve does not follow the original path because some magnetization is retained which is called the remanence ($M_r$). When the magnetization is decreased to zero, the curve passes from the coercive field ($-H_c$); after this point, the magnetization starts to increase in opposite direction until the point of the saturation. The schematic view of hysteresis curve is shown in Figure 3.5 [14]. Moreover, relative permeability ($\mu_r = \frac{\mu}{\mu_0}$, where $mu_0$ is the permeability in a vacuum) is the another parameter to define the magnetic properties of the materials which is the measurement of the magnetization degree.

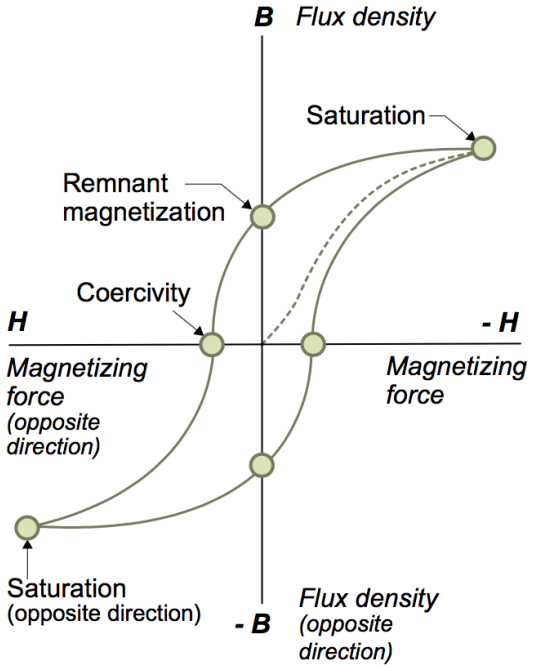


Figure 3.5: Schematic view of a hysteresis curve [13]

## 3.4 Results and Discussion

### 3.4.1 Milling of Pure Iron Powders

The XRD graphs of pure iron powders for different milling times are illustrated in Figure 3.6.

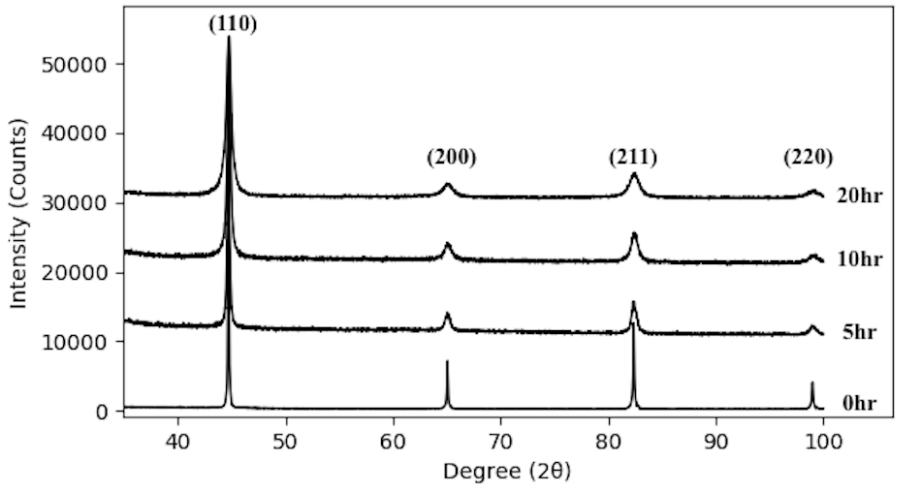


Figure 3.6: The X-ray diffraction curves of pure iron powder for different milling time periods

According to the XRD graph of the pure iron powders for different milling times, the position of the diffraction peaks were consistent with the literature for the body-centered cubic structured iron. From Figure 3.6, it can easily be seen that there was no additional peak of oxides or impurities or there was no shifting; the only change was the increase in the peak broadening with the higher milling time which showed the decrease in crystallite size of the pure iron powders. The decrease in crystallite size that was calculated by the Modified Scherrer method is listed in Table3.1.

In order to investigate the particle morphology and particle size distribution, scanning electron microscopy studies were carried out. The SEM images of pure iron powders with respect to the increased milling time are shown in Figure 3.7.

Table 3.1: Crystallite size change of pure Fe powders with respect to milling time

| Milling Time (hour) | Crystallite Size (nm) |
|---|---|
| 0 | 51.99 |
| 5 | 30.40 |
| 10 | 30.31 |
| 20 | 20.23 |

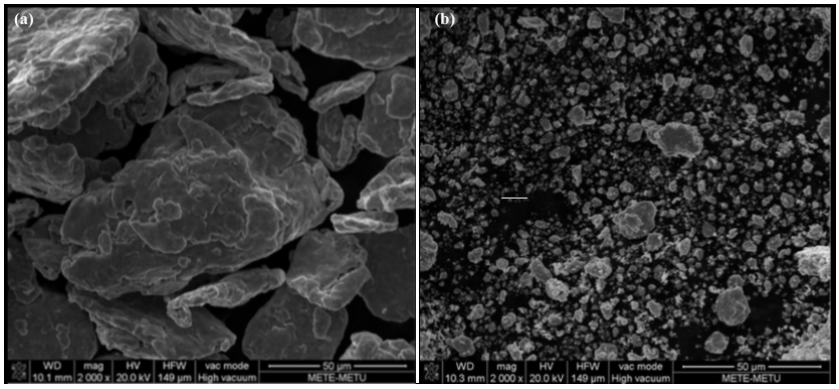


Figure 3.7: SEM images of pure iron powders a) before milling starts b) after 20 hours

According to the calculated crystallite size and the SEM images of pure iron powders, it can be deduced that the particle and crystallite sizes of the powders got smaller with higher milling time.

### 3.4.2 Mechanical alloying of Iron and Nickel Powders

The samples of the iron-nickel powders from mechanical alloying under dry atmosphere with 250 rpm and 400 rpm milling speeds, and from two-step mechanical alloying were analyzed by X-ray diffraction, scanning electron microscopy, energy dispersive spectroscopy, and vibrating-sample magnetometer. The XRD curves of the samples from the mechanical alloying with 250 rpm and 400 rpm under dry atmosphere are given in Figure 3.8 and Figure 3.9, respectively. Also the EDS results

of the samples are listed in Table 3.2 and Table 3.3.

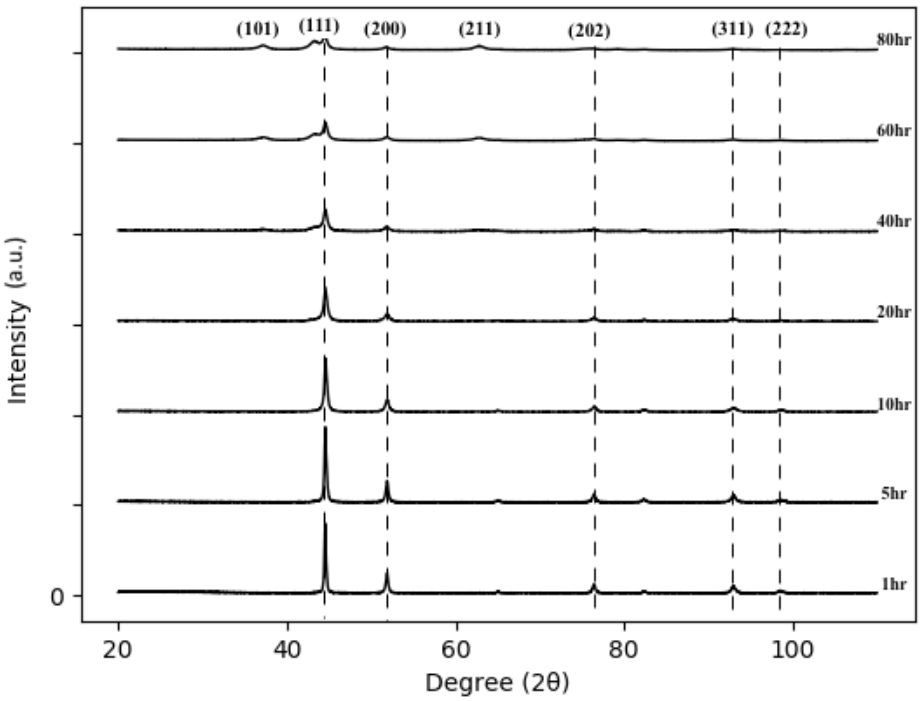


Figure 3.8: XRD graphs of Fe-Ni powders synthesized by mechanical alloying with 250 rpm milling speed under dry atmosphere

From the XRD curves of the Fe-Ni powders synthesized by mechanical alloying with 250 rpm under the dry atmosphere, it has been observed that Fe individual peaks disappeared as the milling time increased to 40 hours. On the other hand, Fe peaks vanished earlier in the XRD graphs of the samples obtained from 400 rpm milling under dry atmosphere.

Table 3.2: Chemical composition of the alloyed particles with respect to milling time for the dry milling with 250 rpm

| | 1 hr | 5 hr | 10 hr | 20 hr | 40 hr | 60 hr | 80 hr |
|---|---|---|---|---|---|---|---|
| Fe (At%) | 81.16 | 12.39 | 19.81 | 33.84 | 25.52 | 28.42 | 24.3 |
| Ni (At%) | 18.84 | 87.61 | 80.19 | 66.16 | 74.48 | 71.58 | 75.70 |

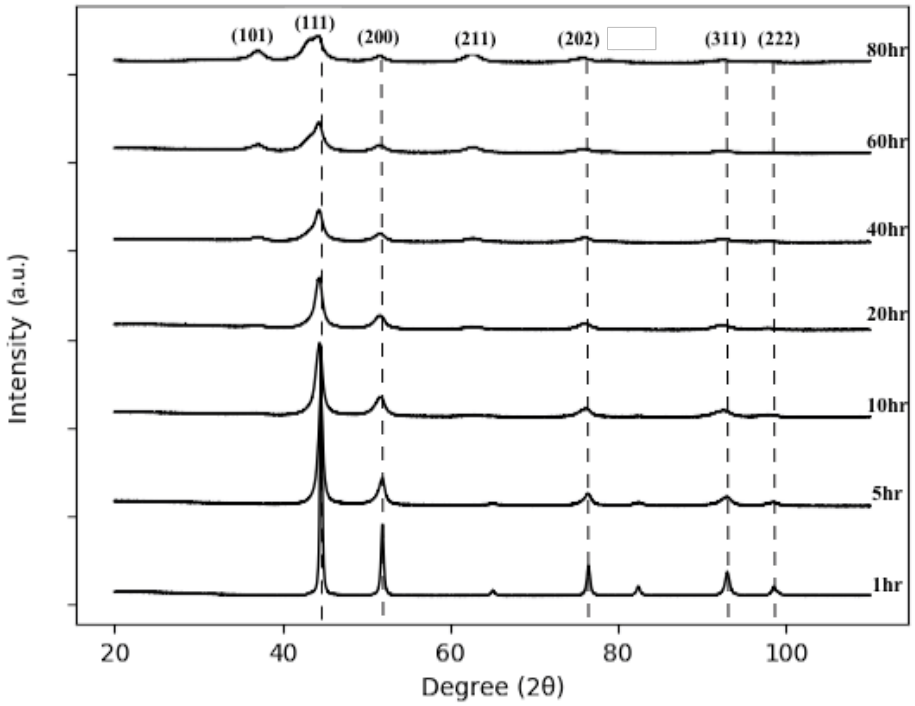


Figure 3.9: XRD graphs of Fe-Ni powders synthesized by mechanical alloying with 400 rpm milling speed under dry atmosphere

Table 3.3: Chemical composition of the alloyed particles with respect to milling time for the dry milling with 400 rpm

| | 1 hr | 5 hr | 10 hr | 20 hr | 40 hr | 60 hr | 80 hr |
|---|---|---|---|---|---|---|---|
| Fe (At%) | 86.82 | 26.32 | 28.15 | 22.46 | 24.57 | 23.97 | 24.17 |
| Ni (At%) | 13.18 | 73.68 | 71.85 | 77.54 | 75.43 | 76.03 | 75.83 |

According to the XRD curves, the fundamental peaks of the face-centered cubic structure (A1) for $FeNi_3$ system were observed, at the beginning. Fundamental peaks are strong and occur when h,k,l are all even or all odd. After 40 hour milling time of the mechanical alloying with 400 rpm under dry conditions, superstructure lines of ordered simple cubic ($L1_2$) structure for $FeNi_3$ system started to be observed which means that mechanical alloying for the synthesis of $FeNi_3$ system started and the order degree of the alloy system increased. Superstructure peaks are weak and occur when

h, k, l are mixed. However, some of the superstructure peaks of the $L1_2$ structure could not be obtained, such as (100), (201), (301) from the XRD analysis conducted in D8 Advance Bruker with Cu-K$\alpha$ radiation at a wavelength of 1.540562 angstroms.

In order to observe all superstructure peaks clearly, the incident wavelength to the wavelength of the K absorption edge for the scattering element should be close to each other; however, if the ratio is less than 0.8, the intensity of superlattice peaks becomes negligible [94]. For $FeNi_3$ system, with Cu radiation in X-Ray diffraction, the ratio of the incident wavelength to the wavelength of the K absorption edge of the scattering element is approximately equal to 0.8 so super lattice lines couldn't be observed clearly and the exact value of long-range order parameter could not be determined.

The formation of the mechanical alloying in high energy dry milling with 250 rpm and 400 rpm was also proven with EDS results which are shown in Table 3.2 and in Table 3.3. According to quantitative results, in the early stages of milling, there were particles consisting of different combinations of the constituents but after 40-hour milling, the target 1:3 iron to nickel atomic ratio was mainly provided.

Although the elemental analysis became constant after 40 hours, regarding XRD analysis, the alloying was completed at higher milling times for the mechanical alloying with 250 rpm milling speed. On the other hand, according to structural and quantitative results obtained from XRD and EDS analysis, it was observed that the mechanical alloying was completed after 40-hour milling for the mechanical alloying with 400 rpm under dry conditions. Therefore, surfactants and solvent inserted into the system once the mechanical alloying completed for the two-step mechanical alloying at 40 hours. Figure 3.10 shows the XRD graphs of the samples produced by the two-stage mechanical alloying. Furthermore, the EDS results of the samples from the two-step mechanical alloying are listed in Table 3.4.

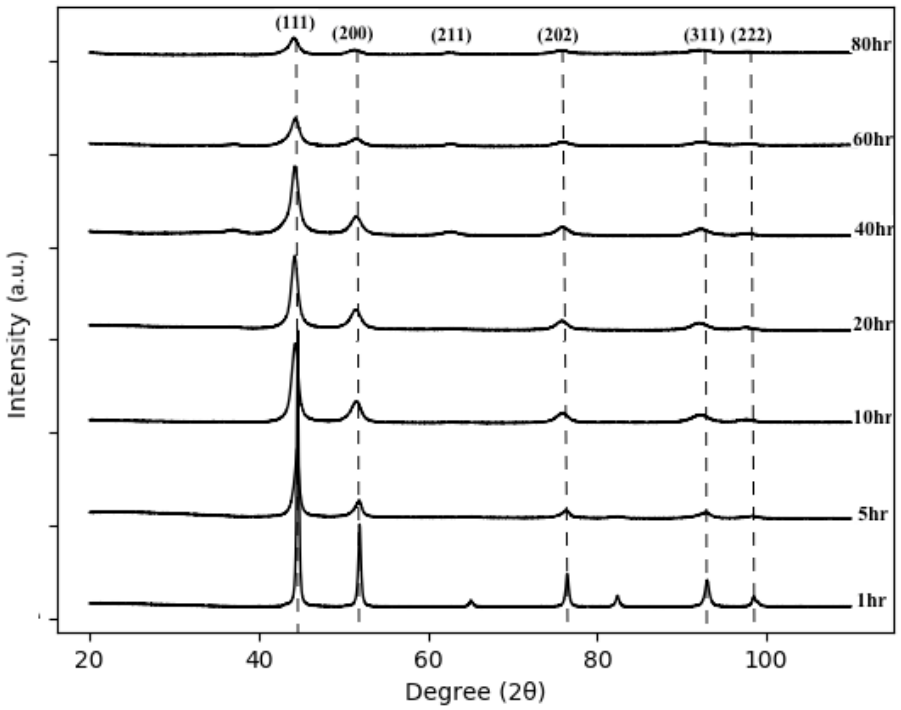


Figure 3.10: XRD graph of Fe-Ni powders synthesized by the-two-step mechanical alloying with 400 rpm milling speed for different milling periods

Table 3.4: Chemical composition of the alloyed particles with respect to milling time for the two-step mechanical alloying with 400 rpm

| | 1 hr | 5 hr | 10 hr | 20 hr | 40 hr | 60 hr | 80 hr |
|---|---|---|---|---|---|---|---|
| Fe (At%) | 3.36 | 23.12 | 24.27 | 24.49 | 24.64 | 24.78 | 24.83 |
| Ni (At%) | 96.64 | 76.88 | 75.73 | 75.51 | 75.36 | 75.22 | 75.17 |

In the XRD diffractograms of the samples synthesized by mechanical alloying, the intensities and the position of the diffraction peaks were consistent with the literature and according to the XRD graphs of each system, it was seen that the peaks became wider as the milling time increased which showed the decrease in the crystallite size of the $FeNi_3$ powders. Also, there was an angular shift on the Ni peaks towards lower angles with the higher milling times. This was the sign of the first order stress induced by milling and the formation of $FeNi_3$ phase alloy which led to modify the

lattice parameter [73, 91].

The crystallite size change estimated by using the Modified Scherrer Method with respect to milling time for different milling conditions (250 rpm and 400 rpm milling speeds, with and without surfactant) is illustrated in Figure 3.11. It can be seen that as the milling speed increased, the smaller crystallite size could be obtained. However, surfactant usage after 40 hours did not have any positive effect on the reducing crystallite size. Therefore, the smallest crystallite size was obtained by the dry milling with 400 rpm milling speed.

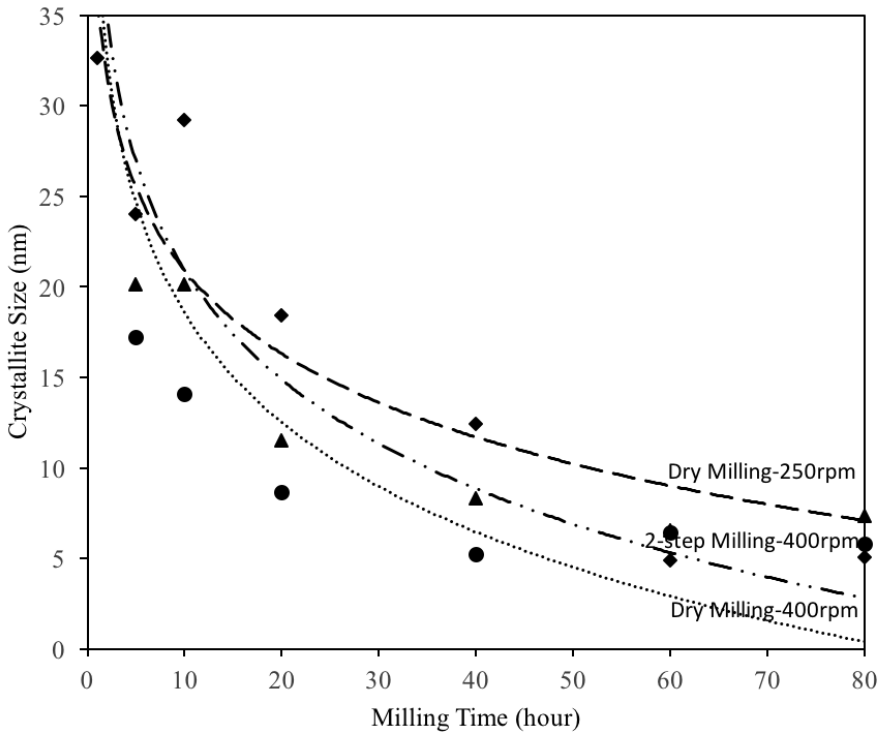


Figure 3.11: Crystallite size change of $FeNi_3$ powders with respect to milling time

Also, the determined strain and crystallite size values from Williams-Hall method and Modified Sherrer Method for different milling time are listed in Table 3.5-3.7.

Table 3.5: Crystallite size and strain values with respect to milling time for the dry milling with 250 rpm

| | Williamson-Hall Method | | Modified Scherrer Method |
|---|---|---|---|
| Milling Time (hour) | Strain (%) | Size (nm) | Size (nm) |
| 1 | 0.06 | 53.635 | 32.652 |
| 5 | -0.07 | 48.272 | 24.030 |
| 10 | 0.15 | 20.113 | 29.210 |
| 20 | 0.11 | 21.941 | 18.404 |
| 40 | -0.37 | 7.313 | 12.442 |
| 60 | -1.97 | 3.344 | 4.898 |
| 80 | -0.67 | 5.815 | 5.050 |

Table 3.6: Crystallite size and strain values with respect to milling time for the dry milling with 400 rpm

| | Williamson-Hall Method | | Modified Scherrer Method |
|---|---|---|---|
| Milling Time (hour) | Strain (%) | Size (nm) | Size (nm) |
| 1 | 0.17 | 46.715 | 29.5124 |
| 5 | 0.12 | 17.240 | 15.212 |
| 10 | 0.42 | 14.059 | 8.3538 |
| 20 | 0.19 | 8.671 | 7.962 |
| 40 | -0.42 | 5.247 | 6.0788 |
| 60 | -0.43 | 6.465 | 6.371 |
| 80 | -0.46 | 5.815 | 4.590 |

Table 3.7: Crystallite size and strain values with respect to milling time for two-step mechanical alloying with 400 rpm

| | Williamson-Hall Method | | Modified Scherrer Method |
|---|---|---|---|
| Milling Time (hour) | Strain (%) | Size (nm) | Size (nm) |
| 1 | 0.2 | 46.715 | 29.601 |
| 5 | 0.2 | 20.113 | 15.198 |
| 10 | 0.4 | 20.113 | 11.481 |
| 20 | 0.19 | 11.493 | 9.681 |
| 40 | 0.24 | 8.3227 | 7.803 |
| 60 | 0.0005 | 6.5232 | 6.434 |
| 80 | 0.03 | 7.351 | 7.885 |

According to Table 3.5-3.7, the crystallite size was decreasing with the increasing milling time. In terms of the strain variation, the strain values of the samples from 250 rpm milling speed mainly fluctuated throughout the mechanical alloying process. although the strain values of the samples from two-step mechanical alloying approached to zero value at higher milling times, they varied irregularly at the beginning. On the other hand, the strain values of the samples from the mechanical alloying with 400 rpm under dry atmosphere exhibited different trend compared to others. Although varying tensile strain was found with different values until 40 hours because of the alloying and welding, compressive strain appeared at higher milling times due to the smaller crystallite size.

At the earlier stage of the milling, it is probable that the main reason of the microstrain was the plastic deformation, and consequently dislocation density. However, at the higher milling time, the strain of the sample from the dry milling with 400 rpm became stable because the main effect of the microstrain probably was the grain boundary volume fraction and at that time grain boundary fraction remained constant. The effect of the atomic mismatch was negligible on the microstrain because of the insignificant size difference between Fe and Ni atoms Gheisari2013.

Furthermore, lattice parameters of $FeNi_3$ nanoparticles were determined from the

equation 3.4 by utilizing XRD data and the calculated values are listed in Table 3.8. The calculated lattice parameters are agreeable with the literature.

Table 3.8: Lattice parameter of synthesized $FeNi_3$ nanoparticles for different milling times

| Milling Time | Lattice Parameter (Dry MA-250rpm) | Lattice Parameter (Dry MA-400rpm) | Lattice Parameter (2-step MA) |
|---|---|---|---|
| 1 hour | 3.522 Å | 3.518 Å | 3.519 Å |
| 5 hours | 3.523 Å | 3.5207 Å | 3.503 Å |
| 10 hours | 3.524 Å | 3.539 Å | 3.549 Å |
| 20 hours | 3.525 Å | 3.538 Å | 3.559 Å |
| 40 hours | 3.522 Å | 3.545 Å | 3.533 Å |
| 60 hours | 3.523 Å | 3.545 Å | 3,535 Å |
| 80 hours | 3.523 Å | 3.543 Å | 3.540 Å |

From Table 3.8, it is seen that as the milling speed was increased from 250 rpm to 400 rpm, the lattice parameter of the synthesized powders increased because the higher milling speed led to larger kinetic energy into the powders which increased the lattice parameter [89]. Although the lattice parameters of the powders from the dry milling with 250 rpm and two-step mechanical alloying did not change significantly, the lattice parameters of the samples from the mechanical alloying with 400 rpm under dry atmosphere were mainly increased. This increase in lattice parameter caused because of the crystallite size reduction, and consequently lattice expansion [90]. Also, the closest lattice parameter value to the literature (3.5525 A [73]) was obtained from the mechanical alloying with 400 rpm milling speed under the dry atmosphere, which was 3.543 Å.

To investigate particle morphology (spherical, cubic, stick, etc.) and changes in the particle size, scanning electron microscopy has been used. The results of scanning electron microscopy studies are shown in Figure 3.12, Figure 3.13 and Figure 3.14 for the dry milling with 250 rpm, dry milling with 400 rpm and wet milling with 400 rpm milling speed, respectively.

From the SEM images, it has been seen that the 1-hour milled powders had a relatively narrow particle size distribution in the micron range. After 5 hour milling, the shape of the particles became layered because of the welding. With further increase of milling time, the layered particles changed to ultra-fine particles for dry and wet milling with 250 rpm and 400 rpm. However, the agglomeration could not be prevented completely, and non-homogeneous particle size distribution was obtained as the milling time increases.

To compare the average particle size of the nanostructured $FeNi_3$ alloys synthesized from different milling parameters, SEM images of 80-hour milled samples with high magnification were illustrated in Figure 3.15.

Although there was a considerable decrease in the particle size of the nanoparticles obtained from dry milling at 250 rpm, the nanostructured particles which had dimensions smaller than 100 nm were rarely seen. On the other hand, with dry milling with 400 rpm milling speed, it has been observed that there was a considerable amount of nanostructured $FeNi_3$ alloyed particles which were smaller than 100 nm. However, due to having the magnetic property, images with high resolution could not be obtained in higher magnifications, so smaller particles than 38 nm could not be identified in SEM analysis. In addition, the sample from the two-step mechanical alloying with 400 rpm also contained smaller particles than 100nm, but a significant difference in particle size between dry milling with 400 rpm and the two-step mechanical alloying was not observed.

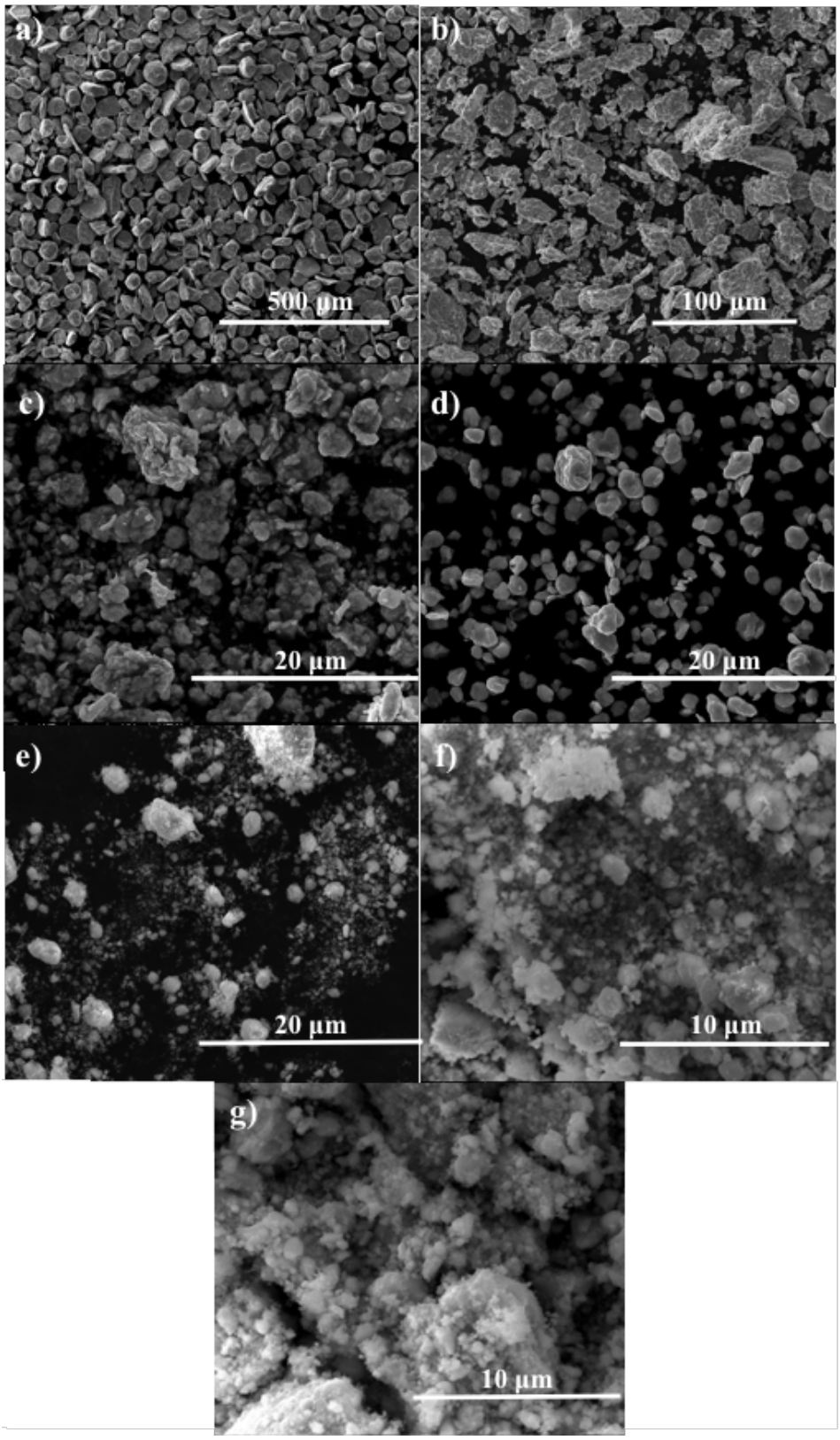


Figure 3.12: SEM images of $FeNi_3$ powders from mechanical alloying with 250 rpm milling speed under dry conditions after a) 1 hour b) 5 hours c) 10 hours d) 20 hours e) 40 hours f) 60 hours g) 80 hours

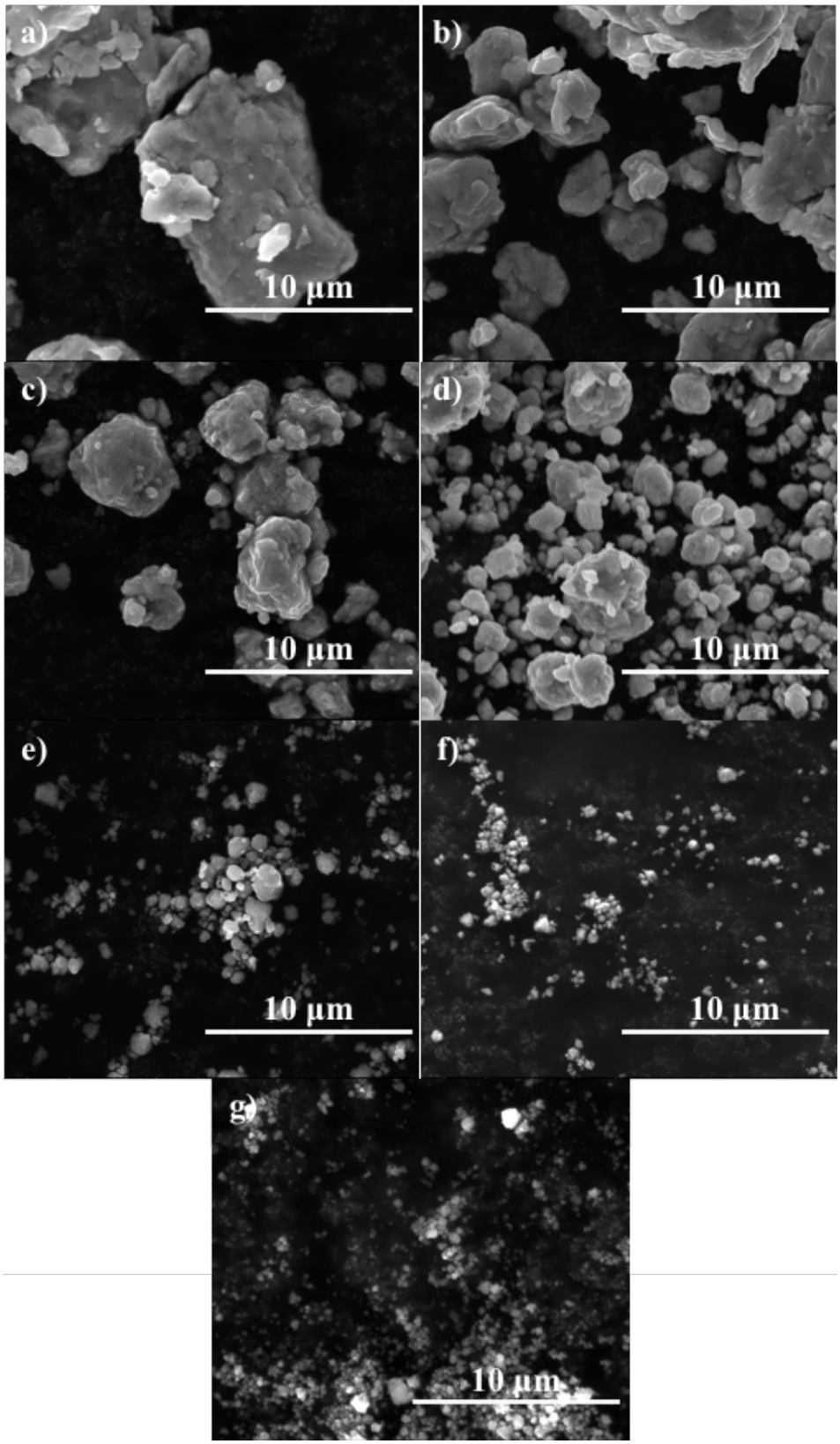


Figure 3.13: SEM images of $FeNi_3$ powders from mechanical alloying with 400 rpm milling speed under dry conditions after a) 1 hour b) 5 hours c) 10 hours d) 20 hours e) 40 hours f) 60 hours g) 80 hours

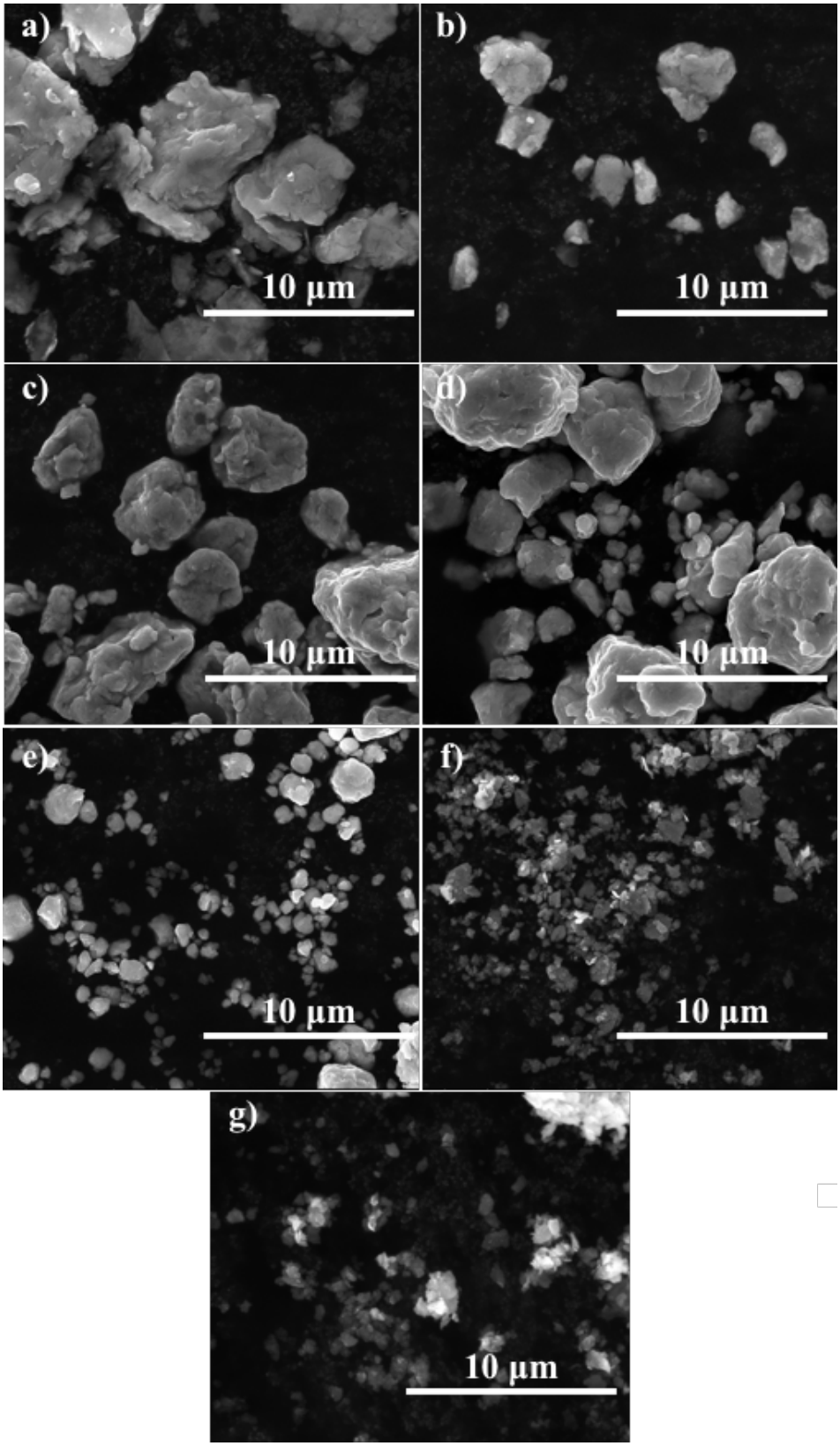


Figure 3.14: SEM images of $FeNi_3$ powders from two-step mechanical alloying with 400 rpm after a) 1 hour b) 5 hours c) 10 hours d) 20 hours e) 40 hours f) 60 hours g) 80 hours

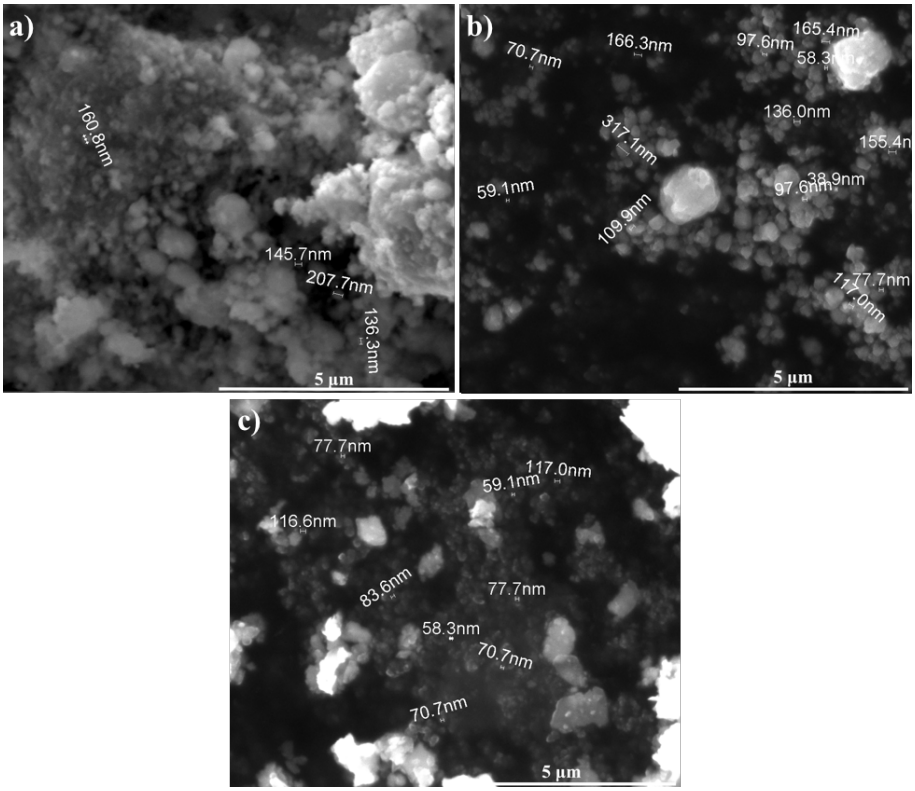


Figure 3.15: Average particle size determination of the synthesized nanoalloyed $FeNi_3$ particles after 80-hour milling a) SEM image of the powders alloyed under dry atmosphere with 250 rpm b) SEM image of the powders alloyed under dry atmosphere with 400 rpm c) SEM image of the powders from two-step mechanical alloying with 400 rpm

The effect of the milling parameters on the magnetic behavior of the alloyed nanoparticles was investigated by the hysteresis curve which was obtained from vibrating-sample magnetometer (VSM). The hysteresis curves of $FeNi_3$ nanoalloys obtained from the dry milling with 250 rpm, dry milling with 400 rpm and 2-step mechanical alloying with 400 rpm are illustrated in Figure 3.16, Figure 3.17 and Figure 3.18, respectively. Also, the magnetic parameters determined from the hysteresis curve are listed in Table 3.9, Table 3.10 and Table 3.11. In the tables, $M_s$, $M_r$, S, $H_c$, $\mu_{max}$ represent saturation magnetization, remanence, squareness ($M_r/M_s$), coercivity and maximum permeability, respectively.

As it is seen from the Hysteresis curve, the synthesized powders had soft magnetic

behavior, but as the milling time and the milling speed were increased, smaller coercivity values were obtained.

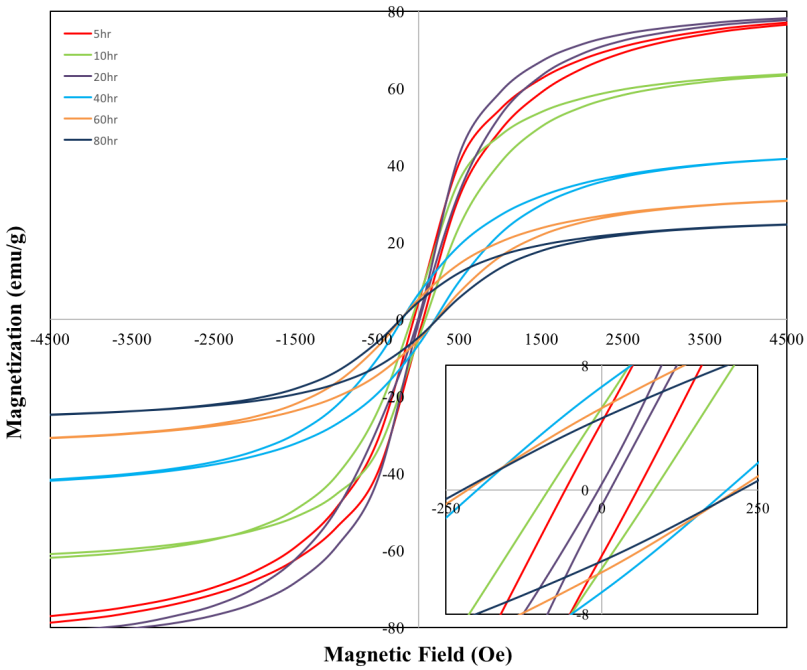


Figure 3.16: Hysteresis curves of $FeNi_3$ powders from mechanical alloying with 250 rpm for different milling times

Table 3.9: Magnetic properties of $FeNi_3$ powders synthesized by mechanical alloying with 250 rpm for different milling time

| Milling Time (hr) | 5 | 10 | 20 | 40 | 60 | 80 |
|---|---|---|---|---|---|---|
| $M_s$ (emu/g) | 83.66 | 66.31 | 83.82 | 45.96 | 34.13 | 27.43 |
| $M_r$ (emu/g) | 4.29 | 5.17 | 0.72 | 6.60 | 5.28 | 4.59 |
| $H_c$ (Oe) | 59.52 | 88.26 | 11.16 | 197.92 | 213.62 | 221.50 |
| $BH_{max}$ | 10539 | 7531 | 9206 | 3201 | 3421 | 3176 |
| $\mu_{max}$ (emu/Oe) | 0.0020 | 0.0014 | 0.002 | 0.0005 | 0.0005 | 0.0005 |

Table 3.9 showed that saturation magnetization and the amount of energy dissipation of the samples from dry milling with 250 rpm decreased at higher milling times, but coercivity increased probably due to the unalloyed particles remained in the sample.

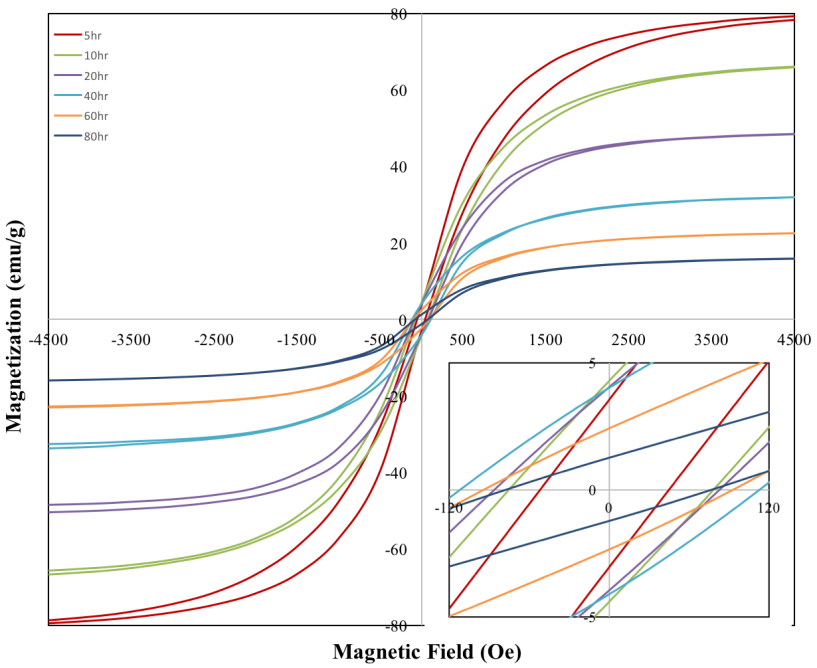


Figure 3.17: Hysteresis curves of $FeNi_3$ powders from mechanical alloying with 400 rpm for different milling times

Table 3.10: Magnetic properties of $FeNi_3$ powders synthesized by mechanical alloying with 400 rpm for different milling time

| Milling Time(hr) | 5 | 10 | 20 | 40 | 60 | 80 |
|---|---|---|---|---|---|---|
| $M_s$(emu/g) | 83.06 | 69.58 | 51.45 | 34.86 | 24.40 | 17.36 |
| $M_r$(emu/g) | 3.30 | 4.33 | 3.99 | 4.05 | 2.37 | 1.24 |
| $H_c$(Oe) | 52.46 | 76.20 | 83.09 | 106.77 | 89.36 | 74.72 |
| $BH_{max}$ | 10136 | 8475 | 6144 | 4147 | 2876 | 2184 |
| $\mu_{max}(emu/Oe)$ | 0.0019 | 0.0015 | 0.0012 | 0.0009 | 0.0006 | 0.0004 |

For the powders which were mechanically alloyed with 400 rpm under the dry condition, coercivity increased until 40 hours due to the formation of the $FeNi_3$ phase. Then the coercivity started to decrease with longer milling times because of the complete formation of alloy, the relaxation of the lattice strain and the decrease in the crystallite/particle size. Moreover, at higher milling times, the remanence, saturation

magnetization and the dissipated energy also decreased.

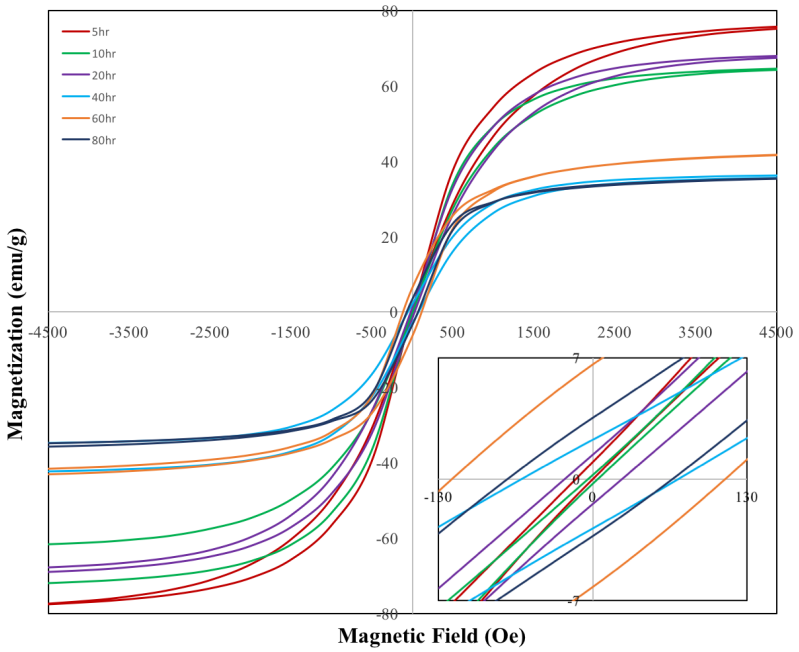


Figure 3.18: Hysteresis curves of $FeNi_3$ powders from two-stage mechanical alloying for different milling times

Table 3.11: Magnetic properties of $FeNi_3$ powders synthesized by two-step mechanical alloying for different milling time(400rpm-wet)

| Milling Time(hr) | 5 | 10 | 20 | 40 | 60 | 80 |
|---|---|---|---|---|---|---|
| $M_s$(emu/g) | 79.78 | 70.26 | 70.78 | 40.62 | 44.64 | 37.29 |
| $M_r$(emu/g) | 0.51 | 0.28 | 1.43 | 2.56 | 6.40 | 3.40 |
| $H_c$(Oe) | 8.02 | 5.05 | 25.96 | 67.73 | 111.48 | 67.34 |
| $\mu_{max}$ (emu/Oe) | 0.0018 | 0.0019 | 0.0017 | 0.0010 | 0.0014 | 0.0014 |

The coercivity values of the synthesized powders from two-step mechanical alloying fluctuated as the milling time increases which are probably because of the change in lattice strain and magnetic measurement conditions [89, 90]. Also, the saturation magnetization of the 2-step mechanically alloyed powders increased between 40 hours and 60 hours probably because of the presence of unalloyed Ni and Fe which

are below the detection limit of XRD [19, 73].

Among the samples, the $FeNi_3$ nanopowder synthesized with 400 rpm milling speed at 80 hour milling time under the dry atmosphere showed the softest magnetic properties having lowest:

- Saturation magnetization of Ms=17.36 emu/g (magnitude of which is lower than the value of bulk counterparts (125 emu/g [98])
- Coercivity of Hc=74.72 Oe (much smaller than the coercivity of bulk $FeNi_3$ alloys (500–800 Oe [99])
- Remanence (1.24 emu/g) and
- The energy product of BHmax=2184

To investigate the magnetic behavior of the nanostructured $FeNi_3$ alloys, a large amount of samples should have been taken and the nanoparticles should have been separated from the large particles before conduct VSM analysis. However, in order not to affect the powder to ball ratio, the small amount of samples which contained not only nanostructured particles but also large ones had to be taken. As a result of this, superparamagnetic behavior of the $FeNi_3$ nanoalloys could not be observed. Superparamagnetic materials should have very small values of $H_c$ and $M_r$ (close to zero). Although in this experimental study, we couldn't obtain superparamagnetic behavior, the decrease of $H_c$ and $M_r$ values of the alloyed powders with 400 rpm under dry atmosphere showed that the synthesized nanopowders were close to having superparamagnetic properties at room temperature.

# CHAPTER 4

# SUMMARY AND CONCLUSION

## 4.1 Summary of Findings

In this study, Fe-Ni nanoalloys have been investigated by means of theoretical and experimental methods. In the theoretical part, the effects of temperature (300-1700 K), size (2 nm-6 nm) and shape (spherical and cubic) on the structural evolution of the crystalline and amorphous Fe-Ni nanoalloys have been studied by using molecular dynamics (MD) method combined with embedded atom model (EAM) in Large-scale Atomic/Molecular Massively Parallel Simulator (LAMMPS). In experimental part, $FeNi_3$ bimetallic nanoalloys were synthesized by mechanical alloying with different milling speeds under dry atmosphere and the by the two-step mechanical alloying process in a planetary high energy ball milling. The results of theoretical and experimental investigations may be summarized as follows:

A. Modeling and simulation studies:

Firstly, the $FeNi_3$ nanosystems with crystalline structures were modeled by assuming that systems with more than 100 atoms have the same crystal structure as their bulk counterpart. Then, the temperature augmentation process applied to the modeled crystalline nanoparticles with different size and shape. Afterward, the spherical nanoparticles with 2 nm, 4 nm, and 6 nm diameter were also obtained by subtracting them from the simulated unstable amorphous bulk counterpart. The subtracted amorphous particles were melted to remove local atomic configurations from their solid phase and they incrementally cooled down to room temperature. Finally, the structural evolution of these nanoparticles at a wide temperature range (300-1700 K) was analyzed by means of radial distribution functions, coordination numbers, core-

to-surface concentration profiles, surface energy and Voronoi analysis.

- Structural analysis indicated that all the crystalline nanoparticles deformed at high temperatures, but as the size of the particle increased to 6 nm, the deformation became negligible and the 6 nm particles exhibited the most heat-resistant behavior while conserving their stable cage structure, due to the decrease in the surface-to-volume ratio;

- The melting point of the particles exhibited strongly size and shape dependence behavior. Due to the decrease in the surface to volume ratio of the particles, increasing particle size led to higher melting temperatures which approached to the melting point of the bulk phase. On the other hand, although, cubic nanoparticle had a higher surface to volume ratio, the melting temperature was close to the melting point of the 4 nm nanoparticle because of the similar surface area which showed the shape effect;

- According to the spatial ordering of the nanoparticles, generally, ordered mixed pattern was achieved without segregation or core-shell structure, although some Ni atoms preferred to locate at the core-side of the 2nm nanoparticle;

- From the Voronoi tessellations, exact polyhedral structures could not be identified but distorted polyhedral forms were found from the total number of polyhedron faces and the ratio of the i-edged faces to the total number of the faces. According to Voronoi analysis, the 2 nm amorphous nanoparticles had fully icosahedral structure and its derivatives at room temperature. However, as the particle size increased to 6 nm, icosahedral structure vanished and deformed truncated octahedron polyhedrons appeared with a high degree of rectangularity which is a stable polyhedral form of the FCC lattice structure for the larger nanoparticles;

- The surface energy of the spherical nanoparticles with crystalline structure tended to decrease until 1300 K which means they became more stable at 1300 K. Afterward, the surface energy started to increase. The probable reason for this unusual behavior, i.e. surface energy anomaly (positive temperature coefficient) is that the surface topology and atomic arrangement significantly differed

from the inner part of the particle and a denser structure was occurred in the liquid phase compared to the solid phase;

- The surface energy of the amorphous particles showed different trends. During the cooling of the amorphous nanoparticles from high temperatures to room temperature, the nanoparticles achieved their most stable structures at 300 K by self-assembly. The larger particles formed the deformed truncated octahedron structure, as it has been expected. However, when the size decreased to 2nm, icosahedron polyhedral structure was formed with the compact surface morphology and minimum surface energy due to the fivefold symmetry of the nanoparticles below the critical size. Therefore, the surface energy of the amorphous $FeNi_3$ nanoparticles tended to be lowered as the particle size decreased at room temperature, due to the capability of the small particles to form denser structure, especially at the surface, during the cooling process.

B. Experimental studies:

The experimental studies were carried out in three ways. Firstly, mechanical alloying with 250 rpm milling speed in high energy dry planetary ball milling was applied to obtain $FeNi_3$ nanoparticles. Secondly, the milling speed increased to 400 rpm to investigate the milling speed influence on the characteristics of the powders. Furthermore, two-step mechanical alloying was performed in which dry milling was followed by surfactant-assisted ball milling to observe the surfactant and solvent effect on the structure, size, and magnetic properties of the $FeNi_3$ nanoalloys. During two-step mechanical alloying, heptane was used as milling medium, and as surfactants, oleic acid and oleylamine were used. The powder sample of iron-nickel was prepared according to the 1:3 iron to nickel ratio to produce $FeNi_3$ nanoparticles and the 1:10 powder to ball weight ratio. In order to avoid oxidation during milling, the vials had been filled with Ar inert gas before milling started. The structural and magnetic properties the alloyed nanoparticles have been analyzed by using XRD, SEM, EDS, and VSM techniques.

- The synthesis of the $FeNi_3$ intermetallic nanoparticles was succeeded by mechanical alloying in 40 hours and the powders milled for 80 hours in total. After

80-hour milling, there were no additional intermetallic compounds or contaminants;

- It is shown that particle size and crystallite size decreased with higher milling time and increasing milling speed from 250 rpm to 400 rpm;
- However, surfactant usage in the two-step mechanical alloying did not have a significant influence on the crystallite or particle size change;
- From the VSM analysis, it has been observed that, in general, the $FeNi_3$ nanopowders exhibited soft magnetic behavior at higher milling times and magnetic properties of the $FeNi_3$ nanoalloy particles were strongly dependent on the particle and crystallite size;
- The coercivity and saturation magnetization values of the samples from the dry mechanical alloying with 250 rpm and from the two-step mechanical alloying were fluctuated due to the existence of the lattice strain and the unalloyed nanoparticles which could not be observed from XRD and EDS analysis.
- The coercivity and saturation magnetization of the samples from dry mechanical alloying with 400 rpm under dry atmosphere became lowered due to the completion of the alloying and the decrease in the particle/crystallite size.

## 4.2 Conclusion

From the theoretical studies for the modeling and the simulations of the nanoparticles by molecular dynamics method with embedded atom model, it has been clearly observed that the structural evolution, melting point, surface energies and atomic arrangements of the nanoparticles were strongly size and shape dependent. During the simulations, the way of modeling did not affect significantly the final stable crystalline structure with a mixing pattern of the 6 nm $FeNi_3$ nanoparticles at room temperature, and both the initially crystalline and amorphous 6 nm nanoparticles owned the same FCC crystalline lattice structure owing 3.5 Å lattice parameter and 12-13 coordination number with truncated octahedron polyhedrons in local atomic arrangements, even though they were modeled in different ways. These results imply that the initial assumption about systems with more than 100 atoms owing identical crystalline

structure with the crystalline bulk $FeNi_3$ intermetallic has been validated for the 6nm nanoparticles. However, as the diameter decreased to 2 nm with 360 or 368 atoms, some deviations appeared in the assumption and structure of amorphous nanoparticles became different from its crystalline counterparts.

In experimental studies, the synthesis of the $FeNi_3$ intermetallic nanoparticles was succeeded in 40 hours of milling via mechanical alloying with 400 rpm milling speed under dry conditions and the powders were milled for 80 hours in total to obtain nanoparticles which are smaller than 100 nm. On the other hand, 250 rpm milling speed was not high enough to complete mechanical alloying and surfactant usage inhibited the further alloying process in the two-step mechanical alloying process. During the experimental studies, it has been shown that the crystallite and particle size decreased with increasing milling time and speed. However, surfactant usage in the two-step mechanical alloying did not have a significant influence on the decrease of the crystallite and/or particle size. Therefore, the smallest, $L1_2$-type ordered $FeNi_3$ nanopowders having 5.8 nm crystallite size, -0.46% strain value, and 3.54 Å lattice parameter were synthesized by means of dry milling with 400 rpm milling speed after 80 hour milling time. Moreover, it has been deduced that, in general, the soft magnetic behavior of the $FeNi_3$ nanopowders was strongly dependent on the particle and crystallite size. However, due to the wide range particle size distributions in the samples of synthesized nanopowders, the superparamagnetic behavior could not be detected. On the other hand, the nanopowders synthesized by dry mechanical alloying with 400 rpm showed the closest magnetic behavior to super-paramagnetic materials at room temperature because of having the smallest crystallite and particle size.

## 4.3 Future Works

For future work, the magnetic and electronic behavior of the $FeNi_3$ nanoparticles would be investigated in detail by using various computational methods to establish a relationship between the structural, magnetic and electronic properties. Moreover, the surface energy variation of the nanoparticles with temperature, particle size and shape should be investigated to enlighten the surface properties of the $FeNi_3$ nanoparticles, which is more important especially for the catalytic and biomedical applications of

nanoalloys. Furthermore, more experimental investigations needed to synthesize Fe-Ni nanopowders having a smaller particle size with superparamagnetic behavior by varying milling speeds and milling times. Then, the degradation and the oxidation behavior of Fe-Ni nanopowders should be determined for the potential usage of them as radar absorbing materials, catalysts, and biomedical applications.

# REFERENCES


[1] ASM International. *ASM Handbook, Volume 3, Alloy Phase Diagrams*, volume 7. 2004.

[2] Christian Alloyeau, Damien; Mottet, Christine; Ricolleau. *Nanoalloys Synthesis, Structure and Properties*. Springer, 2012.

[3] Riccardo Ferrando, Julius Jellinek, and Roy L Johnston. Nanoalloys : From Theory to Applications of Alloy Clusters and Nanoparticles. 108(3), 2008.

[4] Shan X Wang and Alexander M Taratorin. Chapter 1 - Introduction. In Shan X Wang and Alexander M Taratorin, editors, *Magnetic Information Storage Technology*, Electromagnetism, pages 1–30. Academic Press, San Diego, 1999.

[5] Sakir Erkoc. Lecture Notes on Simulations Simulations of Many – Particle Systems. Technical report, 2004.

[6] Le Roux Sebastian and Valeri Petkov. Model Box Periodic Boundary Conditions - P.B.C.

[7] Alaei Sholeh. *Structural, Electronic and Magnetic Properties of Various Nanosystems: Molecular Dynamics Simulations and Density Functional Theory Calculations*. PhD thesis, Middle East Technical University, 2014.

[8] C. C. Wang, K. J. Dong, and A. B. Yu. Analysis of Voronoi clusters in the packing of uniform spheres. In *AIP Conference Proceedings*, volume 1542, pages 353–356, 2013.

[9] Romain Breitwieser, Ulises Acevedo, Souad Ammar, and Raul Valenzuela. Ferrite nanostructures consolidated by spark plasma sintering (sps). In Mohindar Singh Seehra, editor, *Nanostructured Materials - Fabrication to Applications*, chapter 02. InTech, Rijeka, 2017.

[10] C. C. Koch and J. D. Whittenberger. Mechanical milling/alloying of intermetallics. *Intermetallics 4*, 4(5):339–355, 1994.

[11] Lu; Man On Lai Li. *Mechanical Alloying*. Springer US, 1998.

[12] C. Suryanarayana. Chapter 4 Mechanical alloying. In *Pergamon Materials Series*, volume 2, pages 49–85. 1999.

[13] William D Callister and John Wiley. *Materials Science and Engineering*. 2007.

[14] Daniel Schodek, Paulo Ferreira, and Michael Ashby. *Nanomaterials, Nanotechnologies and Design*. 2009.

[15] Sherif Moussa, Victor Abdelsayed, and M.S. El Shall. Chemical synthesis of metal nanoparticles and nanoalloys. In *Nanoalloys*, pages 1–37. Elsevier Inc., 2013.

[16] Karrina McNamara and Syed A.M. Tofail. Biomedical applications of nanoalloys. In *Nanoalloys*, pages 345–371. Elsevier Inc., 2013.

[17] F Baletto and R Ferrando. Structural properties of nanoclusters: Energetic, thermodynamic, and kinetic effects RID C-4066-2011. *Reviews Of Modern Physics*, 77(1):371–423, 2005.

[18] Andrés A. Aguado. Modeling the electronic and geometric structure of nanoalloys. In *Nanoalloys*, pages 75–111. 2013.

[19] I. Chicinas. Soft magnetic nanocrystalline powders produced by mechanical alloying routes. *Journal of Optoelectronics and Advanced Materials*, 8(2):439–448, 2006.

[20] Sergei P Gubin, Yurii A Koksharov, G B Khomutov, and Gleb Yu Yurkov. Magnetic nanoparticles: preparation, structure and properties. *Russian Chemical Reviews*, 74(6):489–520, 2005.

[21] C Suryanarayana. Chapter 35 Nanostructured Intermetallics. In Fleischer Westbrook J. H. and R. L., editors, *Intermetallic Compounds, Principles and Practice*, volume 3. John Wiley & Sons Ltd, 2002.

[22] E. Cottancin and M. Pellarin. Optical probes of the chemical structure in metallic nanoalloys. In *Nanoalloys*, pages 203–245. 2013.

[23] Eleonora Petryayeva and Ulrich J. Krull. Localized surface plasmon resonance: Nanostructures, bioassays and biosensing-A review, 2011.

[24] Hui Zhao, Zhenghou Zhu, Chao Xiong, Xialian Zheng, and Qianying Lin. The influence of different Ni contents on the radar absorbing properties of FeNi nano powders. pages 16413–16418, 2016.

[25] P. H. Zhou, L. J. Deng, J. L. Xie, D. F. Liang, L. Chen, and X. Q. Zhao. Nanocrystalline structure and particle size effect on microwave permeability of FeNi powders prepared by mechanical alloying. *Journal of Magnetism and Magnetic Materials*, 292:325–331, 2005.

[26] Dominique Bazin, Ioana Fechete, François C. Garin, Giovanni Barcaro, Fabio R. Negreiros, Luca Sementa, and Alessandro Fortunelli. Reactivity and catalysis by nanoalloys. In *Nanoalloys*, pages 283–344. 2013.

[27] Younan Xia, Yujie Xiong, Byungkwon Lim, and Sara E Skrabalak. Shape-Controlled Synthesis of Metal Nanocrystals:Simple Chemistry Meets Complex Physics?, 2008.

[28] L. J. Swartzendruber. The Fe-Ni (Iron-Nickel) System. *Journal of Phase Equilibria*, 12(3), 1991.

[29] G Bonny, R C Pasianot, and L Malerba. Fe–Ni many-body potential for metallurgical applications. *Modelling and Simulation in Materials Science and Engineering*, 17:025010, 2009.

[30] Y. Mishin, M. J. Mehl, and D. A. Papaconstantopoulos. Phase stability in the Fe-Ni system: Investigation by first-principles calculations and atomistic simulations. *Acta Materialia*, 53(15):4029–4041, 2005.

[31] Reed A Howald. The Thermodynamics of Tetrataenite and Awaruite : A Review of the Fe-Ni Phase Diagram. *Metallurgical and Materials Transactions A*, 34(September):1759–1769, 2003.

[32] K B Reuter, D B Williams, and J I Goldstein. Determination of the Fe-Ni Phase Diagram below 400 C. *Metallurgical and Materials Transactions A*, 20(April):719–725, 1989.

[33] Magnetic and Structural Study of FeNi3 Nanoparticles: Effect of Calcination Temperature. *Journal of Superconductivity and Novel Magnetism*, 27(12):2803–2811, 2014.

[34] D Turnbull and H Ehrenreich. Solid-State Physics: Advances in Research and Applications. *osti.gov*, 1997.

[35] Şakir Erkoç. Empirical many-body potential energy functions used in computer simulations of condensed matter properties. *Physics Reports*, 278(2):79–105, 1997.

[36] Risto M. Nieminen, Puska Martti J., and Manninen Matti, editors. *Many-Atom Interactions in Solids*. Springer-Verlag Berlin Heidelberg, 1 edition, 1990.

[37] David S. Sholl and Janice A. Steckel. *Chapter 01: Density Functional Theory: A Practical Introduction*. 2009.

[38] P Hohenberg and W Kohn. The Inhomogeneous Electron Gas. *Phys. Rev.*, 136(3B):B864, 1964.

[39] Philip J Hasnip, Keith Refson, Matt I J Probert, Jonathan R Yates, Stewart J Clark, and Chris J Pickard. Density functional theory in the solid state. 372(2011), 2014.

[40] Hande Toffoli. Computational Materials Science I. Technical report, 2017.

[41] W. K. Hastings. Monte carlo sampling methods using Markov chains and their applications. *Biometrika*, 57(1):97–109, 1970.

[42] Daan Frenkel and Berend Smit. Understanding Molecular Simulation, 2002.

[43] Riccardo Ferrando. Kinetic aspects. nucleation, mixing, coalescence. In *Nanoalloys*, pages 175–202. 2013.

[44] Ercolessi Furio. molecular dynamics primer. Technical report, International School for Advanced Studies, Trieste, Italy, 1997.

[45] T Halicioglu and C W Bauschlicher Jr. Physics of microclusters. *Reports on Progress in Physics*, 51(6):883, 1988.

[46] M.L. Klein and J.A. Venables. *Rare Gas Solids*. Number v. 1 in Rare Gas Solids. Academic Press, 1976.

[47] Mark J. Uline and David S. Corti. Molecular dynamics at constant pressure: Allowing the system to control volume fluctuations via a "shell" particle, 2013.

[48] Victor Ruhle. Berendsen and Nose-Hoover thermostats. *Thesis*, pages 1–4, 2007.

[49] Mark E. Tuckerman, José Alejandre, Roberto López-Rendón, Andrea L. Jochim, and Glenn J. Martyna. A Liouville-operator derived measure-preserving integrator for molecular dynamics simulations in the isothermal-isobaric ensemble. *Journal of Physics A: Mathematical and General*, 39(19):5629–5651, 2006.

[50] Loup Verlet. Comyuter "Experiments" on Classical Fluids. I. Thermodynamical Properties of Lennard, -Jones Molecules. *Physical review*, 159(1), 1967.

[51] Z. A. Matysina, Amdulla O. Mekhrabov, Z. M. Babaev, and S. Yu Zaginaichenko. Impurities in Ni3Fe magnetic alloys. *Journal of Physics and Chemistry of Solids*, 48(5):419–423, 1987.

[52] Amdulla O Mekhrabov. Impurity effect of Me=Cr, Nb or Mn third component atoms on hyperfine interactions in ordered Ni3Fe alloy. *Hyperfine Interactions*, 59(1):337–340, aug 1990.

[53] Amdulla Mekhrabov, Z M Babayev, A A Katsnel'son, and Z A Matysina. Pseudopotential Calculation of Atomic Pair Interaction Energies and Estimation of the Kurnakov Temperature of Ternary Alloys Ni3(Fe, Me). 61:44–48, 1986.

[54] Amdulla Mekhrabov. Pseudopotential Calculation of Atomic Short Range Order Parameters of Three-Component Alloys Ni3(Fe, Me). 62:181–183, 1986.

[55] H. P. Cheng and D. E. Ellis. First-principles potentials in modeling structure and thermodynamics of Fe-Ni alloys. *Physical Review B*, 39(17):12469–12483, 1989.

[56] S. M. Foiles, M. I. Baskes, and M. S. Daw. Embedded-atom-method functions

for the fcc metals Cu, Ag, Au, Ni, Pd, Pt, and their alloys. *Physical Review B*, 33(12):7983–7991, 1986.

[57] Murray. S Daw and M.I. Baskes. Daw-Baskes_EAM.pdf, 1984.

[58] R. A. Johnson. Alloy models with the embedded-atom method. *Phys. Rev. B*, 39:12554–12559, Jun 1989.

[59] M Grujicic and P Dang. Computer simulation of martensitic transformation face-centered cubic alloys in Fe-Ni. 201:194–204, 1995.

[60] R. Meyer and P. Entel. Martensite-austenite transition and phonon dispersion curves of $\mathrm{fe}_{1-x}\mathrm{ni}_x$ studied by molecular-dynamics simulations. *Phys. Rev. B*, 57:5140–5147, Mar 1998.

[61] K Kadau, P Entel, and P S Lomdahl. Molecular-dynamics study of martensitic transformations in sintered FeNi nanoparticles. *Computer Physics Communications*, 147(1):126–129, 2002.

[62] M Byshkin Marc Hou. Phase transformations and segregation in Fe – Ni alloys and nanoalloys. pages 5784–5793, 2012.

[63] Guojian Li, Xudong Sui, Xuesi Qin, Yonghui Ma, Kai Wang, and Qiang Wang. Discussion. *Physics Letters A*, 380(42):3500–3504, 2016.

[64] Sefa Kazanc and Fatih Ahmet Celik. The local order and structural study of liquid pdag alloy during cooling processes under different pressures. *Chinese Journal of Physics*, 52(2):852–864, 2014.

[65] Alexander Stukowski. Structure identification methods for atomistic simulations of crystalline materials. *Modelling and Simulation in Materials Science and Engineering*, 20(4), 2012.

[66] Ovito open visulization tool. http://www.ovito.org, 2018.

[67] Masato Shimono and Hidehiro Onodera. Dynamics and Geometry of Icosahedral Order in Liquid and Glassy Phases of Metallic Glasses. *Metals*, 5(4):1163–1187, 2015.

[68] H. Ehrenreich and D. Turnbull. *Solid State Physics*. Number v. 45 in Solid State Physics. Elsevier Science, 1991.

[69] S. Ali, V. S. Myasnichenko, and E. C. Neyts. Size-dependent strain and surface energies of gold nanoclusters. *Phys. Chem. Chem. Phys.*, 18(2):792–800, 2016.

[70] Andrey Sobolev and Alexander Mirzoev. Voronoi analysis of the short-range atomic structure in iron and iron-carbon melts. In *AIP Conference Proceedings*, volume 1673, 2015.

[71] B.M. Smirnov. *Physics of Atoms and Ions*. Graduate Texts in Contemporary Physics. Springer New York, 2003.

[72] Florent Calvo. Thermodynamics of nanoalloys. *Phys. Chem. Chem. Phys.*, 17(42):27922–27939, 2015.

[73] I. Chicinaş, V. Pop, O. Isnard, J. M. Le Breton, and J. Juraszek. Synthesis and magnetic properties of Ni3Fe intermetallic compound obtained by mechanical alloying. *Journal of Alloys and Compounds*, 352(1-2):34–40, 2003.

[74] W. H. Qi, B. Y. Huang, M. P. Wang, Z. M. Yin, and J. Li. Molecular dynamic simulation of the size- and shape-dependent lattice parameter of small Platinum nanoparticles. *Journal of Nanoparticle Research*, 11(3):575–580, 2009.

[75] P. H. T. Philipsen and E. J. Baerends. Cohesive energy of 3d transition metals: Density functional theory atomic and bulk calculations. *Physical Review B*, 54(8):5326–5333, 1996.

[76] M. Hanbücken, P. Müller, and R.B. Wehrspohn. *Mechanical Stress on the Nanoscale: Simulation, Material Systems and Characterization Techniques*. Wiley, 2011.

[77] Roy L. Johnston. Metal nanoparticles and nanoalloys. *Frontiers of Nanoscience*, 3(1):1–42, 2012.

[78] Zbigniew Kaszkur. Thermodynamical properties of nanoalloys. In *Nanoalloys*, pages 147–174. 2013.

[79] Ricardo B. Schwarz and Carl C. Koch. Formation of amorphous alloys by the mechanical alloying of crystalline powders of pure metals and powders of intermetallics. *Applied Physics Letters*, 49(3):146–148, 1986.

[80] C. Suryanarayana. Mechanical alloying and milling, 2001.

[81] John S. Benjamin. Dispersion strengthened superalloys by mechanical alloying. *Metallurgical Transactions*, 1(10):2943–2951, 1970.

[82] M. Kis-Varga and D.L. Beke. Phase transitions in Cu-Sb systems induced by ball milling. *Materials Science Forum*, 225-227:465–470, 1996.

[83] M. Miki, T. Yamasaki, and Y. Ogino. Preparation of Nanocrystalline NbN and (Nb,Al)N Powders by Mechanical Alloying Under Nitrogen Atmosphere. *Materials Transactions*, 33(9):839–844, 1992.

[84] Md Eaqub Ali, Mahbub Ullah, and Sharifah Bee Abd Hamid. Surfactant-Assisted Ball Milling: A Novel Route to Novel Materials with Controlled Nanostructure-A Review. *Rev. Adv. Mater. Sci*, 37:1–14, 2014.

[85] Hui Zhao, Zhenghou Zhu, Chao Xiong, Xing Xu, and Qianying Lin. The effect of transverse magnetic field treatment on wave-absorbing properties of FeNi alloy powders. *Journal of Magnetism and Magnetic Materials*, 422(Supplement C):402–406, 2017.

[86] Qilong Liao, Rina Tannenbaum, and Zhong Lin Wang. Synthesis of FeNi3 alloyed nanoparticles by hydrothermal reduction. *Journal of Physical Chemistry B*, 110(29):14262–14265, 2006.

[87] M Pkała, D Oleszak, E Jartych, and J K Żurawicz. Structural and magnetic study of mechanically alloyed Fe-Ni. *Nanostructured Materials*, 11(6):789–796, 1999.

[88] Elżbieta Jartych, Jan K Żurawicz, Dariusz Oleszak, and Marek Pękała. X-ray diffraction, magnetization and Mössbauer studies of nanocrystalline Fe–Ni alloys prepared by low- and high-energy ball milling. *Journal of Magnetism and Magnetic Materials*, 208(3):221–230, 2000.

[89] Kh Gheisari, S. Javadpour, J. T. Oh, and M. Ghaffari. The effect of milling speed on the structural properties of mechanically alloyed Fe-45%Ni powders. *Journal of Alloys and Compounds*, 472(1-2):416–420, 2009.

[90] K. Gheisari, S. Shahriari, and S. Javadpour. Structural evolution and magnetic properties of nanocrystalline 50 Permalloy powders prepared by mechanical alloying. *Journal of Alloys and Compounds*, 574:71–82, 2013.

[91] N.C. Ghosh, H.N. Das, M.A. Gafur, and A.K.M. Akther Hossain. Formation and Magnetic Properties of Nanocrystalline 78.5-permalloy by Mechanical Alloying. *Procedia Engineering*, 90:136–139, 2014.

[92] Amir Fadaie. *Production and Structural Characterization of Iron-Boron Nanoalloys*. PhD thesis, 2014.

[93] L. Seda Mut. *Synthesis and Structural Characterization of Nickel-Boron Nanoalloys*. PhD thesis, Middle East Technical University, 2015.

[94] B. D. Cullity. *Elements of X-Ray Diffraction*. Addison-Wesley Publishing Company, Inc., Massachusetts, 1956.

[95] A. Khorsand Zak, W. H. Abd. Majid, M. E. Abrishami, and Ramin Yousefi. X-ray analysis of ZnO nanoparticles by Williamson-Hall and size-strain plot methods. *Solid State Sciences*, 13(1):251–256, 2011.

[96] Ahmad Monshi, Mohammad Reza Foroughi, and Mohammad Reza Monshi. Modified Scherrer Equation to Estimate More Accurately Nano-Crystallite Size Using XRD. *World Journal of Nano Science and Engineering*, 02(03):154–160, 2012.

[97] C. Machio, D. Nyabadza, V. Sibanda, and H. K. Chikwanda. Characterization of mechanically alloyed f.c.c. Ti-Mg-based powders. *Powder Technology*, 207(1-3):387–395, 2011.

[98] Xian-Wen Wei, Guo-Xing Zhu, Chuan-Jun Xia, and Yin Ye. A solution phase fabrication of magnetic nanoparticles encapsulated in carbon. *Nanotechnology*, 17(17):4307–4311, 2006.

[99] Sharif Ahmad, Ufana Riaz, Ajeet Kaushik, and Javed Alam. Soft Template Synthesis of Super Paramagnetic Fe3O4 Nanoparticles a Novel Technique. *Journal of Inorganic and Organometallic Polymers and Materials*, 19(February 2016):355–360, 2009.